Integral Twist Actuation of Helicopter Rotor Blades for Vibration Reduction

by

SangJoon Shin

B.S., Aerospace Engineering, Seoul National University (1989)

M.S., Aerospace Engineering, Seoul National University (1991)

S.M., Aeronautics and Astronautics, Massachusetts Institute of Technology (1999)

Submitted to the Department of Aeronautics and Astronautics in partial fulfillment of the requirements for the degree of

Doctor of Philosophy in Aeronautics and Astronautics

at the

MASSACHUSETTS INSTITUTE OF TECHNOLOGY

August 2001

September 2001

Author ....

Department of Aeronautics and Astronautics

August 24, 2001

Certified by ....

Carlos E. S. Cesnik, Committee Chair

Associate Professor of Aeronautics and Astronautics

Certified by ....

Steven R. Hall

Professor of Aeronautics and Astronautics

Certified by ....

Edward F. Crawley

Professor of Aeronautics and Astronautics

Certified by ....

Nesbitt W. Hagood

Associate Professor of Aeronautics and Astronautics

Accepted by ....

Wallace E. Vander Velde

Professor of Aeronautics and Astronautics

Chair, Committee on Graduate Students

Integral Twist Actuation of Helicopter Rotor Blades for Vibration Reduction

by

SangJoon Shin

Submitted to the Department of Aeronautics and Astronautics
on August 24, 2001 in Partial Fulfillment of the
Requirements for the Degree of
Doctor of Philosophy in Aeronautics and Astronautics

ABSTRACT

Active integral twist control for vibration reduction of helicopter rotors during forward flight is investigated. The twist deformation is obtained using embedded anisotropic piezocomposite actuators. An analytical framework is developed to examine integrally-twisted blades and their aeroelastic response during different flight conditions: frequency domain analysis for hover, and time domain analysis for forward flight. Both stem from the same three-dimensional electroelastic beam formulation with geometrical-exactness, and are coupled with a finite-state dynamic inflow aerodynamics model. A prototype Active Twist Rotor blade was designed with this framework using Active Fiber Composites as the actuator. The ATR prototype blade was successfully tested under non-rotating conditions. Hover testing was conducted to evaluate structural integrity and dynamic response. In both conditions, a very good correlation was obtained against the analysis. Finally, a four-bladed ATR system is built and tested to demonstrate its concept in forward flight. This experiment was conducted at NASA Langley Transonic Dynamics Tunnel and represents the first-of-a-kind Mach-scaled fully-active-twist rotor system to undergo forward flight test. In parallel, the impact upon the fixed- and rotating-system loads is estimated by the analysis. While discrepancies are found in the amplitude of the loads under actuation, the predicted trend of load variation with respect to its control phase correlates well. It was also shown, both experimentally and numerically, that the ATR blade design has the potential for hub vibratory load reduction of up to 90% using individual blade control actuation. Using the numerical framework, system identification is performed to estimate the harmonic transfer functions. The linear time-periodic system can be represented by a linear time-invariant system under the three modes of blade actuation: collective, longitudinal cyclic, and lateral cyclic. A vibration minimizing controller is designed based on this result, which implements classical disturbance rejection algorithm with some modifications. The controller is simulated numerically, and more than 90% of the 4P hub vibratory load is eliminated.

By accomplishing the experimental and analytical steps described in this thesis, the present concept is found to be a viable candidate for future generation low-vibration helicopters. Also, the analytical framework is shown to be very appropriate for exploring active blade designs, aeroelastic behavior prediction, and as simulation tool for closed-loop controllers.

Thesis supervisor: Carlos E. S. Cesnik, Chair
Title: Associate Professor of Aeronautics and Astronautics

Acknowledgments

I greatly appreciate Dr. Carlos E. S. Cesnik, who is my advisor, for his guidance and supervision throughout the entire process of this thesis. Without his encouragement, this thesis would not exist. I would also like to express my gratefulness to Dr. Steven R. Hall for sharing his profound knowledge with me regarding the helicopter and its control problems. Also, I would like to express my thankfulness to Dr. Nesbitt W. Hagood for his support during the period of my graduate study. I appreciate Dr. Edward F. Crawley and Dr. John Dugundji for the discussion and recommendations on my work.

I would definitely like to thank Mr. Matthew L. Wilbur for the financial support and all the wind-tunnel experiments, as well as CAMRAD II analysis. I also would like to express my thankfulness to Mr. Paul H. Mirick, Mr. William T. Yeager, Jr., Mr. Chester W. Langston, and Dr. W. Keats Wilkie for their support on the experiments.

I am profoundly grateful to Dr. Olivier A. Bauchau for providing DYMORE code and the help on its modification. Also, I wish to thank Dr. Xiaoyang Shang for his help on modifying the one-dimensional beam code.

I am grateful to Dr. John P. Rodgers, Dr. Eric F. Prechtl, Mr. Mads C. Schmidt, and Mr. Viresh K. Wickramasinghe for their support on the experiments of the ATR test blade and providing the updated AFC data. Special thanks to Ms. Afreen Siddiqi for her help on the blade signal generation and providing the system identification routine.

I would appreciate my parents for their love and support, and also, my sister, brother, brother-in-law, and twin nieces. Especially, I would like to profoundly thank my wife, JeeYoung, for her encouragement and understanding, and my daughter, SoMin, for her love and smile.

This work was sponsored by NASA Langley Research Center under the cooperative agreement # NCC1-323.

Contents

List of Figures

List of Tables

Nomenclature

a	lift curve slope of the airfoil
$\mathbf{a}$	global frame attached to the hub
$\mathbf{a}_o$	conformal rotation vector of the rotation from B_n^- to B_{n+1}^-, measured in the $\mathbf{a}$ frame
$\mathcal{A}$	dynamics matrix in harmonic state-space formulation
$A(t)$	dynamics matrix in state-space formulation
b	number of blades
$\mathbf{b}$	undeformed reference frame of the blade
$\mathbf{b}_o$	conformal rotation vector of the rotation from B_n^- to B_n^+, measured in the $\mathbf{a}$ frame
$\mathbf{B}$	deformed reference frame of the blade
$\mathcal{B}$	input matrix in harmonic state-space formulation
$B(t)$	input matrix in state-space formulation
c	blade chord length
c_{d_o}	profile drag coefficient of the airfoil
C^{ba}	transformation matrix from a to b
C^{Ba}	transformation matrix from a to B
C	rotation matrix, product of C^{ab} and C^{Ba}
$\mathcal{C}$	output matrix (related to state vector) in harmonic state-space formulation
$C(t)$	output matrix (related to state vector) in state-space formulation
C_T	non-dimensionalized rotor thrust coefficient

d	characteristic dimension of the beam cross section
$\mathbf{D}^2$	second difference operator matrix
$\mathcal{D}$	input matrix (related to state vector) in harmonic state-space formulation
$D(t)$	input matrix (related to output) in state-space formulation
e_1	unit vector $[1,\ 0,\ 0]^T$
$\mathbf{e}$	error vector
f_0	initial frequency of the chirp
f_1	final frequency of the chirp
f_a	external forces vector
$\mathbf{f}_B$	sectional force/moment vector measured in the $\mathbf{B}$ frame
$\mathbf{f}_m,\ \mathbf{f}_j$	elastic forces at the mid time-step point m, j, respectively
$f_{u_i},\ f_{\psi_i},\ f_{F_i}$ $f_{M_i},\ f_{P_i},\ f_{H_i}$	beam element functions explicitly integrated
F_1	beam axial force
$F_1^{(a)}$	actuation component of beam axial force
F_B	internal force column vector in the $\mathbf{B}$ frame
$F_B^{(a)}$	actuation column vector for internal force
F_{dB}	column vector of the viscous forces in the $\mathbf{B}$ frame
F_I	inflow terms in the inflow equilibrium equation
F_L	aerodynamic terms in the beam equilibrium equation
F_P	pressure terms in the inflow equilibrium equation
F_S	structural terms in the beam equilibrium equation
$g_1(s)$	warping due to axial strain
$g_2(s),\ g_3(s)$	warping due to bending strain
$\mathbf{g}_m$	m-th transfer function (in vector form)
G	transfer function in Laplace domain
$G(s)$	torsion-related warping
$\widehat{\mathbf{G}}(\omega)$	harmonic transfer function estimate

$\mathcal{G}$	harmonic transfer function
h	thickness of the shell surface
H_B	angular momentum column vector
I	3×3 inertial matrix
$\mathbf{k}$	sectional elastic curvature vector
J	cost function
K	kinetic energy density per unit span of the blade
$[K]$	general 6×6 stiffness matrix
$K(s)$	transfer function of the feedback compensator
K_B	sectional stiffness matrix measured in the $\mathbf{B}$ frame
K_{ij}	beam stiffness components
L	length of the shell
m	blade mass per unit span length
m_a	external moment vector
M_1	beam torsional moment
$M_2,\ M_3$	beam bending moments
$M_1^{(a)}$	actuation component of beam torsional moment
$M_2^{(a)},\ M_3^{(a)}$	actuation components of beam bending moments
M_B	internal moment column vector in the $\mathbf{B}$ frame
$M_B^{(a)}$	actuation column vector for internal moment
M_{dB}	column vector of the viscous moments in the $\mathbf{B}$ frame
n	number of data points in input vector $\mathbf{u}$
n_c	number of chirps that have already been generated
n_h	number of harmonic transfer functions to be evaluated
N	number of the one-dimensional elements for blade spanwise discretization
N	number of chirp to be generated in input signal
$\mathcal{N}$	frequency modulation (block diagonal) matrix
$\mathbf{p}_B$	sectional momentum vector measured in the $\mathbf{B}$ frame

P_B	linear momentum column vector
$\mathbf{q}$	external load vector per unit span measured in the **a** frame
r	submatrix (1,1) of the cross-section flexibility matrix
$\bar{r}$	non-dimensional radial station
r_t	projection of the position vector **r** on the tangential vector
r_n	projection of the position vector **r** on the normal vector
R	radius of the rotor blades
s	submatrix (2,2) of the cross-section flexibility matrix
$s,\ \xi$	coordinate with respect to the middle surface point along the surface
t	submatrix (1,2) of the cross-section flexibility matrix
t_d	actuation period
t_p	no actuation period between chirps in an input sequence
$\bar{t}$	non-dimensionalized time
$\widehat{t}$	pseudo time obtained by shifting time vector based on system phase
T	system period
$\mathbf{T}$	control response matrix
T_c	chirp period
T_d	delay time
T_r	rotor rotational period
$u(t)$	input signal in time domain
$\mathbf{u}$	displacement of an arbitrary point on the beam reference line to the deformed configuration, measured in the **a** frame
$\mathbf{u}$	vector of discretized $u(t)$
$\mathbf{u}$	vector of b/rev actuation amplitudes
$\mathbf{u}_1$	position of an arbitrary point on the beam reference line before deformation, measured in the **a** frame
$u_i(x)$	displacement field of the cross-section reference point

$u_i,\ \theta_i,\ F_i$ $M_i,\ P_i,\ H_i$	constant vectors of the corresponding quantities at each node i
U	potential energy density per unit span of the blade
$U(j\omega)$	input matrix with elements in frequency domain
$\mathbf{U}$	matrix with modulated and Fourier transformed input data vector elements
$\mathbf{U_c}$	chirp input vector for rotor system
$v_1,\ v_s,\ v_\xi$	displacement field of an arbitrary point in the shell frame
$v_1^{(a)}(s)$	actuation contribution to the out-of-plane displacement
V	magnitude of the electric field distribution shape
$\mathbf{V}$	vector for rotor actuation mode selection
V_B	linear velocity column vector in the **B** frame
w_a	initial angular velocity of a generic point on the **a** frame
$W_{B2},\ W_{B3}$	component of the relative wind velocity in the **B** frame
$\overline{\delta W}$	virtual work of applied loads per unit span
x	beam axial coordinate
$x(t)$	state vector in state-space formulation
X	column matrix of the structural variables in one-dimensional beam formulation
$\mathcal{X}$	harmonic state vector
$\bar{X}$	steady components of the structural variables X
$\check{X}(t)$	perturbed motion components of the structural variables X
y	output vector in the state space representation of the beam
$y,\ z$	Cartesian coordinates with respect to the reference point in the cross section
$\mathbf{y}$	vector of discretized $y(t)$
$y(t)$	output signal in time domain
Y	column matrix of the inflow state variables in one-dimensional beam formulation

$\bar{Y}$	steady components of the inflow state variables Y
$\check{Y}(t)$	perturbed motion components of the inflow state variables Y
$Y(j\omega)$	output matrix with elements in frequency domain
$\mathbf{z}$	vector of vibration amplitudes
$\mathbf{z_o}$	vector of vibration amplitudes with no actuation (baseline)
Z_a	arbitrary vector Z represented with respect to the **a** frame
Z_b	arbitrary vector Z represented with respect to the **b** frame
Z_B	arbitrary vector Z represented with respect to the **B** frame
$\tilde{Z_{jk}}$	$= Z_i \, e_{ijk}$
α	scalar for weighting difference operator matrix
α_S	rotor shaft tilt angle in the rearward direction
$\overline{\delta \mathsf{A}}$	virtual action at the ends of the beam and at the ends of the time interval
$\delta\Pi_a$	variational quantity of total potential energy in the **a** frame
$\delta\Pi_i$	$\delta\Pi$ over the i-th element
$\delta\boldsymbol{\psi}$	virtual rotation vector measured in a frame
Δ	3×3 identity matrix
Δl_i	length of the i-th spanwise beam element
ϕ_c	phase of the chirp
$\phi(x)$	twist angle of the cross section
$\boldsymbol{\Phi}$	state transition matrix over interval $[0, T]$
$\boldsymbol{\Phi}_{\mathbf{UU}}$	product of $\mathbf{U}$ and conjugate transpose of $\mathbf{U}$
$\boldsymbol{\Phi}_{\mathbf{UY}}$	product of $\mathbf{U}$ and conjugate transpose of $\mathbf{Y}$
$\gamma,\ \kappa$	generalized strain column vectors
$\gamma_B,\ \kappa_B$	components of the sectional strain vector, measured in the **B** frame
λ	induced flow velocity
μ	advance ratio
μ_S	damping coefficient to represent the beam structural damping
θ	rotation vector expressed in terms of Rodrigues parameters

θ_o	collective pitch angle setting
ρ	weight density of the blade
ρ_∞	air mass density
ω	input frequency to excite the system
$\boldsymbol{\omega}$	sectional angular velocity vector
ω_p	major frequency of the system
Ω	rotor rotational frequency
Ω_1	component of the blade rotation speed along $\mathbf{B}_1$ direction
Ω_B	angular velocity column vector in the $\mathbf{B}$ frame
Ω_o	nominal rotational speed of the rotor system
ξ	local coordinate of each beam finite element
ψ	blade azimuth angle
ψ	vector of azimuthal locations
$\bar{\psi}$	azimuthal location of the blade in the rotating frame
$\dot{(\ )}$, $(\ )^\bullet$	derivative with respect to time
$(\ )'$	derivative with respect to the beam span coordinate, x_1
$(\ )^*$	geometrically-exact kinematical quantity in the $\mathbf{a}$ frame
$\hat{(\ )}$	boundary values of the corresponding quantities
$\tilde{(\ )}$	skew-symmetric matrix

Chapter 1

Introduction

1.1 Background

Rotorcraft has been a very important mode of aerial transportation due to its capability of vertical take-off and landing, enabling many unique missions such as rescue operation at sea. However, it has also been under several serious constraints such as poor ride quality due to high levels of vibration [1] and noise, restricted flight envelope, low fatigue life of the structural components, and high operating cost. The primary source of those problems is the complex unsteady aerodynamic environment which is generated near the rotor blades mainly during forward flight [2]. An instantaneous asymmetry of the aerodynamic loads acting on the blades at different azimuth location is developed, and such asymmetry becomes more and more adverse as the forward flight speed increases. Therefore, the rotor system is the major component from which helicopter vibrations originate, and the resulting vibratory load becomes a dominant factor of reducing the life of fatigue-critical components and poor ride quality. These vibrations also limit the performance of the helicopters such as forward flight speeds, and tend to decrease payload due to the addition of extra vibration-alleviation devices. The coupling between the structural and mechanical components such as rotor, fuselage, engine, and transmission adds another degree of complexity to this problem.

A typical aerodynamic environment of the helicopter main rotor during forward

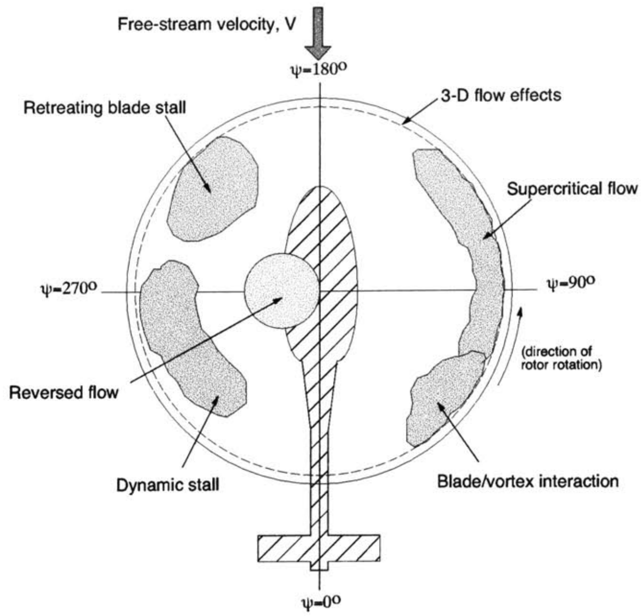

Figure 1-1: Aerodynamic environment in forward flight [3]

flight is illustrated in Fig. 1-1 [3], where helicopter flight velocity adds to the blade element rotating velocities on the advancing side ($0° < \psi < 180°$), and subtracts from it on the retreating side ($180° < \psi < 360°$). The resulting aerodynamic environment may be characterized as follows: high tip Mach number on the advancing side, and blade stall effects on the retreating side. A reverse flow region is also generated at the inboard on the retreating side. Such a complicated environment results in an instantaneous asymmetry of the aerodynamic loads acting among the blades at different azimuthal locations. This results in a vibratory response of a flexible blade structure, adding more complexity to the air loads asymmetry. This vibration is transmitted to the fuselage at the frequency of b/rev through the rotor hub, where b is the number of blades. This mechanism becomes a primary source of fuselage excitation.

The rotor blades usually have a built-in twist which is to relieve the lift difference between the inboard and outboard sections during hover, improving hover thrust. However, the larger the rotor blades have the built-in twist, the more severe fuselage vibrations result in forward flight. Therefore, helicopter designers traditionally trade-off the amount of built-in twist based on hover performance and forward flight vibrations.

1.2 Helicopter Vibration Reduction

There have been considerable efforts to reduce the vibration in helicopter [4, 5], and vibration alleviation methodologies employed by the helicopter designers may be categorized into the following three groups:

1. Varying passive structural properties of the rotor system or fuselage by tuning its dynamic characteristics [6];

2. Employing passive or active vibration absorbing devices either at the rotating system or the fixed system [7];

3. Direct modification of the excitation forces, principally aerodynamic forces to reduce vibration.

The first and second categories involve installation of vibration absorbing devices which produce counteracting inertial and damping forces. They are still used in most of the rotorcraft flying today although they also bring unavoidable penalties in terms of weight and tend to affect vibrations only at discrete points. Therefore, an effort to modify directly the excitation forces has been sought by the helicopter community, that is, to eliminate or reduce vibrations by modifying unsteady aerodynamic forces acting on the rotor blades. During the last two decades, this has been investigated and different implementations were attempted. Higher harmonic control (HHC) and individual blade control (IBC) are the typical examples of these efforts. Higher harmonic control is accomplished by manipulating a conventional swashplate to enable blade pitch control of a higher multiple frequency than an integer multiple of rotating frequency, i.e., $(kb \pm 1)$/rev. Individual blade control installs a feathering actuator in each blade rather than modulating the swashplate, and allows for blade pitch control at arbitrary frequencies. Several outstanding results were obtained regarding vibration reduction capability of these concepts, and they comprise of analytical studies searching for an optimal control scheme [8, 9, 10], wind tunnel tests with either small or full-scaled model [11, 12, 13, 14, 15], and flight tests [16]. However, these concepts based on employing additional hydraulic actuators installed on either non-rotating (beneath swashplate) or rotating (between pitch links) frames have not successfully entered into full-scale application. Typical disadvantages were identified in these concepts, such as adverse power requirement and limitation on excitation frequencies in HHC, and extreme mechanical complexity of hydraulic sliprings in IBC.

Recently, there appeared an opportunity of having multiple lightweight sensors/ actuators embedded or surface-mounted at several locations in the rotor blades and optimally distribute actuation with the aid of modern control algorithm [17, 18, 19]. By employing active materials for such sensors/actuators in order to implement individual blade control, one can potentially obtain advantages in terms of weight and power consumption when compared with traditional hydraulic systems. Basically these new actuators only requires electrical power to operate. Two main concepts have been under development for the active material application: rotor blade flap actuation and integral blade twist actuation [20]. The rotor blade flap actuation concept has been studied in various ways. Millott and Friedmann conducted a comprehensive study on its theoretical basis [21]. A bimorph servo-flap actuator is one of its primary implementations [22, 23, 24]. Recently a trailing-edge flap operated by piezostack-actuated X-frame was successfully fabricated and tested at a hover spin stand [25]. Other flap implementations [26, 27] and variants [28] are also under development, and the associated modeling being conducted [29].

On the other hand, the integral actuation concept [30, 31, 32, 33] presents itself as an aggressive alternative with several potential benefits. One of the advantages is simplicity of its actuation mechanism compared with that for the flap actuation. Besides providing redundancy in operation, the integral concept does not increase the profile drag of the blade just as discrete flap does. Moreover, the actuators once embedded in the composite construction become part of the load bearing structure, making the active blade a truly integrated multifunctional structure that allows for effective construction and assembly of future low vibration and low noise rotor blades.

1.3 Previous Work Related with Integral Twist Actuation

1.3.1 Actuators Applicable for the Integral Concept

An anisotropic actuator is required for the implementation of integral blade twist actuation with certain required characteristics. First, it must be flexible enough to be inserted in the curved shape of the blade assembly. Also, it should have its own structural integrity to withstand the pressure applied during blade fabrication and the external loads during the blade operation. It must have high levels of strain-inducing capability at an appropriately applied electric field. Anisotropy of the actuation is required so that tailoring in the blade design may be possible. Finally, cheap actuator is preferred considering the final blade cost. Candidates which are presently available include Active Fiber Composites (AFC) and Macro-Fiber Composites (MFC).

The AFC is an anisotropic, conformable actuator, which can be integrated with the passive structure [34]. It was originally developed at MIT and now being commercialized by Continuum Control Corporation, Billerica, Massachusetts. The AFC actuator utilizes interdigitated electrode poling and piezoelectric fibers embedded in an epoxy matrix. This combination results in a high performance piezoelectric actuator laminate with strength and conformability characteristics much greater than that of a conventional monolithic piezoceramic. Fig. 1-2 shows AFC packs being inserted in the blade assembly conducted as part of this thesis. However, some disadvantages are also identified for this actuator: difficulty of processing and handling expensive piezoelectric fibers during actuator manufacturing and high actuator voltage requirements. Basic material characterization and proof of concept of an integral twist-actuated rotor blade was investigated at MIT's Active Materials and Structures Laboratory [35].

The MFC has been recently developed at NASA Langley based on the same idea as the AFC in using the piezoelectric fibers under interdigitated electrodes [36]. In this actuator, shown in Fig. 1-3, the piezoelectric fibers are manufactured by dicing from

Figure 1-2: AFC being inserted at active blade assembly

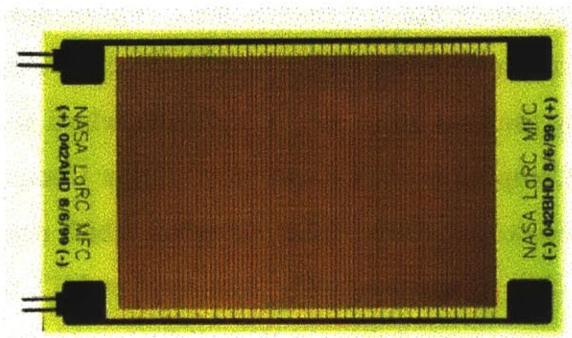

Figure 1-3: MFC actuator

low-cost monolithic piezoceramic wafers. Thus, it retains most advantageous features of the AFC with a potentially lower fabrication cost. This actuator is currently being tested for its basic characteristics, and it has been considered for use in many aerospace applications.

1.3.2 Previous Integral Helicopter Blades

For the integral blade twist actuation concept, the actuators may be embedded throughout the structure, which provides redundancy in operation. A major challenge with integral blades is to develop a design that presents sufficient twist authority while providing the torsional stiffness required for the aeroelastic performance of the blade. Chen and Chopra, based on the piezoelectric actuator presented in Barrett

[30], built and tested a 6-ft diameter two-bladed Froude-scaled rotor model with banks of piezoceramic crystal elements in $\pm 45^\circ$ embedded in the upper and lower surfaces of the test blade [31, 37]. Using dual-layer actuators, the active blade achieved 0.5° of maximum experimental tip twist actuation, still lower than the 1° to 2° necessary for the possible vibration control applications. Bernhard and Chopra studied another twist concept that incorporates an active bending-torsion actuator beam within the blade spar [28]. Tip twist angles of 0.15° to 0.5° (at 100 V) were achieved during Froude-scaled blade hover test.

The most relevant work for this thesis, however, is the one conducted by Rodgers and Hagood [32] as part of a Boeing/MIT program sponsored by DARPA [38]. They manufactured and hover tested a 1/6th Mach-scaled CH-47D blade in a two-bladed rotor where the integral twist actuation was obtained through the use of AFC. In order to design the blade structure and predict the actuation performance, a rudimentary single-cell active composite beam model [39] was used. Also, an intentional reduction by 50% on the baseline torsional stiffness was imposed and regarded to improve twist actuation. Hover testing on the MIT Hover Test Stand Facility demonstrated tip twist performance between 1° and 1.5° in the rotating environment. Boeing/MIT continues this work that eventually should lead to forward flight wind-tunnel tests and full-scale blade section manufacturing [38].

1.3.3 ATR Blade – Previous Work

Another example of an integral blade twist concept has been studied by the author and his co-workers [33, 40] as part of a NASA/Army/MIT Active Twist Rotor cooperative agreement program. The structural design of the ATR prototype blade employing embedded AFC actuators was conducted based on a newly developed analysis for active composite blade with integral anisotropic piezoelectric actuators [41]. The formulation is one of the first attempts for asymptotically-correct analysis of active multiple-cell beams presented in the literature. The approach is based on a two-step solution of the original three-dimensional electromechanical blade representation by means of an asymptotical approximation: a linear two-dimensional cross-sectional analysis and a nonlinear one-dimensional global analysis. The cross-sectional analysis, the first step, is based on a modified formulation originally proposed for passive beams by Badir [42]. The original formulation was revised and extended, providing the stiffness matrix and piezoelectric actuation vector in analytic form. A numerical validation of the stiffness matrix and actuation constants was carried out through comparison against VABS-A [43], a general asymptotically correct finite-element-based cross-sectional analysis intended for generic geometry (multiple cells, thin or thick walls, or even solid active beams). Very good agreement between these formulations was obtained, and only small discrepancies ($< 3\%$) were found for model blade constructions [41, 43]. The second step is the one-dimensional global analysis, and a direct expansion of the mixed variational intrinsic formulation of moving beams was utilized. It is a nonlinear analysis considering small strains and finite rotations, and its original (passive) formulation was presented by Hodges [44]. Verification of the one-dimensional global beam results combined with the cross-sectional analysis was conducted by comparing with other active beam models and few experimental cases (including CH-47D active blade) showing good agreement [41].

Using those set of analyses and loads originated from CAMRAD II, the ATR blade design was conducted, and it is described in detail in [33, 45]. The blade employed a total of 24 AFC packs placed on the front spar only, and distributed in 6 stations along the blade span. During the process of ATR blade design, a trend study was conducted in parallel to identify the relationship between torsional stiffness and twist actuation performance of the active blade [46]. It was shown analytically that the traditional effort of blade torsional stiffness reduction does not always bring twist performance improvement. According to the final selected design, a couple of testing articles were manufactured in advance to the full prototype blade for the structural integrity testing. Experimental structural characteristics of the prototype blade compared well with design goals, and modeling predictions correlate fairly with experimental results [33]. Bench actuation tests showed lower twist performance than originally expected due to the failure of 6 actuators among 24 embedded and limitation of high voltage amplitude down to a half amplitude from the scheduled magnitude [45]. Static tip twist actuation was experimentally observed of 1.1° peak-to-peak.

Even though the new vibration reduction approach using the active materials technology showed promising results from the conceptual point of view [47, 40] and successful preliminary hover testing with small-scaled models [32, 48], experimental forward flight tests were not performed until recently [49]. Moreover, an active aeroelastic environment to design, analyze, and simulate the behavior of integrally-twisted active rotor systems needed to be created. This should impact the ability to design active rotors and will support the design of their control law.

1.4 Present Work

This thesis concentrates on the study of vibration reduction using integral twist actuation on helicopter rotor blades. It includes the development of an analytical framework to identify dynamic characteristics of active rotor system in different flight conditions. The analytical model for forward flight combines a geometrically-exact theory for the dynamics of moving beams with active materials constitutive relations and a finite-state dynamic inflow theory for helicopter forward flight aerodynamics. The solution of this is conducted in time domain. Numerical results from the analytical models are correlated with experimental data obtained from bench, hover and forward flight testing. For this purpose, two main steps are taken. First, a hover testing using the ATR prototype blade previously manufactured is conducted, and the numerical results from the analytical hover model are correlated with the experimental data. Among other things, this step ensures the adequacy of the blade design and evaluates the twist actuation performance in the rotating condition. At the same time, the validity of the proposed analytical framework is demonstrated in both non-rotating and rotating conditions. Secondly, a four-active-bladed rotor system based on the prototype blade design is manufactured and tested in the open-loop control manner for the forward flight condition in the wind-tunnel. In parallel, an active aeroelastic analysis model is upgraded to deal with active twist rotor system during forward flight. Regarding the experimental work, an approach similar to the

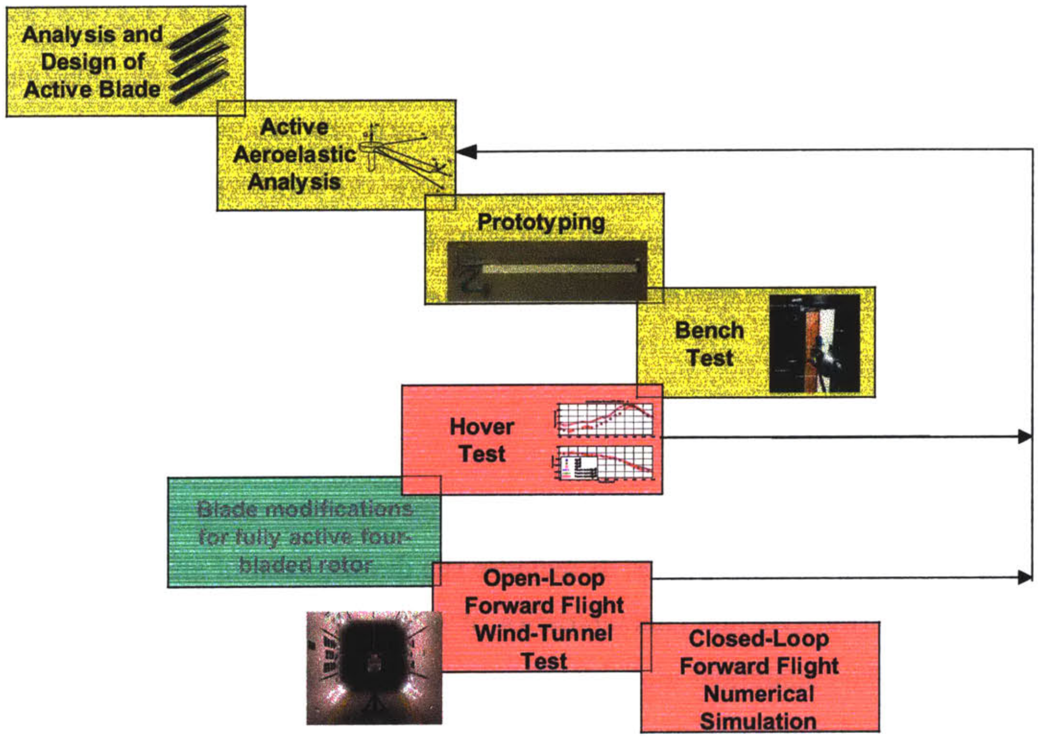

Figure 1-4: Overview of different stages of the NASA/Army/MIT ATR program

conventional HHC vibration reduction methodology [14] is pursued. The theoretical model is used for the system identification of the ATR rotor system, and by combining these frequency response functions corresponding to various flight conditions, a library of system transfer functions is composed. Within this effort, linear time-periodic components of the sensitivity functions are identified and compared with linear time-invariant members to see the degree of their contribution to the rotor system characterization. Finally, a closed-loop controller is designed and demonstrated for its vibration reduction capability. An overview of the different stages of this study is summarized in Fig. 1-4.

The specific objectives of this thesis are:

1. Develop a structural dynamics model for analysis and design of strain-actuated

helicopter blades

2. Extend it to an aeroelastic analysis framework to simulate helicopter flight with active twist rotor blades and evaluate its response functions

3. Correlate the analytical model with experiments conducted in the bench, hover and forward flight

4. Assess helicopter vibration reduction capability using active twist rotor blades with an appropriate closed-loop control algorithm.

Chapter 2

Analytical Framework

2.1 Introduction

For analyzing helicopter blades with embedded strain actuators, a framework is needed such that the effects of the active material embedded in the structure are kept throughout all the stages of the analysis. The framework should also contain an appropriate aeroelastic analysis component to predict the blade behavior under actuation during different operating conditions such as non-rotating, hover, and forward flight. For this purpose, a specific analytical framework for an active helicopter rotor system is proposed and its schematic is illustrated in Fig. 2-1.

A base element from which the framework originates is the structural model of a general composite beam with embedded anisotropic actuators, and this corresponds to the dashed block at the upper part in Fig. 2-1, designated as "3-D electroelastic beam." In this structural model, an asymptotical analysis takes the three-dimensional electromechanical problem of a rotor blade and reduces it into a set of two analyses: a linear analysis over the cross section and a nonlinear analysis of the resulting beam reference line. Such separation of the blade problem makes it convenient for aeroelastic analysis and consistently accounts for the active material effects. Using the structural model previously developed in [41, 45], the ATR prototype blade design was conducted, and its static twist actuation performance was evaluated [45]. Important elements included in the structural model are recapitulated in this chapter.

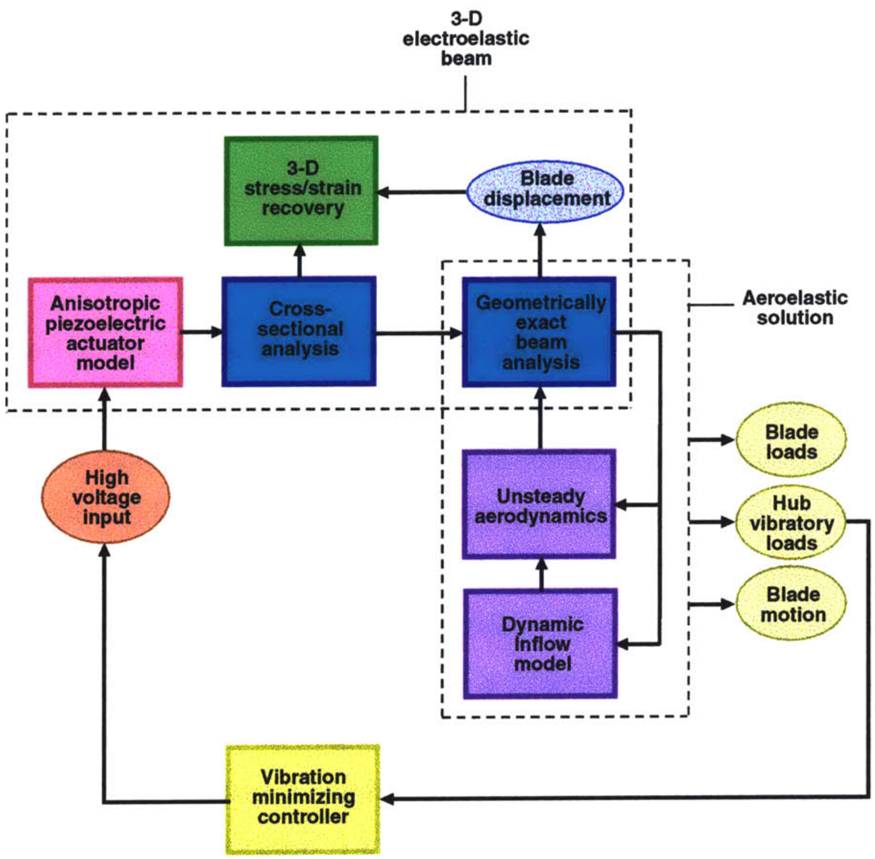

Figure 2-1: Schematic diagram of the analytical framework for an active helicopter blade and its aeroelastic behavior

The previous structural model is extended and improved in this thesis to investigate the dynamic characteristics of the active rotor system in the bench, hover, and forward flight conditions. This corresponds to the lower dashed block in Fig. 2-1, called "Aeroelastic solution." In this extension, the global beam analysis element from the previous structural model is combined with an appropriate aerodynamics model to compose an aeroelastic system. However, the system is still dependent upon the cross-sectional analysis regarding the beam cross-sectional properties. Solution of the resultant aeroelastic system is obtained in either frequency or time domain, and it includes the blade loads, hub vibratory loads, and blade motion.

Specifically, for hover calculation, a mixed form of the geometrically-exact beam analysis model [44] is modified to account for integral actuation, and combined with finite-state dynamic inflow unsteady aerodynamics [50]. Based on the idea of small perturbation from a steady-state equilibrium position, frequency response functions of the active blade are determined using Laplace transform of the state-space representation. By performing hover analysis, more insight into the fidelity of the present modeling can be explored. Also, the behavior of the integral actuator under rotating condition can be assessed before examining the overall actuation authority of the ATR system.

In forward flight analysis, the same geometrically-exact beam formulation is utilized but in displacement-based form. Also, the forward flight version of the same aerodynamics model is used, and their solution is performed in time domain. For implementation, an existing multi-body dynamics code [51] is modified for the needed active beam analysis. Time domain integration is selected since it is adequate for simulation of the blade response under open-loop actuation. This enables system identification for the sake of modern control, and ultimately closed-loop performance of ATR systems can be studied.

2.2 Cross-Sectional Analysis

Stiffness and actuation forcing constants for an active anisotropic beam in its cross-section are obtained from a variational-asymptotical formulation. The derivation stems from a shell theory, and the displacement field (including out-of-plane warping functions) is not assumed *a priori* but rather results from the asymptotical approach. It is presented in detail in [45] for thin-walled cross sections, and [52] presents a generalization of the previous formulation for generic (thin or thick-walled, even solid) cross sections. The thin-walled restriction allows for closed form solutions of the displacement field (which is derived and not assumed), and stiffness and actuation constants, helping determine design paradigms on this new type of blade. These stiffness and actuation constants are then used in the active beam finite element discretization of the blade reference line.

Even though the details of this formulation can be found in [45], the main results are reproduced below for completeness. With an assumed linear piezoelectric constitutive relation and starting from a shell strain energy, the two-dimensional original electroelastic shell formulation is condensed to a one-dimensional beam problem. According to the notation presented in Fig. 2-2, the displacement field is found to be of the form:

$$
\begin{aligned}
v_1 &= u_1(x) - y(s)\; u_2'(x) - z(s)\; u_3'(x) + G(s)\; \phi'(x) + g_1(s)\; u_1'(x) \\
&\quad + g_2(s)\; u_2''(x) + g_3(s)\; u_3''(x) + v_1^{(a)}(s) \\
v_s &= u_2(x)\,\frac{dy}{ds} + u_3(x)\,\frac{dz}{ds} + \phi(x) r_n \\
v_\xi &= u_2(x)\,\frac{dz}{ds} - u_3(x)\,\frac{dy}{ds} - \phi(x) r_t
\end{aligned}
\tag{2.1}
$$

where the superscript (a) indicates that the component is function of the applied electric field (in the case of thin-walled cross sections, the actuation only influences the out-of-plane component of the displacement field). The functions $G(s)$ and $g_i(s)$ are the warping functions associated with torsion, extension, and two bending measures.

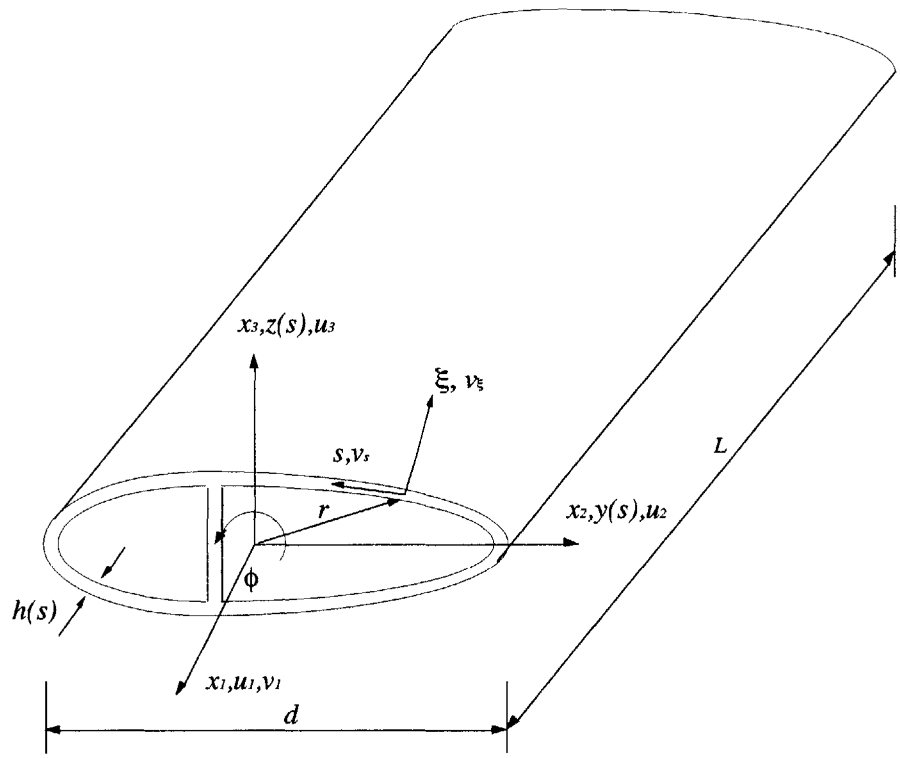

Figure 2-2: Two-cell thin-walled cross section beam

Associated with this displacement field, the beam constitutive relation which relates beam generalized forces (axial force, twist, and two bending moments, respectively) with beam generalized strains (axial strain, twist curvature, and two bending curvatures) and corresponding generalized actuation forces is obtained in the following form:

$$\left\{\begin{array}{c} F_1 \\ M_1 \\ M_2 \\ M_3 \end{array}\right\} = \left[\begin{array}{cccc} K_{11} & K_{12} & K_{13} & K_{14} \\ K_{12} & K_{22} & K_{23} & K_{24} \\ K_{13} & K_{23} & K_{33} & K_{34} \\ K_{14} & K_{24} & K_{34} & K_{44} \end{array}\right] \cdot \left\{\begin{array}{c} \gamma_1 \\ \kappa_1 \\ \kappa_2 \\ \kappa_3 \end{array}\right\} - \left\{\begin{array}{c} F_1^{(a)} \\ M_1^{(a)} \\ M_2^{(a)} \\ M_3^{(a)} \end{array}\right\} \tag{2.2}$$

where $[K_{ij}]$ is the stiffness matrix function of geometry and material distribution at the rotor cross section. γ_1 is the axial strain, κ_1 is the elastic twist, and κ_2, κ_3 are two bending curvatures. The actuation vector is a function of the geometry, material distribution, and applied electric field. Detailed expressions for the stiffness matrix

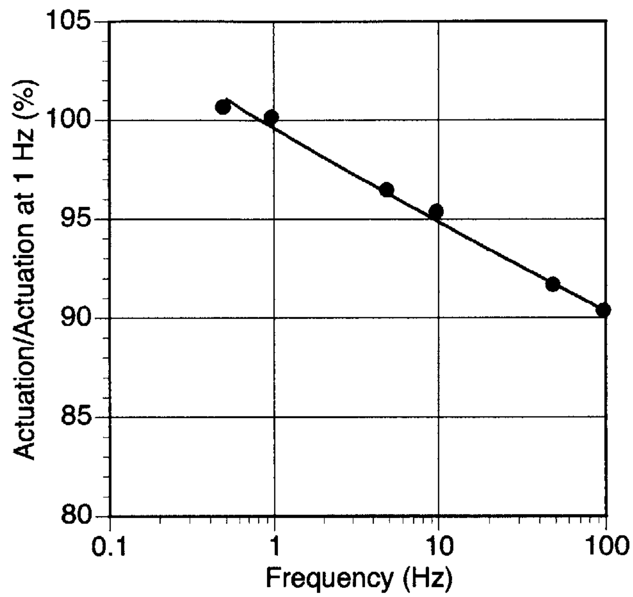

Figure 2-3: Degradation of free strain actuation with the frequency of excitation for the piezoelectric actuators used in the ATR blade

and actuation vector are found in [41]. Eq. (2.2) is consistently utilized in the further global beam analyses providing the numerical values of structural properties and actuation forcing vectors of active twist blades at several different discrete spanwise locations.

Since the free strain properties of piezoelectric material are dependent on the excitation frequency, the actuation forcing vector is not only dependent on the overall cross-sectional material distribution and geometry, but also on the magnitude and frequency of the electric field excitation. Moreover, the actuation performance degrades with the increase in frequency of the electric field due to the inherent capacitive nature of the piezoelectric material. To account for such actuation dependency on frequency, a correction is added to the above constitutive relation. This correction is obtained experimentally by curve fitting the data shown in Fig. 2-3, which is characteristic of the active material system used in the ATR blades [53]. Therefore:

$$\frac{\text{Free strain actuation at } f}{\text{Free strain actuation at 1 Hz}}(\%) = a \cdot f^{-2.117\times 10^{-2}} \tag{2.3}$$

where $a = e^{4.601}$, and f is the actuation frequency in Hz ($R^2 = 0.9932$). The amplitude dependence is assumed linear here, with a linearization of the actuators properties conducted around the operating condition. In practice, some nonlinear behaviors of the ATR prototype blade with respect to applied voltage were observed during bench test [33].

2.3 Global Beam Analysis

2.3.1 Mixed Form for Hover Analysis

The nonlinear one-dimensional global analysis considering small strains and finite rotations is presented here as a direct expansion of the mixed variational intrinsic formulation of moving beams originally presented by Hodges [44], and implemented by Shang and Hodges [54]. The notation used here is based on matrix notation and is consistent with the original work of Hodges [44]. Some steps of the original work are repeated here to help understanding the modifications required in this extended active formulation.

As shown in Fig. 2-4, a global frame named a is rotating with the rotor, with its axes labeled a_1, a_2 and a_3. The undeformed reference frame of the blade is named b, with its axes labeled b_1, b_2 and b_3, and the deformed reference frame named B, with its axes labeled B_1, B_2 and B_3 (though not shown in Fig. 2-4). Any arbitrary vector V represented by its components in one of the basis may be converted to another basis like

$$V_b = C^{ba} V_a, \quad V_B = C^{Ba} V_a \tag{2.4}$$

where C^{ba} is the transformation matrix from a to b, and C^{Ba} is that from a to B. There are several ways to express these transformation matrices. C^{ba} can be expressed in terms of direction cosines from the initial geometry of the rotor blade, while C^{Ba} contains the unknown rotation variables.

The variational formulation is derived from Hamilton's principle which can be written as

$$\int_{t_1}^{t_2} \int_0^l [\delta(K - U) + \overline{\delta W}] \, dx_1 dt = \overline{\delta \mathsf{A}} \tag{2.5}$$

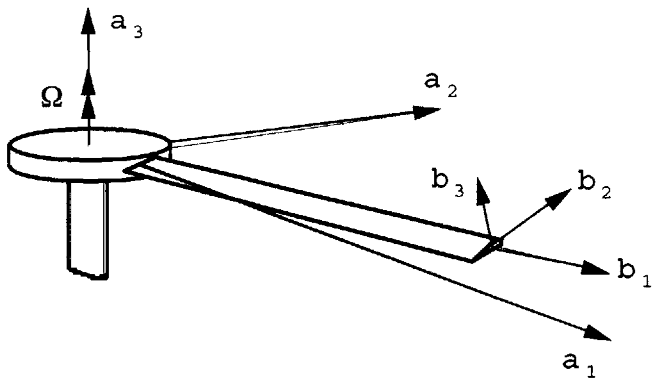

Figure 2-4: Blade frames of reference for the global analysis

where t_1 and t_2 are arbitrarily fixed times, K and U are the kinetic and potential energy densities per unit span, respectively. $\overline{\delta \mathsf{A}}$ is the virtual action at the ends of the beam and at the ends of the time interval, and $\overline{\delta W}$ is the virtual work of applied loads per unit span.

Taking the variation of the kinetic and potential energy terms with respect to V_B and Ω_B, the linear and angular velocity column vectors, respectively, and with respect to γ and κ, the generalized strain column vectors, yields

$$\begin{aligned} F_B &= \left(\frac{\partial U}{\partial \gamma}\right)^T, \quad M_B = \left(\frac{\partial U}{\partial \kappa}\right)^T \\ P_B &= \left(\frac{\partial K}{\partial V_B}\right)^T, \quad H_B = \left(\frac{\partial K}{\partial \Omega_B}\right)^T \end{aligned} \tag{2.6}$$

where F_B and M_B are internal force and moment column vectors, and P_B and H_B are linear and angular momentum column vectors, all expressed with respected to the B frame.

The geometrically-exact kinematical relations in the a frame are given by

$$\begin{aligned} \gamma &= C^{Ba}\left(C^{ab}e_1 + u_a'\right) - e_1 \\ \kappa &= C^{ba}\left(\frac{\Delta - \frac{\tilde{\theta}}{2}}{1 + \frac{\theta^T\theta}{4}}\right)\theta' \\ V_B &= C^{Ba}\left(v_a + \dot{u}_a + \tilde{\omega}_a u_a\right) \end{aligned}$$

$$\Omega_B = C^{ba}\left(\frac{\Delta - \frac{\tilde{\theta}}{2}}{1+\frac{\theta^T\theta}{4}}\right)\dot{\theta} + C^{Ba}\omega_a \tag{2.7}$$

where u_a is the displacement vector measured in the a frame, θ is the rotation vector expressed in terms of Rodrigues parameters, e_1 is the unit vector $[1,\ 0,\ 0]^T$, Δ is the 3×3 identity matrix, v_a and w_a are the initial velocity and initial angular velocity of a generic point on the a frame. $\dot{(\ )}$ is a derivative with respect to time, and $(\ )'$ is a derivative with respect to the spanwise curvilinear coordinate. $\tilde{(\ )}$ operator applied to a column vector is defined as $\tilde{(\ )}_{mn} = -e_{nmk}(\ )_k$, with e_{nmk} being the permutation tensor.

To form a mixed formulation, Lagrange's multipliers are used to enforce the satisfaction of the kinematical equations, Eq. (2.7).

Manipulating the equations accordingly [54], one can obtain the a frame version of the variational formulation based on exact intrinsic equations for dynamics of moving beams as

$$\int_{t_1}^{t_2} \delta\Pi_a \, dt = 0 \tag{2.8}$$

where

$$\begin{aligned}
\delta\Pi_a = & \int_0^l \{\delta u_a'^T C^T C^{ab} F_B + \delta u_a^T[(C^T C^{ab} P_B)^\bullet + \tilde{\omega}_a C^T C^{ab} P_B] \\
& + \overline{\delta\psi}_a'^T C^T C^{ab} M_B - \overline{\delta\psi}_a^T C^T C^{ab}(\tilde{e_1} + \tilde{\gamma}) F_B \\
& + \overline{\delta\psi}_a^T[(C^T C^{ab} H_B)^\bullet + \tilde{\omega}_a C^T C^{ab} H_B + C^T C^{ab} \widetilde{V_B} P_B] \\
& - \overline{\delta F}_a^T[C^T C^{ab}(e_1 + \gamma) - C^{ab} e_1] - \overline{\delta F}_a'^T u_a \\
& - \overline{\delta M}_a^T(\Delta + \frac{\tilde{\theta}}{2} + \frac{\theta\theta^T}{4}) C^{ab}\kappa - \overline{\delta M}_a'\theta \\
& + \overline{\delta P}_a^T(C^T C^{ab} V_B - v_a - \tilde{\omega}_a u_a) - \overline{\delta P}_a^T \dot{u}_a \\
& + \overline{\delta H}_a^T(\Delta - \frac{\tilde{\theta}}{2} + \frac{\theta\theta^T}{2})(C^T C^{ab}\Omega_B - \omega_a) \\
& - \overline{\delta H}_a^T \dot{\theta} - \delta u_a^T f_a - \overline{\delta\psi}_a^T m_a\} dx_1 \\
& - \left|(\delta u_a^T \hat{F}_a + \overline{\delta\psi}_a^T \hat{M}_a - \overline{\delta F}_a^T \hat{u}_a - \overline{\delta M}_a^T \hat{\theta}\right|_0^l
\end{aligned} \tag{2.9}$$

and the rotation matrix C is the product $C^{Ba}C^{ab}$ and is expressed in terms of θ as

$$C = \frac{(1 - \frac{\theta^T\theta}{4})\Delta - \tilde{\theta} + \frac{\theta\theta^T}{2}}{1 + \frac{\theta^T\theta}{4}} \tag{2.10}$$

In Eq. (2.9), f_a and m_a are the external force and moment vectors respectively, which result from aerodynamic loads. The $\hat{()}$ terms are boundary values of the corresponding quantities. The generalized strain and force measures, and velocity and momentum measures are related through the constitutive relations in the following form:

$$\begin{aligned} \left\{ \begin{array}{c} F_B \\ M_B \end{array} \right\} &= [K] \left\{ \begin{array}{c} \gamma \\ \kappa \end{array} \right\} - \left\{ \begin{array}{c} F_B^{(a)} \\ M_B^{(a)} \end{array} \right\} \\ \left\{ \begin{array}{c} P_B \\ H_B \end{array} \right\} &= \left[\begin{array}{cc} m\Delta & -m\bar{\xi}_B \\ m\bar{\xi}_B & I \end{array} \right] \left\{ \begin{array}{c} V_B \\ \Omega_B \end{array} \right\} \end{aligned} \tag{2.11}$$

and these expressions are solved for γ, κ, V_B, and Ω_B as function of the other measures and constants and used in Eq. (2.9). The stiffness $[K]$ is in general a 6×6 matrix, function of material distribution and cross sectional geometry. As described in [55], the 6×6 stiffness matrix is related to the 4×4 one. The latter is used in this thesis, where the stiffness matrix and column vector for the piezoelectric actuation comes from the variational asymptotical analysis of active cross sections as presented in the previous section.

Adopting a finite element discretization by dividing the blade into N elements, Eq. (2.8) is written as

$$\int_{t_1}^{t_2} \sum_i \delta\Pi_i \, dt = 0 \tag{2.12}$$

where index i indicates the i-th element with length Δl_i, $\delta\Pi_i$ is the corresponding spatial integration of the function in Eq. (2.9) over the i-th element. Due to the formulation's weakest form, the simplest shape functions can be used. Therefore, the following transformation and interpolation are applied within each element [54]

$$x = x_i + \xi \Delta l_i,\ dx = \Delta l_i\ d\xi,\ (\ )' = \frac{1}{\Delta l_i}\ \frac{d}{d\xi}(\ ) \tag{2.13}$$

$$\begin{aligned}
\delta u_a &= \delta u_i(1-\xi) + \delta u_{i+1}\xi, \qquad u_a = u_i \\
\overline{\delta\psi}_a &= \overline{\delta\psi}_i(1-\xi) + \overline{\delta\psi}_{i+1}\xi, \qquad \theta = \theta_i \\
\overline{\delta F}_a &= \overline{\delta F}_i(1-\xi) + \overline{\delta F}_{i+1}\xi, \qquad F_B = F_i \\
\overline{\delta M}_a &= \overline{\delta M}_i(1-\xi) + \overline{\delta M}_{i+1}\xi, \quad M_B = M_i \\
\overline{\delta P}_a &= \overline{\delta P}_i, \qquad P_B = P_i \\
\overline{\delta H}_a &= \overline{\delta H}_i, \qquad H_B = H_i
\end{aligned}$$

where u_i, θ_i, F_i, M_i, P_i and H_i are constant vectors at each node i, and all δ quantities are arbitrary. ξ varies from 0 to 1.

With these shape functions, the spatial integration in Eq. (2.12) can be performed explicitly to give

$$\begin{aligned}
\sum_{i=1}^{N} \quad & \{\delta u_i^T f_{u_i} + \overline{\delta\psi}_i^T f_{\psi_i} + \overline{\delta F}_i^T f_{F_i} + \overline{\delta M}_i^T f_{M_i} + \overline{\delta P}_i^T f_{P_i} + \overline{\delta H}_i^T f_{H_i} \\
& + \delta u_{i+1}^T f_{u_{i+1}} + \overline{\delta\psi}_{i+1}^T f_{\psi_{i+1}} + \overline{\delta F}_{i+1}^T f_{F_{i+1}} + \overline{\delta M}_{i+1}^T f_{M_{i+1}}\} \\
= \quad & \delta u_{N+1}^T \hat{F}_{N+1} + \overline{\delta\psi}_{N+1}^T \hat{M}_{N+1} - \overline{\delta F}_{N+1}^T \hat{u}_{N+1} - \overline{\delta M}_{N+1}^T \hat{\theta}_{N+1} \\
& - \delta u_1^T\ \hat{F}_1 - \overline{\delta\psi}_1^T \hat{M}_1 + \overline{\delta F}_1^T\ \hat{u}_1 - \overline{\delta M}_1^T\ \hat{\theta}_1
\end{aligned} \tag{2.14}$$

where the f_{u_i}, f_{ψ_i} ,..., $f_{M_{i+1}}$ are the element functions explicitly integrated from the formulation.

In each element function, γ and κ should be replaced with an expression that is function of F_B and M_B using the inverse of Eq. (2.11), along with the piezoelectric forcing vector $F_B^{(a)}$ and $M_B^{(a)}$. So do V_B and Ω_B with an expression function of P_B

and H_B. The modified functions become

$$
\begin{aligned}
f_{\psi_i} &= -C^T C^{ab} M_i - \frac{\Delta l_i}{2} C^T C^{ab} [e_1 + \widetilde{\{r(F_i + F_i^{(a)}) + t(M_i + M_i^{(a)})\}}] F_i \\
&\quad + \frac{\Delta l_i}{2} (\widetilde{\omega}_a C^T C^{ab} H_i + C^T C^{ab} \widetilde{V}_i P_i) + \frac{\Delta l_i}{2} (C^T C^{ab} H_i)^{\bullet} - \overline{m}_i \\
f_{F_i} &= u_i - \frac{\Delta l_i}{2} [C^T C^{ab} (e_1 + \{r(F_i + F_i^{(a)}) + t(M_i + M_i^{(a)})\}) - C^{ab} e_1] \\
f_{M_i} &= \theta_i - \frac{\Delta l_i}{2} (\Delta + \frac{\widetilde{\theta}_i}{2} + \frac{\theta_i \theta_i^T}{4}) C^{ab} \{t^T (F_i + F_i^{(a)}) + s(M_i + M_i^{(a)})\} \\
f_{\psi_{i+1}} &= C^T C^{ab} M_i - \frac{\Delta l_i}{2} C^T C^{ab} [e_1 + \widetilde{\{r(F_i + F_i^{(a)}) + t(M_i + M_i^{(a)})\}}] F_i \\
&\quad + \frac{\Delta l_i}{2} (\widetilde{\omega}_a C^T C^{ab} H_i + C^T C^{ab} \widetilde{V}_i P_i) + \frac{\Delta l_i}{2} (C^T C^{ab} H_i)^{\bullet} - \overline{m}_{i+1} \\
f_{F_{i+1}} &= -u_i - \frac{\Delta l_i}{2} [C^T C^{ab} (e_1 + \{r(F_i + F_i^{(a)}) + t(M_i + M_i^{(a)})\}) - C^{ab} e_1] \\
f_{M_{i+1}} &= -\theta_i - \frac{\Delta l_i}{2} (\Delta + \frac{\widetilde{\theta}_i}{2} + \frac{\theta_i \theta_i^T}{4}) C^{ab} \{t^T (F_i + F_i^{(a)}) + s(M_i + M_i^{(a)})\} \qquad (2.15)
\end{aligned}
$$

where the new symbols are submatrices of the flexibility matrix, *i.e.*,

$$
\begin{bmatrix} r & t \\ t^T & s \end{bmatrix} = [K]^{-1} \qquad (2.16)
$$

2.3.2 Displacement-based Form for Forward Flight Analysis

For possible simulation of the active rotor system in open and closed-loop control manner, a time domain formulation is needed. The multi-body dynamics code DYMORE, developed by Bauchau and co-workers [51], is based on similar geometrically-exact beam equations as presented before and it already couples these to the aerodynamics of Peters and He [56] (described next). This makes it a natural implementation to be modified for this study, which was done for this thesis.

DYMORE's original formulation adopts a similar geometrically-exact one-dimensional beam formulation as the one employed in the previous section, with the difference of being in displacement-based form. Therefore, the same cross-sectional analysis for active beams can be used with a properly modified version of the multi-body dynamics for passive beams so as to be applied to the analysis of active rotor system

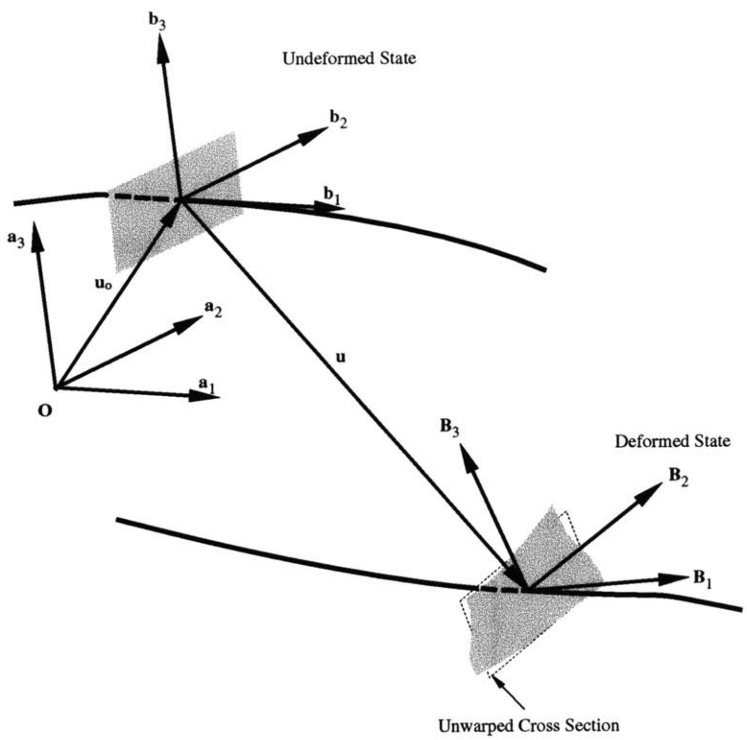

Figure 2-5: Beam in the undeformed and deformed configurations

during forward flight. The integral actuation forces and moments existing inside the blade structure are realized in the form of finite element loads to the passive beam in the modified time domain analysis. In what follows, an overview of the modifications to the formulation for the forward flight analysis is presented.

The kinetic and strain energies of the beam are

$$\begin{aligned} K &= \frac{1}{2}\int_0^L \left\{ \begin{array}{c} V_B \\ \Omega_B \end{array} \right\}^T \left\{ \begin{array}{c} P_B \\ H_B \end{array} \right\} dx_1 \\ U &= \frac{1}{2}\int_0^L \left\{ \begin{array}{c} \gamma_B \\ \kappa_B \end{array} \right\}^T \left\{ \begin{array}{c} F_B \\ M_B \end{array} \right\} dx_1 \end{aligned} \tag{2.17}$$

The velocity-displacement and strain-displacement relationships are expressed as

$$\left\{ \begin{array}{c} V_B \\ \Omega_B \end{array} \right\} = \left[\begin{array}{c} C^{ba^T} C^{Bb^T} \dot{\mathbf{u}} \\ C^{ba^T} C^{Bb^T} \boldsymbol{\omega} \end{array} \right] \tag{2.18}$$

$$\begin{Bmatrix} \gamma_B \\ \kappa_B \end{Bmatrix} = \begin{bmatrix} C^{ba^T} C^{Bb^T} (\mathbf{u}'_\text{o} + \mathbf{u}') - \mathbf{1} \\ C^{ba^T} C^{Bb^T} \mathbf{k} \end{bmatrix}$$

where $\boldsymbol{\omega}$ is the sectional angular velocity vector, with $\widetilde{\boldsymbol{\omega}} = \dot{C}^{Bb} C^{Bb^T}$; $\mathbf{u}_\text{o}$ defines the position of a point on the reference line before deformation, measured in a (See Fig. 2-5); $\mathbf{u}$ defines the displacement of a point to the deformed configuration, measured in a; and $\mathbf{k}$ is the sectional elastic curvature vector, with $\widetilde{\mathbf{k}} = C^{Bb'} C^{Bb^T}$. The relations presented in Eq. (2.18) are geometrically-exact, which means that they are valid for arbitrarily large displacements and rotations, although the strains are assumed to remain small. Virtual variations in sectional velocities and strains are

$$\begin{Bmatrix} \delta V_B \\ \delta \Omega_B \end{Bmatrix} = \begin{Bmatrix} \delta \dot{\mathbf{u}}^T + \delta \boldsymbol{\psi}^T \widetilde{\dot{\mathbf{u}}}^T \\ \delta \dot{\boldsymbol{\psi}}^T \end{Bmatrix} C^{Bb} C^{ba} \tag{2.19}$$

$$\begin{Bmatrix} \delta \gamma_B \\ \delta \kappa_B \end{Bmatrix} = \begin{Bmatrix} \delta \mathbf{u}'^T + \delta \boldsymbol{\psi}^T \widetilde{(\mathbf{u}'_\text{o} + \mathbf{u}')}^T \\ \delta \boldsymbol{\psi}'^T \end{Bmatrix} C^{Bb} C^{ba}$$

where $\delta \boldsymbol{\psi}$ is the virtual rotation measured in a, with $\delta \boldsymbol{\psi} = C^{Bb} C^{Ba^T}$.

The equations of motion of the beam are derived again from Hamilton's principle

$$\int_{t_i}^{t_f} [\delta(K - U) + \delta W] dt = 0 \tag{2.20}$$

where δW is the virtual work done by the externally applied forces. By using Eq. (2.17), one obtains

$$\int_{t_i}^{t_f} \left[\begin{Bmatrix} \delta V_B \\ \delta \Omega_B \end{Bmatrix}^T \begin{Bmatrix} P_B \\ H_B \end{Bmatrix} - \begin{Bmatrix} \delta \gamma_B \\ \delta \kappa_B \end{Bmatrix}^T \begin{Bmatrix} F_B \\ M_B \end{Bmatrix} + \delta W \right] dt = 0 \tag{2.21}$$

The sectional momenta and forces can be represented by the same constitutive relation as described in Eq. (2.11). The cross section analysis presented before provides the numerical values for both stiffness and inertial matrices, as well as the actuation vector.

Substituting Eqs. (2.19) and (2.11) into (2.21), and integrating by parts yield the governing equations as follows

$$
\begin{aligned}
&(C^{Bb}C^{ba}P_B)^{\bullet} - (C^{Bb}C^{ba}F_B)' = \hat{\mathbf{q}} + (C^{Bb}C^{ba}F_B^{(a)})' \qquad (2.22)\\
&(C^{Bb}C^{ba}H_B)^{\bullet} - \tilde{\dot{\mathbf{u}}}^T C^{Bb}C^{ba}P_B - (C^{Bb}C^{ba}M_B)' + (\widetilde{\mathbf{u}'_{\text{o}} + \mathbf{u}'})^T C^{Bb}C^{ba}F_B = \\
&\quad \check{\mathbf{q}} - (C^{Bb}C^{ba}M_B^{(a)})' + (\widetilde{\mathbf{u}'_{\text{o}} + \mathbf{u}'})^T C^{Bb}C^{ba}F_B^{(a)}
\end{aligned}
$$

where $\mathbf{q}^T = \lfloor \hat{\mathbf{q}}^T,\ \check{\mathbf{q}}^T \rfloor$ are the externally applied loads per unit span, measured in a. As described earlier, the effect of the actuation forcing vector is treated as an additional external load in the right-hand side of Eq. (2.22), while considering the transformation between the inertial frame and the deformed configuration.

2.4 Aerodynamic Analysis

2.4.1 Hover Aerodynamics

The external loads f_a and m_a along the B frame (Eq. 2.9) can be written as:

$$
\begin{aligned}
f_B &= \frac{1}{2}\rho_\infty c a \begin{Bmatrix} 0 \\ (W_{B_3} - \frac{c}{2}\Omega_1)W_{B_3} - \frac{c_{d_o}}{a}W_{B_2}^2 \\ (\frac{c}{2}\Omega_1 - W_{B_3})W_{B_2} - \frac{c}{4}\dot{V}_{B_3} + \frac{c^2}{16}\dot{\Omega}_1 \end{Bmatrix} \\
m_B &= -\frac{1}{32}\rho_\infty c^3 a \begin{Bmatrix} W_{B_2}\Omega_1 - \dot{V}_{B_3} + \frac{3c}{8}\dot{\Omega}_1 \\ 0 \\ 0 \end{Bmatrix} \qquad (2.23)
\end{aligned}
$$

which is based on a thin airfoil theory [57]. Here, ρ_∞ is the air mass density, c is the blade chord length, a is the lift curve slope, c_{d_o} is the profile drag coefficient, W_{B_2} and W_{B_3} are the components of the relative wind velocity in B frame, and Ω_1 is the component of the blade rotational speed along B_1 direction. By the transformation between the frames a and B, these forces and moments are converted to those in frame a. Additionally, W_{B_2} and W_{B_3} can be represented by the following expressions.

$$\begin{aligned} W_{B_2} &= e_2^T(V_B + C^{ba}C\lambda e_3) \\ W_{B_3} &= e_3^T(V_B + C^{ba}C\lambda e_3) \end{aligned} \tag{2.24}$$

where λ is the induced velocity. Since the current aerodynamic model contains the induced velocity terms explicitly, it is necessary to solve them simultaneously.

In this analysis, finite-state dynamic inflow equations based on Peters and He [50] are adopted, and can be summarized as

- Inflow expansion equation:

$$\bar{\lambda}(\bar{r}, \hat{\psi}, \bar{t}) = \sum_{\substack{m=0 \\ n=m+1,m+3,\ldots}}^{\infty} \phi_n^m(\bar{r})[a_n^m(\bar{t})\cos(m\hat{\psi}) + b_n^m(\bar{t})\sin(m\hat{\psi})] \tag{2.25}$$

where $\bar{r}$ is the non-dimensional radial station, $\hat{\psi}$ is the azimuthal location of the blade in the rotating frame, $\bar{t}$ is the non-dimensionalized time Ωt, and

$$\phi_n^m(\bar{r}) = \sqrt{(2n+1)H_n^m} \cdot \sum_{q=m,m+2,\ldots}^{n-1} \bar{r}^q \frac{(-1)^{\frac{(q-m)}{2}}(n+q)!!}{(q-m)!!(q+m)!!(n-q-1)!!}$$

$$H_n^m = \frac{(n+m-1)!!(n-m-1)!!}{(n+m)!!(n-m)!!}$$

where by definition

$$(m)!! = (m)(m-2)\ldots(2 \text{ or } 1),\ (-3)!! = -1,\ (-1)!! = 1,\ (0)!! = 1$$

- Inflow state equations:

$$\begin{bmatrix} [K_n^m] & \\ & [K_n^m] \end{bmatrix} \begin{Bmatrix} \{a_n^m\} \\ \{b_n^m\} \end{Bmatrix}^{\bullet} + \begin{bmatrix} [B_{nt}^m][V_n^m] & -m[K_n^m] \\ m[K_{nt}^m] & [B_{nt}^m][V_n^m] \end{bmatrix} \begin{Bmatrix} \{a_n^m\} \\ \{b_n^m\} \end{Bmatrix} =$$

$$\frac{1}{2}\left\{\begin{array}{c}\{\hat{\tau}_n^m\}^c \\ \{\hat{\tau}_n^m\}^s\end{array}\right\} \tag{2.26}$$

where

$$B_{nt}^m = (-1)^{\frac{(n+t-2m-2)}{2}}\sqrt{\frac{H_n^m}{H_t^m}}\sqrt{(2n+1)(2t+1)} \cdot \sum_{q=m,m+2,\ldots}^{n-1} H_q^m \frac{2q+1}{(t-q)(t+q+1)}$$

$[K_n^m]$: diagonal matrix with $K_n^m = \frac{1}{\pi}H_n^m$

$[V_n^m]$: diagonal matrix with

$$V_n^m = \begin{cases} \sqrt{3}\,|a_1^0| & \text{for } (m,n) = (0,1) \\ \\ 2\sqrt{3}\,|a_1^0| & \text{otherwise} \end{cases}$$

where the absolute value is added to ensure the symmetry about the state of zero inflow, or about the zero thrust level. The right-hand side of Eq. (2.26) is regarded as a pressure integral.

2.4.2 Forward Flight Aerodynamics

The same finite-state dynamic inflow aerodynamics model presented in the previous section is also used for forward flight analysis. This aerodynamic theory was originally developed for both hover and forward flight conditions [56]. Moreover, the forward flight part of this model was already implemented in DYMORE.

This model was constructed by applying the acceleration potential theory to the rotor aerodynamics problem with a skewed cylindrical wake. More specifically, the induced flow at the rotor disk was expanded in terms of modal functions. As a result, a three-dimensional, unsteady induced-flow aerodynamics model with finite number of states was derived in time domain. This model falls on an intermediate level of wake representation between the simplest momentum and the most complicated free wake methodologies. It does not require a severe computational effort, which is usually the case in those that involve the vortex filament theory. Therefore, this model is applicable for the problems of rotor aeroelastic stability, basic blade-passage vibrations, and higher-harmonic control studies.

2.5 Solution of the Aeroelastic System

2.5.1 Frequency Domain Solution for Hover Analysis

For the ATR hover study that follows, having a frequency domain solution is highly desirable. Therefore, combining Eq. (2.14), (2.23), and (2.24) yield a set of nonlinear equations. They can be separated into structural (F_S) and aerodynamic (F_L) terms and written as

$$F_S(X,\dot{X},V) - F_L(X,Y,\dot{X}) = 0 \tag{2.27}$$

where X is the column matrix of structural variables, Y is a column matrix of inflow states and V is the magnitude of the electrical field distribution shape. In Eq. (2.27), V is explicitly included in F_S due to the inverse expression of the first constitutive relation, Eq. (2.11), and the linear piezoelectric constitutive relation as follows:

$$\begin{aligned}
\left\{ \begin{array}{c} \gamma \\ \kappa \end{array} \right\} &= [K]^{-1} \left\{ \begin{array}{c} F_B + F_B^{(a)} \\ M_B + M_B^{(a)} \end{array} \right\} \\
&= [K]^{-1} \left\{ \begin{array}{c} F_B \\ M_B \end{array} \right\} + [K]^{-1} \left\{ \begin{array}{c} F_B^{(a)} \\ M_B^{(a)} \end{array} \right\} \\
&= \left\{ \begin{array}{c} \gamma_{\text{mechanical}} \\ \kappa_{\text{mechanical}} \end{array} \right\} + \left\{ \begin{array}{c} \gamma^{(a)} \\ \kappa^{(a)} \end{array} \right\} V
\end{aligned} \tag{2.28}$$

where $\gamma_{\text{mechanical}}$ and $\kappa_{\text{mechanical}}$ are the mechanical strain components.

Similarly we can separate the inflow equations, Eq. (2.26), into a pressure component (F_P) and an inflow component (F_I) yielding

$$-F_P(X,Y) + F_I(Y,\dot{Y}) = 0 \tag{2.29}$$

The solutions of interest for the two coupled sets of equations (Eqs. 2.27 and 2.29) can be expressed in the form

$$\left\{ \begin{array}{c} X \\ \\ Y \end{array} \right\} = \left\{ \begin{array}{c} \bar{X} \\ \\ \bar{Y} \end{array} \right\} + \left\{ \begin{array}{c} \check{X}(t) \\ \\ \check{Y}(t) \end{array} \right\} \tag{2.30}$$

where $(\bar{\ })$ denotes steady-state solution and $(\check{\ })$ denotes the small perturbation about it.

For the steady-state solution, one has to solve a set of algebraic nonlinear equations originated from Eq. (2.27) and Eq. (2.29):

$$\begin{aligned} F_S(\bar{X}, 0, \bar{V}) - F_L(\bar{X}, \bar{Y}, 0) = 0 \\ -F_P(\bar{X}, \bar{Y}) + F_I(\bar{Y}, 0) = 0 \end{aligned} \tag{2.31}$$

The Jacobian matrix of the above set of nonlinear equations can be obtained analytically and, even with the modifications caused by the active material embedded in the structure, it is found to be very sparse. Note that the presence of the actuation in the blade changes the original terms of the Jacobian in a similar manner it does in Eq. (2.14). The steady-state solution can be found very efficiently using Newton-Raphson method.

In order to investigate the dynamic response of the blade with respect to voltage applied to the embedded anisotropic strain actuator, a state-space representation is required once the steady-state solution is obtained. Perturbing Eqs. (2.27) and (2.29) using Eq. (2.30) about the calculated steady state yields

$$\begin{gathered} \left[\begin{array}{cc} \frac{\partial F_S}{\partial X} - \frac{\partial F_L}{\partial X} & -\frac{\partial F_L}{\partial Y} \\ -\frac{\partial F_P}{\partial X} & \frac{\partial F_I}{\partial Y} - \frac{\partial F_P}{\partial Y} \end{array} \right]_{\substack{X=\bar{X} \\ Y=\bar{Y}}} \left\{ \begin{array}{c} \check{X} \\ \\ \check{Y} \end{array} \right\} + \left[\begin{array}{cc} \frac{\partial F_S}{\partial \dot{X}} - \frac{\partial F_L}{\partial \dot{X}} & 0 \\ 0 & \frac{\partial F_I}{\partial \dot{Y}} \end{array} \right]_{\substack{X=\bar{X} \\ Y=\bar{Y}}} \left\{ \begin{array}{c} \dot{\check{X}} \\ \\ \dot{\check{Y}} \end{array} \right\} + \\ \left[\begin{array}{cc} \frac{\partial F_S}{\partial V} & 0 \\ 0 & 0 \end{array} \right]_{\substack{X=\bar{X} \\ Y=\bar{Y}}} \{ V \} = \left\{ \begin{array}{c} 0 \\ \\ 0 \end{array} \right\} \end{gathered} \tag{2.32}$$

from which the transient solution can be found. Since the aerodynamics is expressed as coupled through the blades, the system equations must be transformed to multi-blade coordinates resulting in a form of multi-harmonic series. In the present hover analysis, only the collective components of those need to be considered. Detailed expressions of the sub-matrices included in Eq. (2.32) are provided in Appendix A. Eq. (2.32) constitutes the first part of a state-space representation, and can be written in the following form

$$\mathbf{E}\dot{\check{X}} = \mathbf{A}\check{X} + \mathbf{B}V \tag{2.33}$$

In order to extract the blade response at any locations, e.g., strain quantities corresponding to the sensors embedded along the blade, an output equation can be established. This is accomplished by inverting the first constitutive relation, Eq. (2.11), for the i-th element

$$\begin{aligned}\begin{Bmatrix}\gamma\\ \kappa\end{Bmatrix}_i &= [K]_i^{-1}\begin{Bmatrix}F_B\\ M_B\end{Bmatrix}_i + [K]_i^{-1}\begin{Bmatrix}F_B^{(a)}\\ M_B^{(a)}\end{Bmatrix}_i\\ &= [K]_i^{-1}[N]\check{X}_i + \begin{Bmatrix}\gamma^{(a)}\\ \kappa^{(a)}\end{Bmatrix}_i V\end{aligned} \tag{2.34}$$

where $[N]$ is a matrix which extracts F_B and M_B vectors from the mixed-form solution vector $\check{X}_i$. $\gamma^{(a)}$ and $\kappa^{(a)}$ are the induced strains per unit voltage, as already presented in Eq. (2.28), and their numerical values are provided from the cross-sectional analysis. Enough numbers of beam elements are used so that the strain may be assumed constant within a single element. Then, the strain quantites at desired location can be extracted by referring to that of the relevant element

$$\begin{aligned}\begin{Bmatrix}\gamma\\ \kappa\end{Bmatrix}_{\text{desired}} &= [L]\begin{Bmatrix}\gamma\\ \kappa\end{Bmatrix}_i\\ &= [L][K]_i^{-1}[N]\check{X}_i + [L]\begin{Bmatrix}\gamma^{(a)}\\ \kappa^{(a)}\end{Bmatrix}_i V\end{aligned} \tag{2.35}$$

where $[L]$ is a matrix containing unity only at the diagonal of the relevant element, and all other zeros. Eq. (2.35) becomes the second part of a state-space representation with a generalized form as

$$y = \mathbf{C}\check{X} + \mathbf{D}V \tag{2.36}$$

where y is the output vector corresponding to the sensors embedded along the blade.

Frequency response function of the blade can be calculated using Laplace transform of the simultaneous equations which are composed of Eqs. (2.33) and (2.36)

$$\frac{\bar{y}(s)}{\bar{V}(s)} = \mathbf{C}(\mathbf{E}s - \mathbf{A})^{-1}\mathbf{B} + \mathbf{D} \tag{2.37}$$

Note that the coefficient matrix $\mathbf{E}$ is usually singular due to the mixed formulation of the beam model.

2.5.2 Time Domain Solution for Forward Flight Analysis

While the hover analysis presented in the previous section seeks frequency-domain quantities of the blade response function, the forward flight analysis performs a direct time integration of the blade response due to an integral actuation. This is needed since system identification and open- and closed-loop simulations, all in time, must be conducted. DYMORE, the original passive blade dynamics model, adopts a time-discontinuous integration scheme with energy decaying characteristics in order to avoid high frequency numerical oscillation [51, 58]. Such a high frequency oscillation usually occurs during a finite element time integration of a complex multi-body dynamic system. Details of the energy decaying time integration of the beam formulation are found in [51, 58], and briefly summarized in Appendix B.

DYMORE is also capable of adjusting its time step size automatically to maintain stability and accuracy of the integration scheme. Another advantage of adopting multi-body formulation here is that the total shear force and moment exerted by the rotor system can be easily extracted. By adding and monitoring a rigid body element which represents a rotor shaft, the degree of vibratory load variation of the entire rotor system can be directly evaluated. Finally, the control sensitivity functions due to high voltage actuation input for different forward flight conditions can be calculated by Fourier transform of the time response of the blade or the entire active rotor system.

Chapter 3

Experimental Setup

3.1 Overview

In the previous chapter, an analytical framework is proposed and established to predict aeroelastic behavior of an active rotor system and numerically evaluate its effectiveness in vibration reduction. At the same time, an experimental effort was pursued to substantiate the present integral blade actuation concept through a small-scale wind-tunnel model. Results from these experiments are also utilized for correlation with the predictions from the proposed analytical framework. Wind-tunnel tests were conducted at NASA Langley's Transonic Dynamics Tunnel as part of the collaboration between the U.S. Army Research Laboratory, at NASA Langley Research Center, and MIT.

The ATR prototype blade was previously designed and successfully manufactured. Preliminary bench testing was conducted to confirm its basic structural characteristics. Details of the relevant work are found in [45], and summarized in this chapter. The prototype blade is used for hover test with three other dummy blades to compose the four-bladed fully-articulated rotor. Blade response under rotating condition is investigated in the hover test. A minor modification is added to the prototype blade design, and four active blades are fabricated based on it. Using four-active-bladed rotor system, forward flight test is performed in an open-loop control manner. The results from the hover, and forward flight tests will be correlated with those predicted by the proposed analytical framework in Chapters 4 and 5.

3.2 Blade Design

3.2.1 ATR Prototype Blade

The aeroelastic design of the active twist blade was basically accomplished within the framework presented here and it is detailed in [33, 45]. The basic requirements for the ATR prototype blade came from an existing passive blade used by NASA Langley. The baseline (passive) system has been well studied and characterized over the years, and is representative of a generic production helicopter [40]. The new ATR blade is designed based on the external dimensions and aerodynamic properties of the existing baseline blade to be tested in heavy gas (R134a) medium. Table 3.1 summarizes the general dimension and shape characteristics of the baseline blade, and Table 3.2 presents the main structural characteristics of the ATR prototype blade design.

Table 3.1: General properties of the existing baseline rotor blade (considering heavy gas test medium)

Rotor type	Fully articulated
Number of blades, b	4
Blade chord, c	10.77 cm
Blade radius, R	1.397 m
Solidity, $bc/\pi R$	0.0982
Airfoil section	NACA 0012
Blade pretwist	$-10°$ (linear from $0R$ to tip)
Hinge offset	7.62 cm
Root cutout	31.75 cm
Pitch axis	25% chord
Elastic axis	25% chord
Center of gravity	25% chord
Lock number	9.0
Tip Mach number	0.6
Centrifugal loading at tip	738.5 g
Rotor speed	687.5 rpm
Rotor overspeed	756 rpm

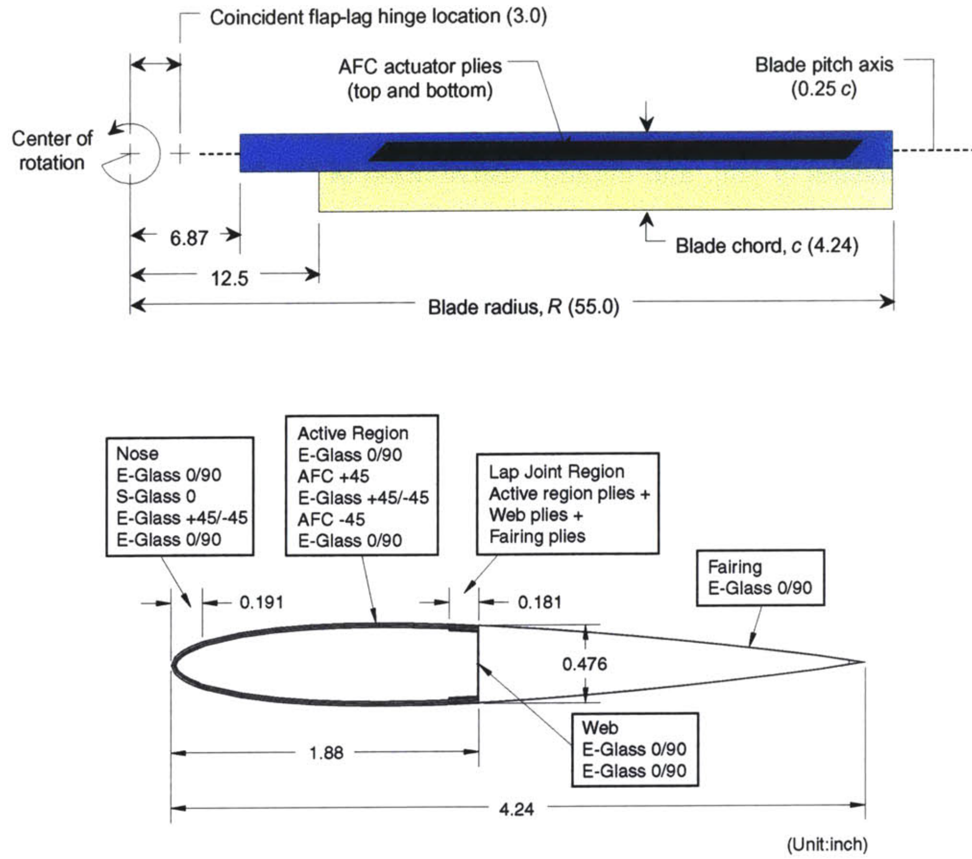

Figure 3-1: Planform and cross-section of the ATR prototype blade (Dimensions are in inches.)

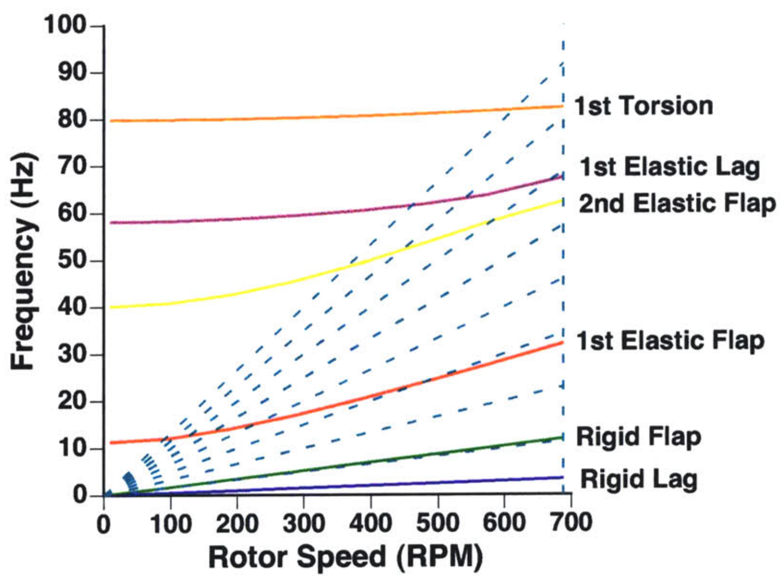

Figure 3-2: Fan plot of the ATR prototype blade from the proposed analysis

Fig. 3-1 shows basic blade planform and cross section characteristics selected, and the fan plot of the prototype blade analyzed by the proposed framework is presented in Fig. 3-2. The material properties of the passive prepregs and active ply are found in the appendices of [45], and detailed distribution of the individual AFC packs in the prototype blade is described in Appendix C.

Table 3.2: Theoretical characteristics of the ATR prototype design

	ATR Design
Mass per unit span (kg/m)	0.6960
Center of gravity Tension axis	24.9 % 30.8 %
EA (N) GJ (N-m^2) EI_{flap} (N-m^2) EI_{lag} (N-m^2)	$1.637\ 10^6$ $3.622\ 10^1$ $4.023\ 10^1$ $1.094\ 10^3$
Lock No.	9.0
Section torsional inertia (kg-m^2/m)	$3.307\ 10^{-4}$
1st torsion frequency @ 687.5 RPM	7.38/rev
Twist actuation @ 0 RPM, 4,000 V_{pp}/1,200 V_{DC} (peak-to-peak, deg/m)	4.52
Maximum strain at the worst loading condition (μstrain) (1) Fiber (2) Transverse (3) Shear	 2,730 2,730 5,170

The selected concept [33] and final structural design of the ATR prototype blade employs a total of 24 AFC packs placed on the front spar only, and distributed in 6 stations along the blade span. Even though it does not reflect the highest actuation authority concept, the chosen one satisfies all the requirements and provide a reasonable cost option (where most of the cost comes from the AFC packs). The AFC laminae are embedded in the blade structure at alternating $\pm 45°$ orientation angles to maximize the twist actuation capabilities of the active plies. With an even number of AFC plies, it is also possible to keep the passive structure of the rotor blade virtually elastically uncoupled. This allows independent actuation of blade torsional motion with practically no bending or axial actuation. The ATR prototype blade was originally expected to achieve static twist actuation amplitudes of between 2.0° to 2.5°, and hovering flight dynamic twist actuation amplitudes of 2.0° to 4.0° (based on CAMRAD II and PETRA simulations [40]) at the extended cycle of maximum applied voltage of 4,000 V_{pp}/1,200 V_{DC}. Structural integrity of the new blade design was evaluated based on the worst loading conditions, which are expected to occur within the rotor system operating envelope. In this design, forward flight with the maximum speed is selected as the design loading condition. Then, the largest magnitudes of the aerodynamic loads are extracted and combined with the centrifugal loads in order to give the worst loading values. A safety factor of 1.5 was used.

3.2.2 ATR Test Blade with Modification

Even though experimental structural characteristics and twist performance of the prototype blade compared well with design goals [45], a concern was raised regarding its structural integrity, especially affected by the fatigue loadings. There was not enough experimental evidence that the prototype blade had the fatigue life according to the criterion employed by NASA Langley Research Center for wind-tunnel testing models [59]. Also, an empirical formula adopted by the contractor who planned to build the ATR test blades for forward flight testing indicated that the design should be improved in fatigue [60]. A modification was applied to the design of the prototype blade to compensate this shortcoming. Different lay-up configurations were suggested to increase the structural integrity within the range that its characteristics is not greatly changed from that of the prototype blade. As a result, only one ply of E-Glass fabric prepreg in 0/90° was added to the front spar assembly in order to further withstand centrifugal loading. Using the active cross-sectional analysis previously described, basic structural characteristics were computed for the updated configuration, and listed in Table 3.3. The material properties of the passive prepregs and the AFC plies used in the test blades manufacturing are slightly changed from those in the prototype blade, and are summarized in Appendix D.

Table 3.3: Basic characteristics of the modified ATR blade design

	ATR Design
Mass per unit span (kg/m)	0.6998
Center of gravity Tension axis	17.9 % 34.4 %
EA (N) GJ (N-m^2) EI_{flap} (N-m^2) EI_{lag} (N-m^2)	1.787 10^6 3.143 10^1 4.419 10^1 1.153 10^3
Section torsional inertia (kg-m^2/m)	3.810 10^{-4}
Twist actuation @ 0 RPM, 4,000 V_{pp}/1,200 V_{DC} (peak-to-peak, deg/m)	4.92

3.3 Prototype Blade Manufacturing

Two test articles were fabricated prior to the ATR prototype blade manufacturing. The blade root is a co-cure assembly of graphite/epoxy prepreg, which was completely modified from the original design of a metal block attachment. The AFC packs, manufactured by Continuum Control Corporation, Billerica, Massachusetts, were inserted in the blade, and individually tested for their actuation and capacitance. Those were characterized at two different cycles: 3,000 V_{pp}/600 V_{DC} ("representative cycle") and 4,000 V_{pp}/1,200 V_{DC} ("extended cycle") for 1 and 10 Hz. A flexible circuit was inserted to distribute the high voltages into the AFC packs, and it was also successfully tested for high-voltage isolation prior to the blade manufacturing. For the ATR prototype blade, a total of 10 sets of strain gauges were embedded inside the spar assembly. These strain gauges were used to monitor the deformation and load level during spinning, and also to assess the individual AFC pack actuation during the bench test. Two tantalum weight pieces were aligned and attached at the nose and web for inertia balancing. Once the spar was cured, the six flexible circuit layers were soldered to the corresponding AFC flap connectors using high-temperature solder. The fairing was attached in a second cure. The final shape of the ATR prototype is shown in Fig. 3-3.

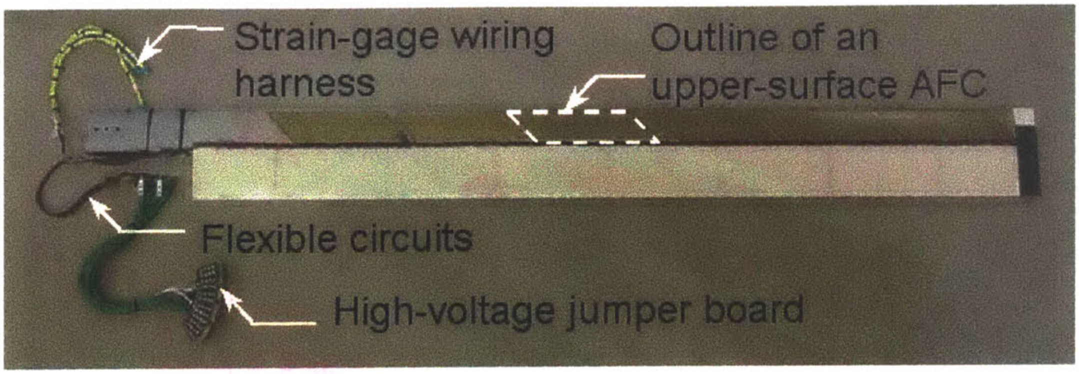

Figure 3-3: ATR prototype blade

3.4 Aeroelastic Tests

3.4.1 Wind Tunnel

The Langley Transonic Dynamics Tunnel (TDT), whose schematic is shown in Fig. 3-4, is a continuous-flow pressure tunnel capable of speeds up to Mach 1.2 at stagnation pressures up to 1 atm. The TDT has a 16-ft square slotted test section that has cropped corners and a cross-sectional area of 248 ft^2. Either air or R-134a, a heavy gas, may be used as a testing medium. The TDT is particularly adequate for rotorcraft aeroelastic testing due to several advantages associated with the heavy gas. At first, the high density of the testing medium allows model rotor components to be heavier, and this satisfies the structural design requirements easily while maintaining dynamic scaling. Second, the low speed of sound in R-134a (approximately 170 m/sec) allows lower rotor rotational speeds to match full-scale hover tip Mach number. Finally, the high-density environment increases Reynolds number throughout the testing envelope, which enables more accurate modeling of the full-scale aerodynamic environment of the rotor system. Both hover and forward-flight tests of the ATR system are primarily conducted in the heavy gas testing medium at a constant density of 2.432 kg/m^3.

3.4.2 Test Apparatus

The Aeroelastic Rotor Experimental System (ARES) helicopter testbed, whose schematic drawing is illustrated in Fig. 3-5, is used for both hover and forward-flight

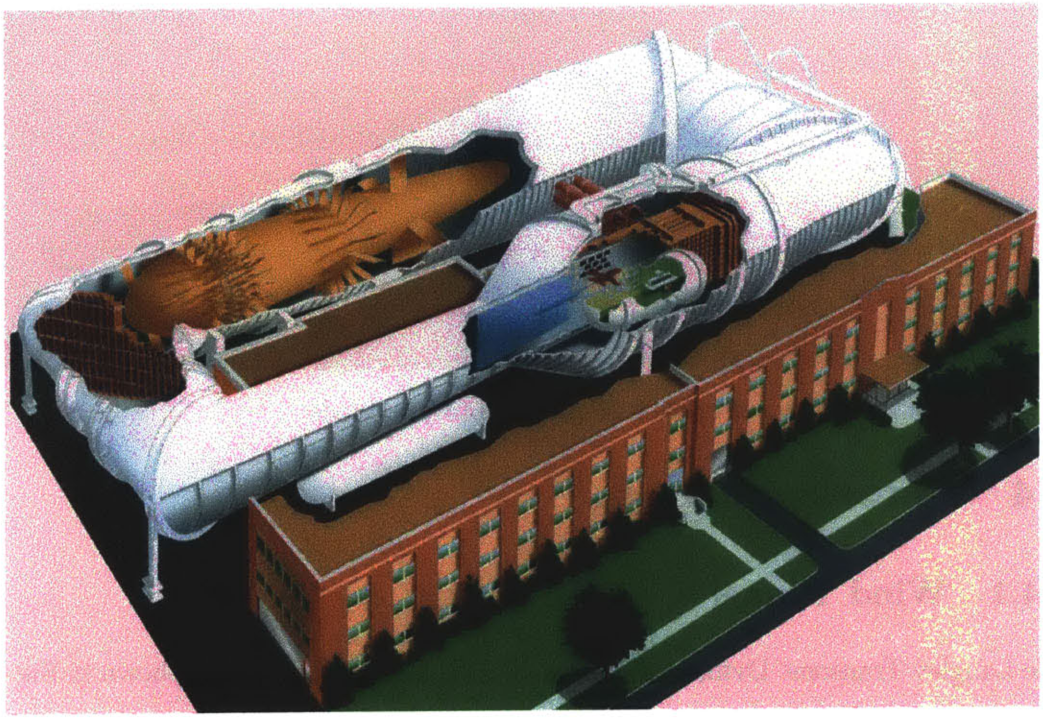

Figure 3-4: The Langley Transonic Dynamic Tunnel (TDT) [48]

testing. The ARES is powered by a variable-frequency synchronous motor rated at 47-HP output at 12,000 rpm. The motor is connected to the rotor shaft through a belt-driven, two-stage speed reduction system. Rotor control is achieved by a conventional hydraulically-actuated rise-and-fall swashplate using three independent actuators. Similarly, inclination angle of the rotor shaft is controlled by a single hydraulic actuator.

Instrumentation on the ARES testbed permits continuous display of model control settings, rotor speed, rotor forces and moments, fixed-system accelerations, blade loads and position, and pitch link loads. All rotating-system data are transferred through a 30-channel slip ring assembly to the testbed fixed-system. An additional slip ring enables the transfer of high-voltage power from the fixed-system to the rotating-system for actuation of the AFC actuators embedded in the ATR blades. A six-component strain gauge balance placed in the fixed-system 21.0 inches below the rotor hub measures rotor forces and moments. The strain gauge balance supports the rotor pylon and drive system, pitches with the model shaft, and measures all of

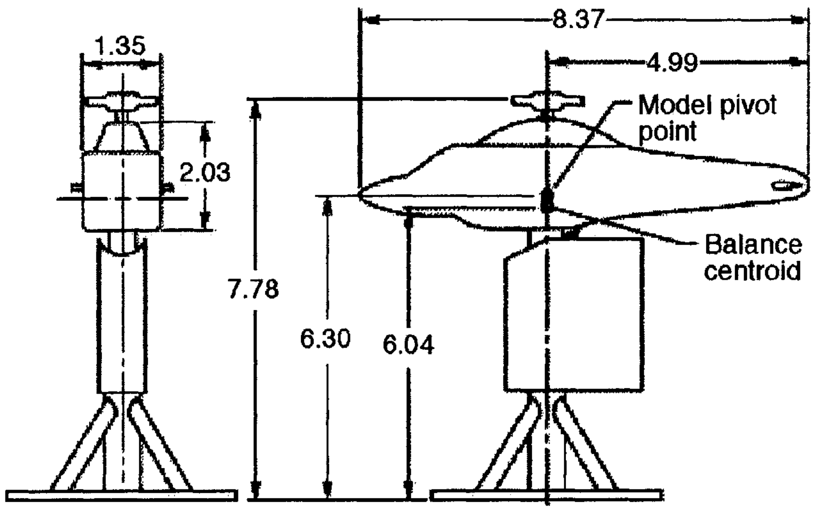

Figure 3-5: Schematic of the Aeroelastic Rotor Experimental System (ARES) helicopter testbed (All dimensions are in ft.) [48]

the fixed-system forces and moments generated by the rotor model. A streamlined fuselage shape encloses the rotor controls and drive system. However, the fuselage is isolated from the rotor system such that fuselage forces and moments do not contribute to the loads measured by the balance.

Fig. 3-6 shows the ATR blades mounted on the ARES helicopter testbed in the TDT. For this configuration a four-bladed articulated hub with coincident flap and lag hinges is used on the ARES. The feathering bearing for the hub is located outboard of the flap and lag hinges, and trailing pitch links are used. The hub is configured such that pitch-flap coupling of 0.5 (flap up, leading-edge down) is obtained and the lag-pitch coupling is minimized. During the hover testing, the test section floor, and the ARES testbed, is lowered approximately 3 ft to allow the rotor wake to vent into the surrounding plenum volume, thus reducing recirculation effects. (In Fig. 3-6, the test section floor is shown in its normal, raised position.).

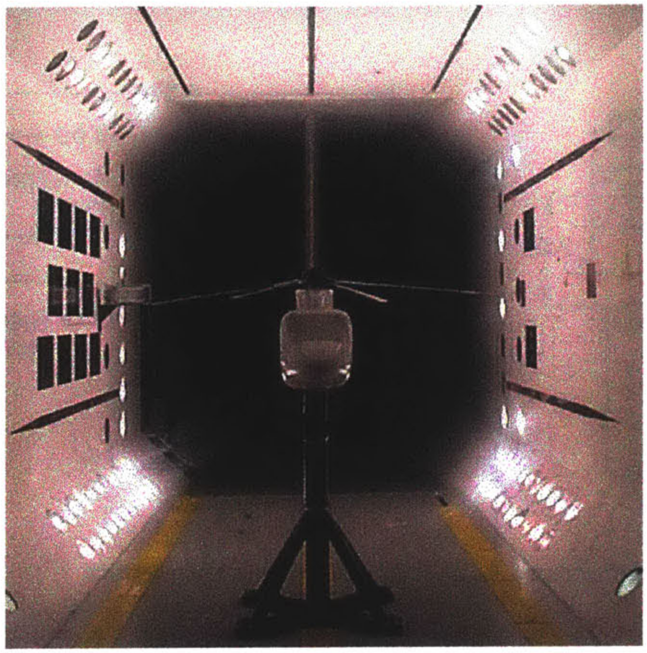

Figure 3-6: Aeroelastic Rotor Experimental System (ARES) 9-ft diameter rotor testbed in Langley Transonic Dynamic Tunnel (TDT) with the ATR prototype blade.

3.4.3 Hover Testing

The ATR prototype blade is used with three other similar passive blades for hover testing. The four-bladed fully-articulated rotor system was mounted inside the NASA Langley Transonic Dynamics Tunnel as shown in Fig. 3-6. The blade tracking and balance were accomplished by adjusting the active blade weight and its pitch angle. This was done so the system could be checked in heavy gas. The hover testing conditions performed with the ATR prototype blade is presented in Table 3.4.

Initial efforts during the hover set up were aimed at solving difficulties with the high-voltage power delivery system since this system was installed in the ARES for the first time. Initial checks were conducted at nonrotating condition, similarly to the bench testing. Once confidence was gained in the high-voltage system, hover testing was initiated. Initial hover tests were in air at low rotational speeds, which progressed incrementally to the rotor design speed. Then, the tunnel test section was closed and pressurized with heavy gas. Again, all these conditions are summarized in Table 3.4.

For each test condition, computer-controlled sine dwell signals ranging from 0 Hz

Table 3.4: Hover test conditions for the ATR prototype blade

Testing medium	Density (kg/m^3)	Rotor speed (rpm)	Collective pitch (deg)	Voltage amplitude (V)
Air	1.225	400	0	100
		400	0	500
		400	0	750
		400	0	1000
Air	1.225	688	0	500
		688	0	1000
		688	4	500
		688	4	1000
		688	8	500
		688	8	1000
		688	12	1000
Heavy gas	2.432	688	0	500
		688	0	1000
		688	4	500
		688	4	1000
		688	8	500
		688	8	1000
Heavy gas	1.546	688	8	1000
	1.984	688	8	1000
	2.432	688	8	1000
	2.432	619	8	1000

to 100 Hz, in 5 Hz increments, at amplitudes of up to 1000 V were applied to the ATR prototype blade. Data from the blade strain gauge bridges, the ARES testbed, and the high-voltage amplifier channels were recorded at a rate of 3,000 samples-per-second by the computer control system for 5-second durations. The signals acquired through the channels during the test are listed in Table 3.5. Even though different loads were measured in the test, correlation with the analytical framework is limited to the blade torsion moments in this thesis. The total rotor loads were measured at the fixed-system balance, and since the dynamics of the fuselage model (housing motors, slip rings for data and power, etc.) is not completely available, these quantities are not included in the present hover analysis model.

The acquired signal data in time were processed to obtain the transmissibility of the system with respect to the sinusoidal actuation of the active blade in frequency

Table 3.5: Data channels for the hover test.

Signal	Components
Rotor system balance	Axial, Normal, Pitch, Roll, Side, Yaw
Active blade deformation	(6) Torsion, Chordwise Bending (3) Flap Bending
Rotor control system	Collective, Cyclic, Flapping, Lead-lagging
Pitch link load	Blade-1, Blade-3
Voltage	Blade-1
Current	Blade-1

domain. The undesirable noise was removed from the data by adopting a simple smoothing algorithm. The transfer function can be obtained by the output signal divided by input signal, both of which were transformed to frequency-domain by a fast-Fourier transform (FFT) technique. Since sine dwell signals were used in the test, one set of data corresponding to each discrete frequency generated a single point in the transfer function plot.

3.4.4 Forward Flight Testing

The four-active-bladed rotor system was used for forward flight testing in Langley's TDT. Testing was conducted to examine the effect of active twist on fixed- and rotating-system vibratory loads and acoustic noise. Table 3.6 presents the conditions tested in terms of advance ratio μ, and rotor shaft inclination angle α_S. The suggested conditions represent sustained 1-g level flight from low to high speed, and descending flight. For each condition tested, the rotor was set to a rotational speed of 688 rpm, and trimmed to a nominal thrust coefficient C_T of 0.0066. At the same time, the collective and cyclic pitch settings were adjusted so that the rotor could reach a steady-state equilibrium. This equilibrium was maintained once the first-harmonic blade flapping was approximately 0.1° [49], and is referred to as "baseline" condition since no actuation was applied.

Once the steady-state equilibrium condition was obtained, either sine-dwell or

Table 3.6: Forward flight test conditions for the ATR system

	$\mu =$ 0.14	$\mu =$ 0.17	$\mu =$ 0.20	$\mu =$ 0.233	$\mu =$ 0.267	$\mu =$ 0.30	$\mu =$ 0.333	$\mu =$ 0.367
$\alpha_s = +8°$	×							
$\alpha_s = +5°$	×							
$\alpha_s = +4°$	×	×	×	×	×			
$\alpha_s = +2°$	×			×	×			
$\alpha_s = +1°$		×						
$\alpha_s = 0°$	×		×	×	×			
$\alpha_s = -1°$	×	×	×					
$\alpha_s = -2°$	×			×	×			
$\alpha_s = -4°$						×	×	
$\alpha_s = -6°$							×	×
$\alpha_s = -8°$							×	

sine-sweep signal was applied by the high-voltage amplifiers. In case of sine-dwell signals, only 3P, 4P, 5P frequency components were considered since (b+1, b, b-1) frequency components are to influence significantly b-bladed rotor system. Available blade control modes include collective twist, differential twist, and an Individual Blade Control (IBC) mode where each blade actuates according to a prescribed schedule with respect to its position in the azimuthal location. In collective twist mode, all the blades are under the same synchronous twist actuation signals, while those of an opposite sign are transferred to the blade at opposite azimuthal location (e.g., Blade No. 1 and 3) in differential mode. For IBC actuation mode, the actuation on each blade behaves in the same phase at a specific azimuthal location.

Also, a sweeping algorithm over control phase angle was considered within the IBC scheme. It is worth noting that although control phase is indicated by the rotor azimuth (i.e., 0° control phase is coincident with 0° azimuth), control phase is not equivalent to rotor azimuth. For example, a 3P twist actuation with control phase of 180° would impose the maximum twist control at a rotor azimuth of 60°. The second and third cycles would achieve maximum twist control at 180° and 300°, respectively. This will be revisited in the IBC signal generation for the forward flight analysis in Section 5.3.2.

The sine-sweep signal was also used for experimental system identification purpose, with varying frequency from 0.1P to 9P linearly over a determined time interval, and with sweeps over the control phase angle around 360°. The signal generated for this system identification purpose is explained in detail in Section 6.2.

Instrumentation during the forward flight testing included the same physical quantities as measured in the hover test presented in Table 3.5. Additional accelerometers were embedded at the tip of the active blades to measure their dynamic twist. Also, PMI measurement was conducted in the tunnel to record the overall blade motion during the test.

Chapter 4

Characteristics of the ATR Blade on the Bench and in Hover

4.1 Overview

Using the ATR prototype blade, two major tests are executed regarding its dynamic response induced by a time-varying electric field applied to the embedded AFC actuators. Bench top non-rotating actuation testing is conducted first. Then, the prototype blade is used to build an active rotor system with the other dummy blades to be tested in hover condition. Details of the hover experiments plan are already introduced in Chapter 3. All these test data are compared with the results from the analytical framework presented before, especially the model which obtains the solution of the aeroelastic system in frequency domain.

4.2 Basic Bench Testing

Different characterization tests were performed on the ATR prototype blade at bench top condition in order to validate the design and manufacturing procedures, and to verify the performance of the prototype article. Also numerical results obtained from the proposed analytical framework were compared with the test data at each stage of the experiments since the model was developed and expanded to enable variety of analyses, such as static twist actuation performance. Detailed description of the previous preliminary tests and the correlation with the numerical results are presented in [45]. Among the tests conducted on the prototype blade, static twist actuation measurement is updated using different apparatus, and described in this section.

For the non-rotating results, the prototype blade was mounted on the bench in a single-cantilevered condition. Preliminary tests were performed on the spar first, and then on the whole assembly (spar + fairing) at very low excitation frequency (1 Hz). The tip twist angle measurements along with model predictions are presented in Table 4.1. Due to electric failures of the packs at higher voltages [45], tests were limited to a 2,000 V_{pp}/0 V_{DC} level. Based on the AFC material characterization conducted on this voltage level, the theoretical actuation prediction using the model developed in this study was conducted. However, as one can see, the analytical model overpredicts the low-frequency actuation by 20% to 27% considering the laser displacement sensor (LDS) measurements. Nonetheless, the quasi-static cross-section actuation model had been validated well against other experimental data, and errors of no more than 15% were expected based on the available AFC material data [41]. Later, closer inspection of the procedure used to perform those measurement indicated the potential source of error. A metal strip taped to the blade and used to reflect laser targets was not totally rigid, and its motion induced a lower reading on the LDS system.

Therefore, another set of tests were performed using the Projection Moirè Interferometry (PMI) at NASA Langley [49]. The PMI is a noninvasive mean of remotely measuring shape, displacement, or deformation of an object. The setup used in the current measurements have an average accuracy of $0.056° \pm 0.042°$ for the large scale system and $0.010° \pm 0.012°$ for the small scale one for the blade rotation angle between 0° and 1° ("large" and "small scale systems" are associated with the field of view, with the "large" one covering most of the blade's active region and the "small scale" being only about 30% span). Based on 18 working AFC actuators, the measurement on the peak-to-peak tip twist at 2,000 V_{pp} is also included in Table 4.1. By correcting the twist actuation to account for the difference in the number of working AFCs, the

Table 4.1: Peak-to-peak tip twist actuation of the ATR prototype blade (2,000 V_{pp}/0 V_{DC}, 1 Hz)

	Present Model	**Experiment (LDS)**	**Experiment (PMI)**
Spar only	1.4°	1.1°	-
Spar+fairing	1.2°	1.0°	1.1°*

* only 18 active AFC packs.

experimental result from the PMI test is about 15% higher than the original LDS measurements, and the difference from the analytical model is within 12%. This discrepancy was expected and arises from variation in AFC material properties (between packs) and uncertainty in the material properties used in the analysis.

4.3 Non-Rotating Frequency Response

The non-rotating dynamic characteristics of the prototype blade can be evaluated from the frequency response of an applied sinusoidal excitation to the AFC actuators. Figs. 4-1 – 4-4 show the results of the laser displacement sensor (for tip twist angle), the blade strain gauges readings, and the predictions of the frequency domain analysis at several blade stations as function of the AFC actuation.

As one can see, the first torsional mode is clearly identified at approximately 85 Hz, and this result matches well with model prediction. The model neither includes structural nor stationary aerodynamic damping, resulting in infinite peaks at resonance. This already indicates that some structural damping should be added to the model. Once the aerodynamics is included in the problem, its damping will bring that to a finite amplitude. While the strain results could be obtained at high excitation voltages, the dynamic tip twist was measured at low voltages due to the limitation on the range of the laser sensors. At 400 V_{pp}, the peak-to-peak tip twist response of the blade is approximately 3.5°. Such an increased dynamic response around the first torsional natural frequency is expected to affect the twist response over the frequency range of interest when the blade is rotating. It makes the frequency response

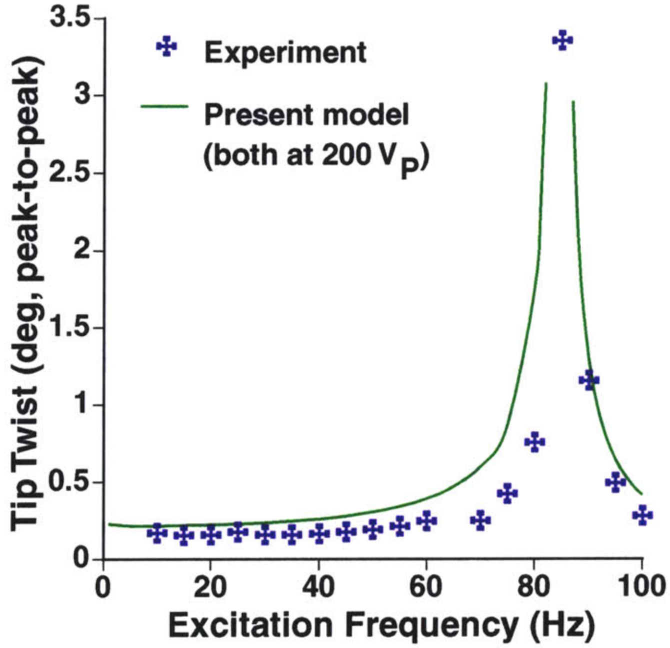

Figure 4-1: Tip twist response of the ATR prototype blade on the bench

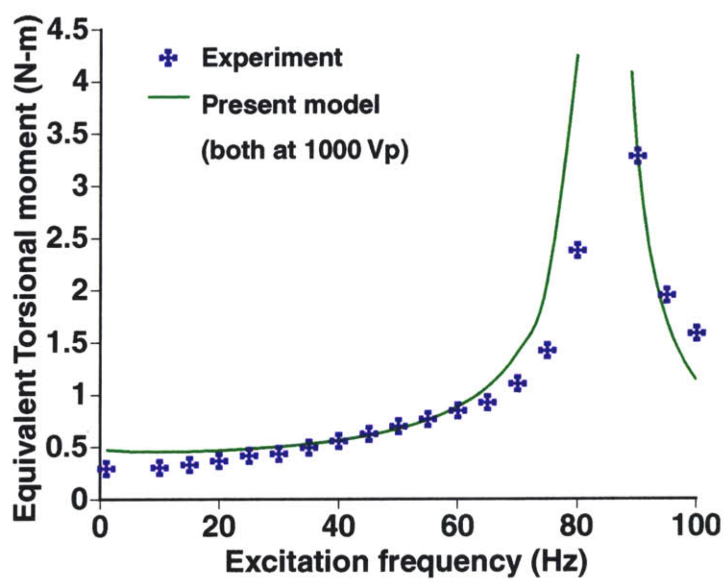

Figure 4-2: Equivalent torsional moment at 31% blade radius of the ATR prototype blade on the bench

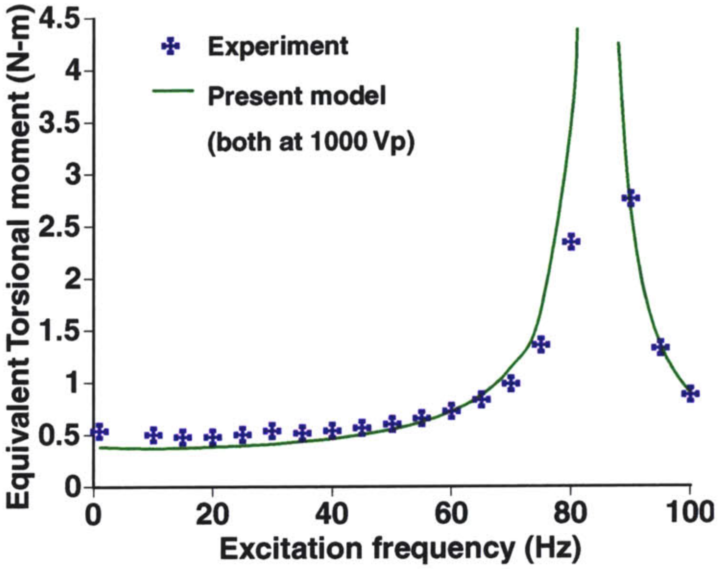

Figure 4-3: Equivalent torsional moment at 49% blade radius of the ATR prototype blade on the bench

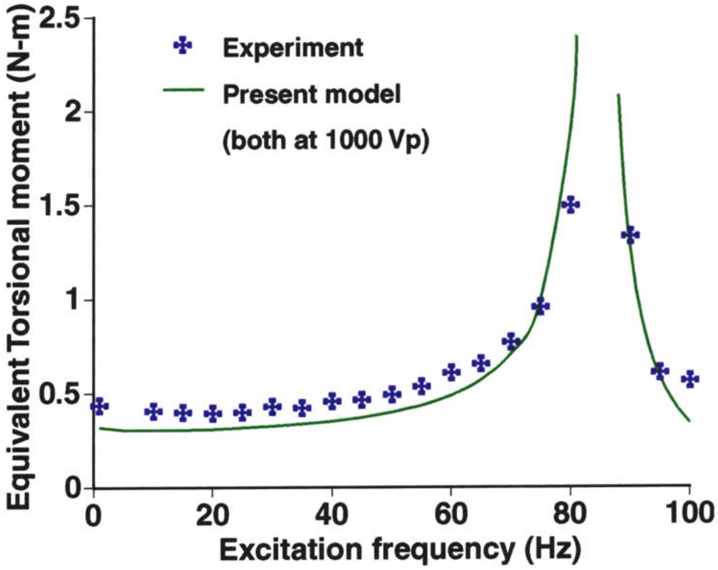

Figure 4-4: Equivalent torsional moment at 75% blade radius of the ATR prototype blade on the bench

quite flat after 1P (11.5 Hz), compensating for the inherent degradation authority of the piezoelectric material with frequency. The analytical model presented herewith captures this effect well, as can be seen from the good correlation with experimental test on the frequency response for both tip twist actuation and torsional deformation of the active blade.

4.4 Hover Frequency Response

4.4.1 Collective pitch sensitivity

From the analytical framework developed in this thesis, the frequency response of the ATR prototype blade can be computed for the hover condition. In Fig. 4-5, equivalent torsional moment at 31% blade radial station is compared with the experimental data for the case of heavy gas environment, full 688 rpm, 2,000 V_{pp} excitation, and varying collective pitch settings 0°, 4°, 8°. As one can see from both magnitude and phase of the torsion gauge readings, the actuation authority is insensitive to the blade static loading (represented by the different collective settings). The different blade loading results in corresponding flapping moments which in turn changes the inplane stresses along the blade span. The piezoelectric effects of PZT materials are dependent on these stresses, and the material tends to depole when subject to tensile stresses. The AFC actuators used in the prototype blade are subject to pre-compression during their manufacturing, increasing their robustness to tensile operational loads [34]. Therefore, no significant effect of inplane loads was identified due to change in collective setting. The first torsion resonance frequency appears at the vicinity of 70 Hz (6.3 P), which is lower than the bench result (85 Hz). It is considered to be associated with the pitch link flexibility, the aerodynamic damping effects, and the effective change on the total length of the blade (due to its mounting on the hub). The analytical model correlates well with the experimental observations. It overpredicts, however, the magnitude of the blade deformation of approximately 0.17 N-m constant offset from very low frequencies up to 5P, with the relative error

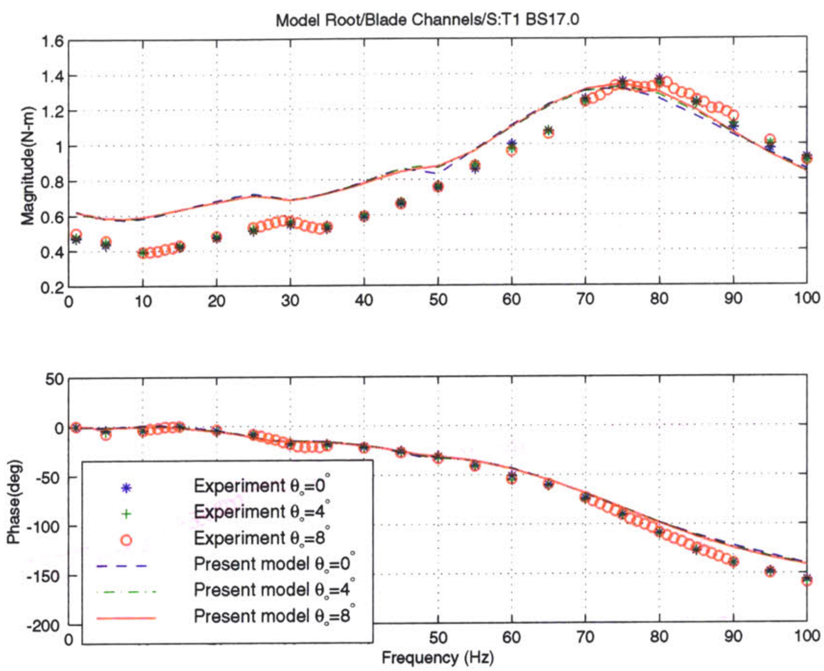

Figure 4-5: Equivalent torsional moment at 31% blade radius of the ATR prototype blade in hover (688 rpm, heavy gas, medium density = 2.432 kg/m^3, 2,000 V_{pp} actuation, θ_o = 0°, 4°, 8°).

varying from 40% to 25%, respectively. This constant offset may indicate the effects of the local three-dimensional deformation field induced by the presence of collocated actuators on the strain gauge bridge, and its effects on strain gauge calibration not taken into account in these results. The phase component of the predicted equivalent torsional moment correlates very well with the experimental results, with errors less than 8% when approaching 10P, which is associated with initial saturation of the power amplifiers during tests.

4.4.2 Medium density sensitivity

When changing the testing medium density, the resulting frequency response functions are shown in Figs. 4-6 and 4-7 for equivalent torsional moment obtained at 31% and 51% spanwise locations, respectively. As one can see, the medium density variation does not influence the actuation authority, except at the torsional resonance frequency due to the change in the aerodynamic damping with density. It is also

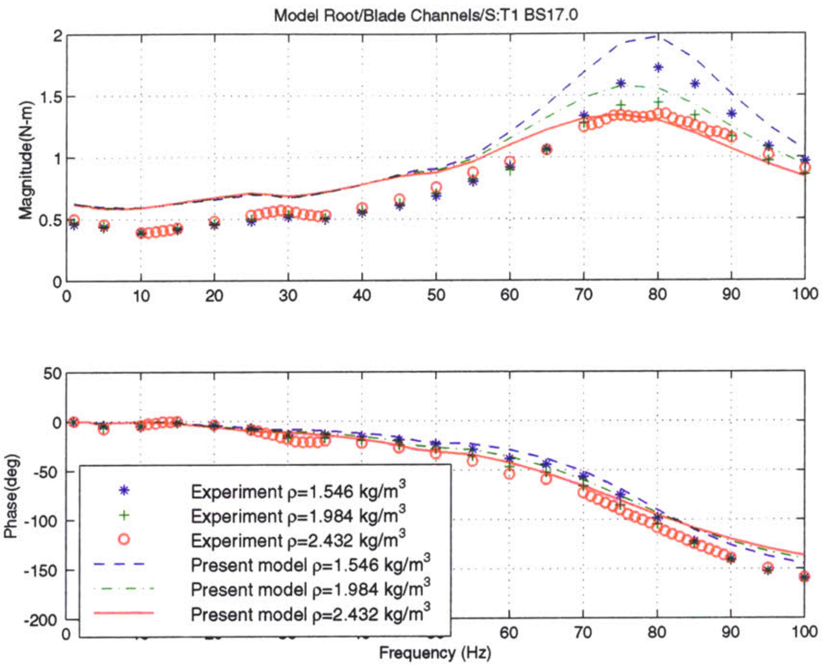

Figure 4-6: Equivalent torsional moment at 31% blade radius of the ATR prototype blade in hover (688 rpm, 2,000 V_{pp} actuation, $\theta_o = 8^o$, medium density = 1.546 kg/m^3, 1.984 kg/m^3, 2.432 kg/m^3).

found that the analytical results follow well the experimental trends so that the peak magnitude around the torsional resonant frequency increases as the test medium density decreases. However, quantitatively the model still overpredicts the experimental data.

4.4.3 Rotational speed sensitivity

Frequency response sensitivity with respect to rotor rotational speed is shown in Figs. 4-8 and 4-9 for 688 (100%) and 619 (90%) rpm. Again, the actuation is quite insensitive to perturbation from the centrifugal loads away from the torsion resonant peak, indicating that the changes in inplane stresses due to rotational speed are not affecting the actuator performance. Around the resonance point, however, the variation of the aerodynamic damping is responsible for the changing in magnitude of torsional moment. The analytical model predicts those trends very well, and again overpredicts the magnitude of the equivalent torsional moment.

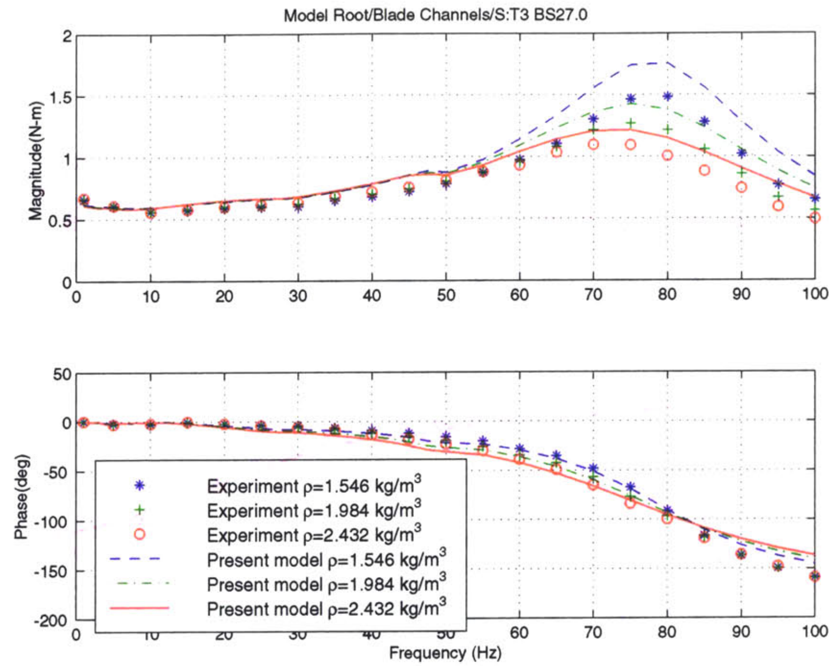

Figure 4-7: Equivalent torsional moment at 51% blade radius of the ATR prototype blade in hover (688 rpm, 2,000 V_{pp} actuation, $\theta_o = 8^o$, medium density = 1.546 kg/m^3, 1.984 kg/m^3, 2.432 kg/m^3).

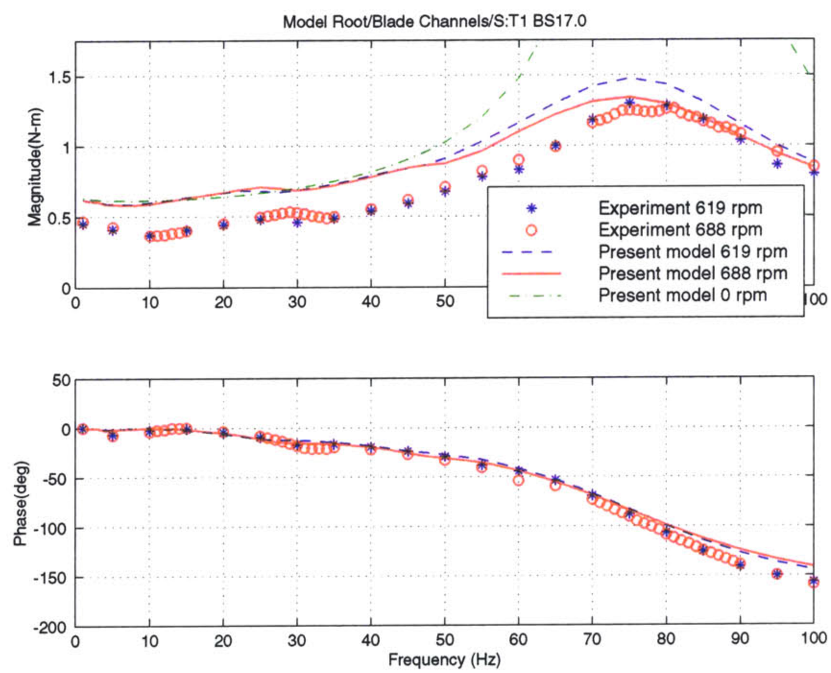

Figure 4-8: Equivalent torsional moment at 31% blade radius of the ATR prototype blade in hover (2,000 V_{pp} actuation, $\theta_o = 8^o$, medium density = 2.432 kg/m^3).

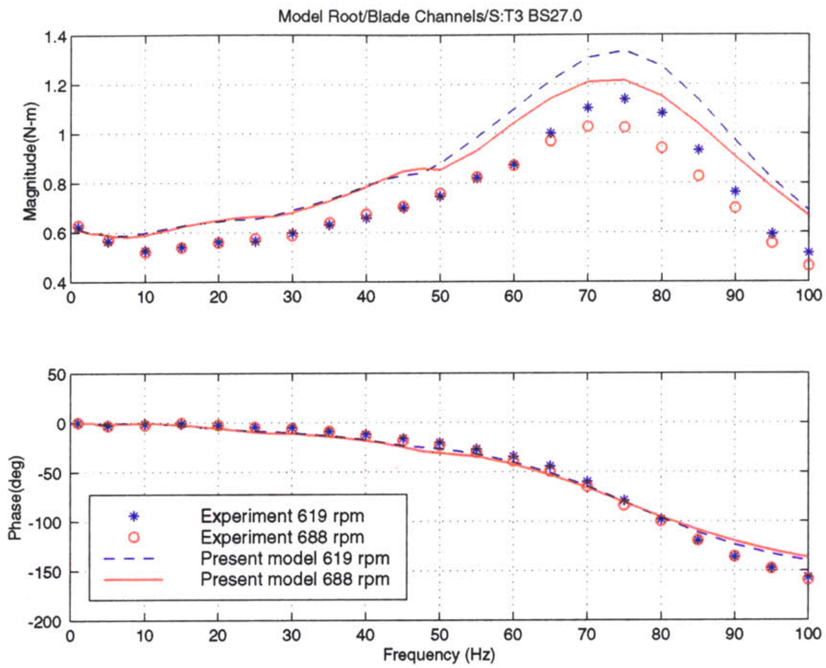

Figure 4-9: Equivalent torsional moment at 51% blade radius of the ATR prototype blade in hover (2,000 V_{pp} actuation, $\theta_o = 8^o$, medium density = 2.432 kg/m^3).

4.4.4 Discussion

Overall, the analysis correctly captures the trend observed in experiments. The degradation of the actuation performance with frequency is well captured and can be observed at low frequency range (below 10 Hz) on all the hover results. The structural resonance, even though occurring at higher frequency, has a broad bandwidth that influences the low frequency range, bringing the twist actuation up. The phase correlation is excellent, both qualitatively and quantitatively. The magnitude of the vibratory torsional moment has been consistently overpredicted, with a constant offset in the 1P to 5P range. As discussed above, this indicates a local three-dimensional effect on the strain gauges caused by the active piezoelectric element. This error should have been accounted for during calibration of the strain gauge bridges but was not for the presented experimental data. The lack of structural damping is the primary source responsible for discrepancies around the peaks as already concluded from the bench results. Another source of damping present in the experiment but not taken into account in the present model is a lead-lag damper. This was used in

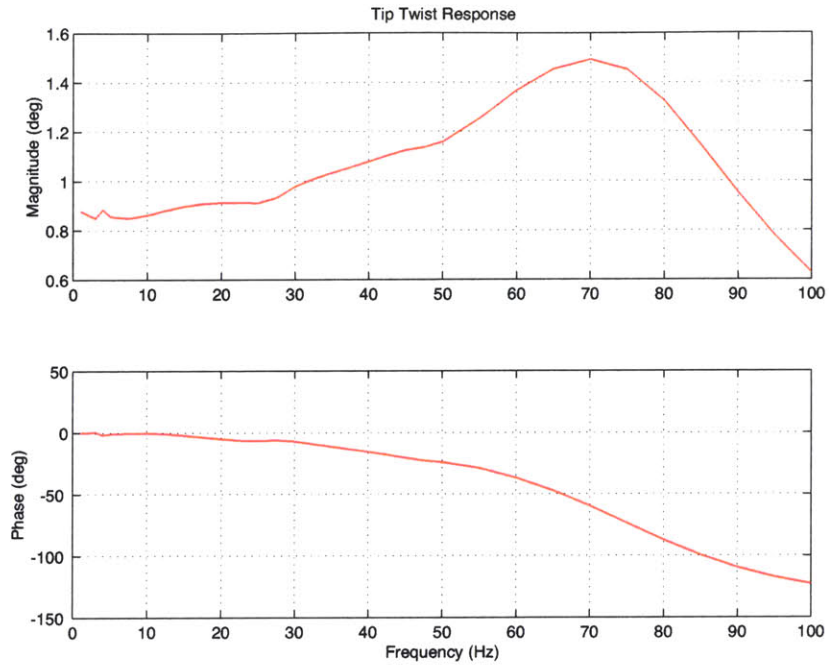

Figure 4-10: Blade tip twist amplitude predicted by the proposed analytical framework (2,000 V_{pp} actuation, 680 rpm, $\theta_o = 8^o$, medium density = 2.432 kg/m^3)

the experimental setup to avoid ground and air resonance of the rotor system. The coupled pitch-flap-lag motion may bring some of those effects to influence the results above. Forward flight part of the proposed analytical framework has a capabilty of modeling lead-lag damper, therefore better correlation is expected with regard to this matter.

Since no specific sensor for tip twist measurements were included in the prototype blade, the blade tip twist can only be estimated based on the analytical framework. Fig. 4-10 presents such results. As it can be seen, between 3P and 5P, the blade tip twist amplitude varies between 1.0° and 1.3°, which, according to previous CAMRAD II simulations [40], should be enough to provide 60% to 80% reduction on 4P hub shear vibratory loads. Forward flight test and analysis in Chapter 5 will be addressing this issue in detail.

Chapter 5

Dynamic Characteristics of the ATR System in Forward Flight

5.1 Overview

The forward flight regime is of great interest for the vibration reduction problem. The blade twist control is suggested to alter the undesirable unsteady aerodynamic environment which develops in that flight regime. As mentioned previously, wind-tunnel testing is conducted on the active rotor system with the ATR test blades. At the same time, confidence on the established analysis model for forward flight is to be obtained through its correlation with experimental data.

Initially, the bench top static actuation testing is revisited in this chapter. This is to exemplify basic validation of the active time domain analysis. Then, the potential impact upon the fixed- and rotating-system loads by the integral blade actuation during forward flight is examined. Both experimental and analytical efforts focus on an open-loop control and their correlation. By accomplishing this, the present forward flight model can be taken for further analytical tasks related with system identification and closed-loop controller design, which will be introduced in Chapters 6 and 7.

5.2 Non-Rotating Frequency Response

In order to verify the modifications introduced to the forward flight analysis, which was introduced in Section 2.3.2, the bench actuation testing results of the ATR prototype blade are used here. A sine-sweep high-voltage signal, which varies its actuation frequency linearly from 1 Hz to 100 Hz within the interval of 1 s, is generated for this purpose. Then, it is applied to the embedded AFC actuators in the prototype blade which is cantilevered at bench, and the blade response and internal loads during the same period are simulated. A time history of the tip twist angle in this simulation is shown in Fig. 5-1. During the actuation period, a resonant response appeared and then undesirable beating phenomenon showed up. In order to eliminate the beating phenomenon to a certain degree, an appropriate level of structural damping is needed in the beam model in the analysis. The non-rotating dynamic characteristics of the blade can be obtained in frequency domain by applying the FFT technique to the time history response. Figs. 5-2 – 5-3 show the experimental measurements of the tip twist rotation and the blade strain gauge readings, respectively. In the same figures, predictions from both models, which are frequency and time domain models originally developed for hover and forward flight analysis, respectively, are also shown as function of the actuation frequency. The two analytical models developed in this thesis capture the overall behavior quite well, as can be seen from the good correlation with experimental data on the frequency response for both tip twist actuation and torsional deformation of the active blade.

The first torsional mode is experimentally identified at approximately 85 Hz, and both models capture it very well. The frequency domain analysis neither includes structural nor stationary aerodynamic damping, resulting in infinite peaks at resonance. This is already observed in Section 4.3, indicating that some structural damping should be added to the numerical analysis. On the other hand, for the time domain analysis, structural damping of magnitude 10^{-4} is found to be appropriate to capture the finite peak at resonance. The coefficient of structural damping used here

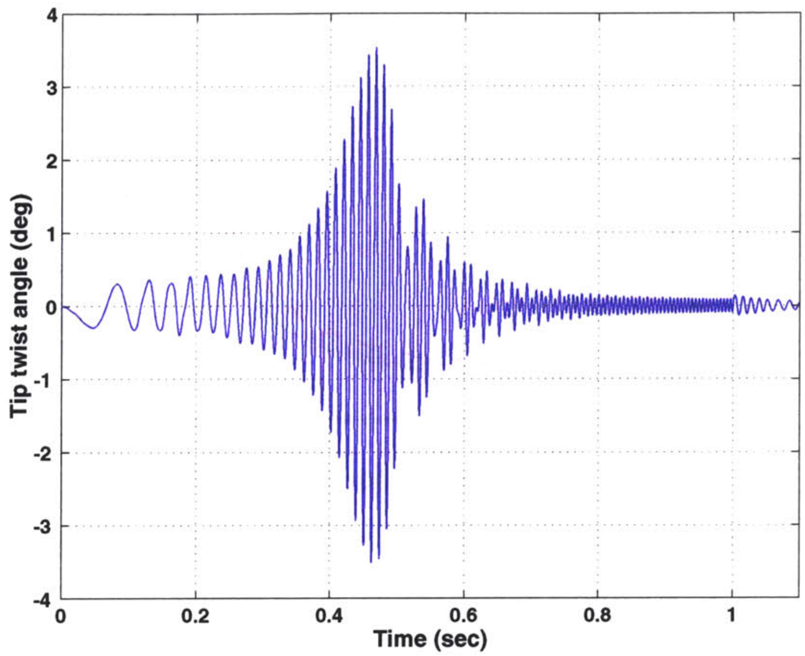

Figure 5-1: Time history of tip twist angle of the ATR blade at bench by sine-sweep actuation signal

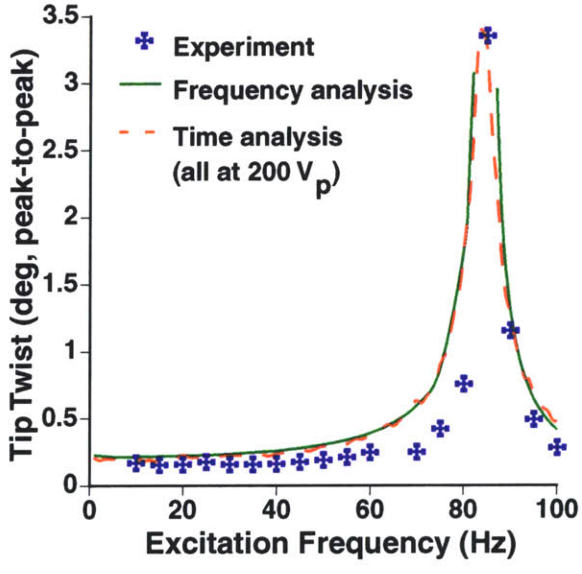

Figure 5-2: Tip twist response of the ATR blade at bench

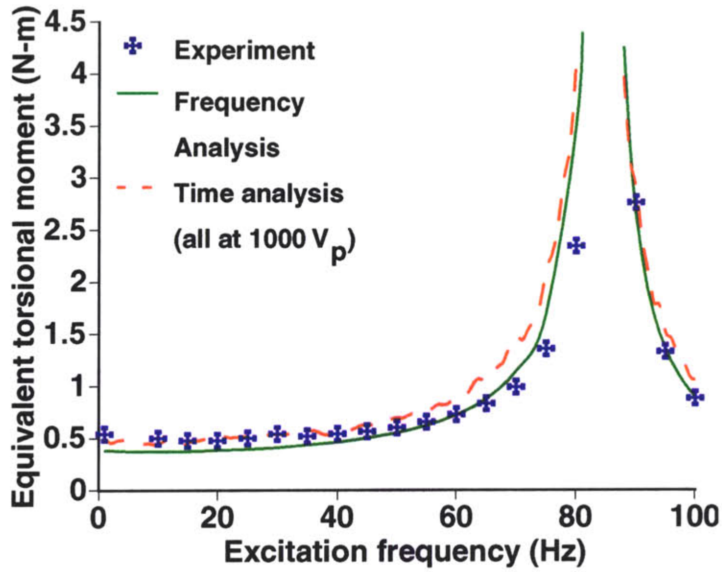

Figure 5-3: Equivalent torsional moment at 49% blade radius of the ATR blade at bench

is defined as follows:

$$\left\{ \begin{array}{c} F_{dB} \\ M_{dB} \end{array} \right\} = \mu_s K_B \left\{ \begin{array}{c} \dot{\gamma}_B \\ \dot{\kappa}_B \end{array} \right\} \tag{5.1}$$

where F_{dB} and M_{dB} are the column vectors of the viscous forces and moments to represent damping in the beam, and μ_s is the damping coefficient. The addition of structural damping brings the location of the peak at a frequency which is slightly lower than that without damping, and proves that the magnitude provided is enough to give the correct response amplitude.

5.3 Forward Flight Response

5.3.1 Analysis Model without Pitch Link

Fig. 5-4 shows the model of the four-active-bladed ATR system used in the forward flight time domain analysis. The hub is modeled as a rigid body, and connected with a revolute joint underneath. It is under a prescribed rotation with nominal rotating speed Ω. Root retention is a passive elastic beam rigidly attached to the hub, and the reaction loads at the attachment point are extracted and added over four of them

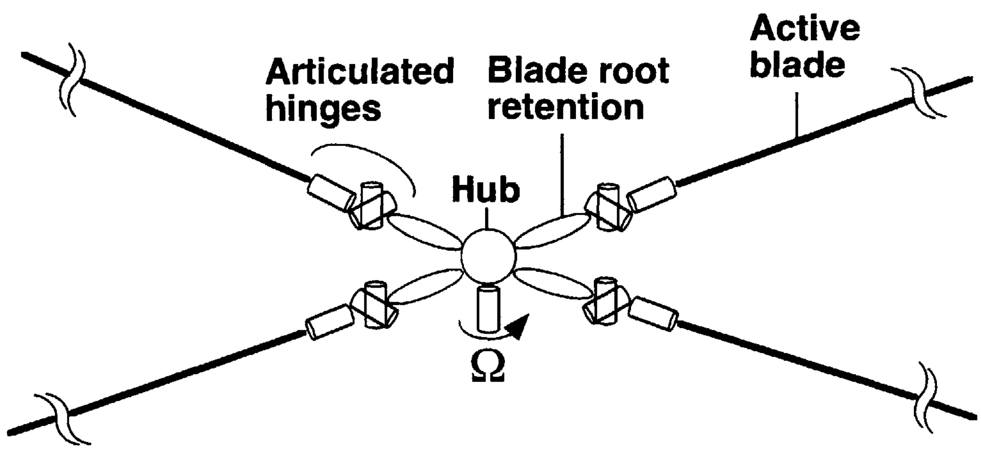

Figure 5-4: Detailed multi-body representation of 4-active-bladed ATR system

to give the hub vibratory loads. Since the ATR system is fully-articulated, three revolute joints are consecutively located between the root retention and the active blade to represent flap, lead-lag, and feathering hinges. As shown in Fig. 5-4, the flapping and lead-lag hinges are coincident. Among the three joints, a prescribed collective and cyclic pitch control commands are applied at the feathering hinge, and their numerical values are based on those used in the wind-tunnel experiment. These are summarized in Table 5.1. Finally, active beams are attached to represent the ATR blades, and they are discretized during the analysis with at least four beam elements per blade, each with the 3rd-order interpolation polynomials. Therefore, there are approximately 900 degrees of freedom to be solved at each time step, including the

Table 5.1: Trim control inputs for the forward flight test conditions

Advance ratio	Rotor shaft inclination angle (deg)	Collective Pitch (deg)	Longitudinal cyclic pitch (deg)	Lateral cyclic pitch (deg)
0.14	-1.0	7.5	-3.5	-3.1
0.17	-1.0	7.0	-3.6	-3.0
0.20	-1.0	7.1	-3.9	-3.1
0.233	-2.0	7.5	-4.3	-3.3
0.267	-2.0	7.8	-4.8	-3.4
0.30	-4.0	8.0	-5.0	-3.3
0.333	-6.0	10.7	-6.2	-4.2
0.367	-6.0	11.2	-6.7	-4.4

dynamic inflow state variables for aerodynamics.

5.3.2 Individual Blade Control Signal

As introduced in Section 3.4.4, three modes of blade actuation were considered in the forward flight open-loop control experiment. Among these modes, the collective and differential modes were experimentally found to be less effective in altering the fixed-system vibratory loads than the IBC mode [49]. It was also observed that simulated 1g level flight conditions generated larger fixed-system vibratory loads than did the descending flight conditions. Therefore, the experimental results presented in this thesis will be limited to those obtained during the simulated 1g level flight conditions while in the baseline (no actuation) and IBC mode of actuation. In order to efficiently impose an IBC-mode sine-dwell signal with control phase variation, a series of high-voltage input is generated using the following formula

$$V(t) = V_{\text{amplitude}} \times \cos\{2\pi\omega_{\text{actuation}}(t - \phi_{\text{control phase}}) + 2N_{\text{act}}\pi \cdot \phi_{\text{blade i}}\} \tag{5.2}$$

where,

$$\begin{aligned}
&V_{\text{amplitude}} = 500,\ 750,\ \text{or}\ 1,000\ \text{V}, \\
&\omega_{\text{actuation}} = N_{\text{act}} \times f_{\text{rotation}}, \\
&\phi_{\text{control phase}} = 0,\ 0.83,\ ...,\ 1.0\ \ (12\ \text{divisions over}\ 360^\circ), \\
&N_{\text{act}} = 3,\ 4,\ \text{or}\ 5, \\
&\phi_{\text{blade i}} = 0.\ (\text{Blade No. 1}),\ 0.25\ (\text{Blade No. 2}), \\
&\qquad\qquad 0.5\ (\text{Blade No. 3}),\ 0.75\ (\text{Blade No. 4})
\end{aligned}$$

An example of the high-voltage input signal generated for an IBC-mode 3P actuation with 12 divisions of control phase angle is displayed in Fig. 5-5. No actuation is applied for the initial 3 seconds to establish a steady-state equilibrium for the given flight condition. At the same time, the baseline (no actuation) quantities are extracted during the last period of this interval, say between 2.5 and 3.0 s, to be compared with

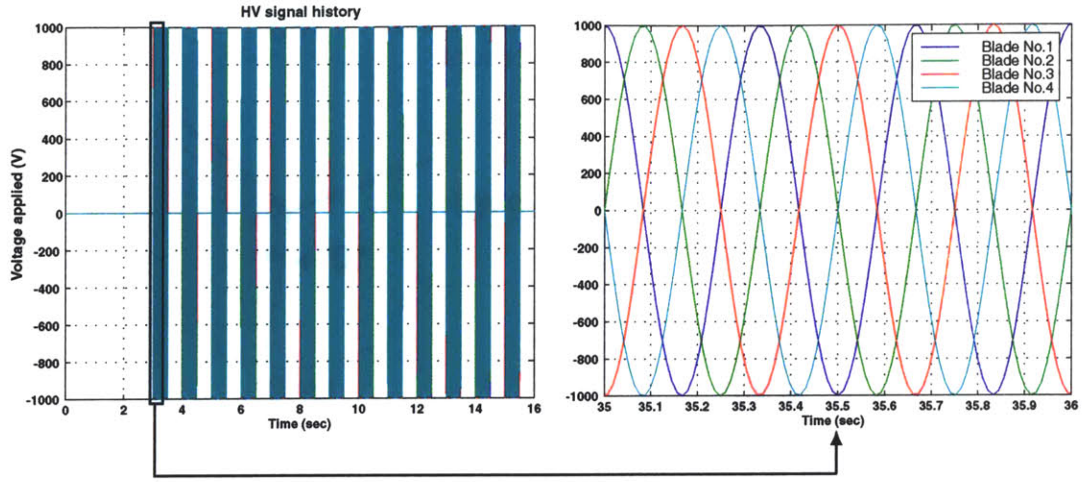

Figure 5-5: Example of high-voltage input generated for an IBC-mode 3P actuation with 12 divisions of control phase angle

those under actuation. Then, for each 0.5-s period of actuation, each with different control phase angle, and another 0.5-s period of no actuation is applied between them. These are applied one after the other as shown in Fig. 5-5.

In each 0.5-second period of actuation cycle, there exists a sine-dwell signal corresponding to a frequency 3P with different phase angles for each blade. 3P sine-dwell signals generated in this fashion are clearly seen in the magnified plot at the right side in Fig. 5-5. By applying this control phase algorithm, the blades exhibit the maximum amplitudes of the sinusoidal electric field at certain azimuthal locations as exemplified in Fig. 5-6. The maximum amplitude occurrence during the first and second actuation periods shows an azimuthal difference of 10° corresponding to 120°/12 divisions, although it is designated as a phase difference of 30° corresponding to 360°/12 divisions in terms of control phase.

5.3.3 Results of the Model without Pitch Link

As a result of the simulation, a time history of the quantities of interest, for example, the forces and moments exerted at each blade and root retention, blade tip displacements, flapping and lead-lag motions at the articulated hinges, and aerodynamic forces generated at the blades are recorded. Among the flight conditions tested

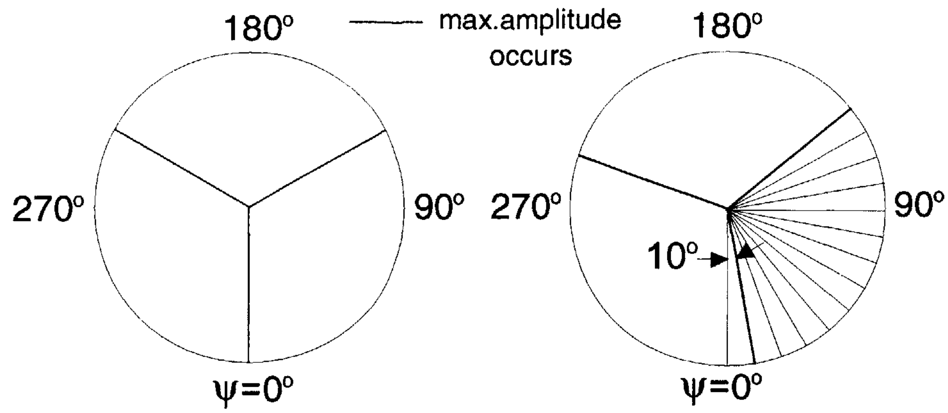

Figure 5-6: Azimuthal locations where the maximum amplitude occurs for the first two actuation periods during the 3P actuation input generated in Fig. 5-5

in the experiment, as summarized in Table 3.6, two conditions are selected here to present the analytical results and their correlation with the experimental observations. First, a flight condition is selected with $\mu = 0.140$, $\alpha_S = -1°$, $C_T = 0.0066$ where C_T is the non-dimensionalized rotor thrust coefficient, and this represents low-speed level flight. Second, a high-speed level flight condition is selected that $\mu = 0.333$, $\alpha_S = -6°$, $C_T = 0.0066$.

Fixed-system loads in the low-speed level flight case

The hub reaction loads of the rotor system can be obtained from summation of all the loads in the four root retention elements at root location. Fig. 5-7 shows the simulated vertical component of the hub shear forces developed in the ATR system when 3P sine-dwell actuation is applied as described in Fig. 5-5. The steady-state trim condition is $\mu = 0.140$, $\alpha_S = -1°$, $C_T = 0.0066$. As one can observe from Fig. 5-7, there is a considerable change in the magnitude of the vibratory loads for certain control phase actuation. The highest reduction happens in the interval of 9 to 9.5 s and 10 to 10.5 s. Notice, however, that there has been an increase in the average thrust of about 2% at the minimum vibration condition.

These time domain quantities can be transferred to frequency domain to examine the magnitude of the frequency content of interest, which is 4P in the four-bladed rotor system. Results are shown in Fig. 5-8 with the corresponding experimental data

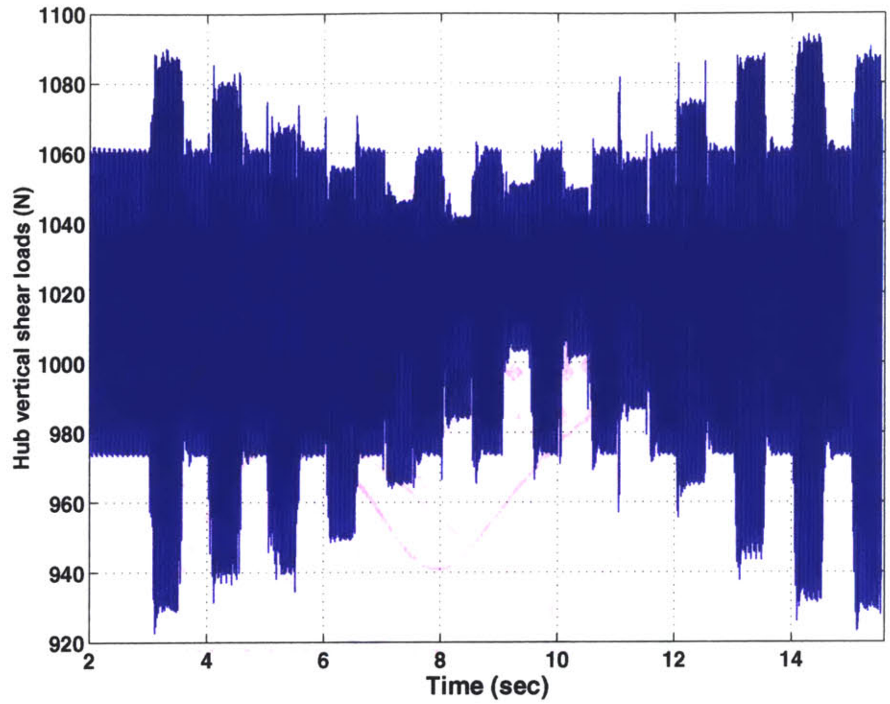

Figure 5-7: Simulated time history of hub vertical shear forces when the 3P actuation is applied as described in Fig. 5-5

for 3P, 4P, 5P actuation applied during the same steady-state trim condition. In the figures, the lines are simple interpolation of the solution points which are obtained from the analysis at discretely increased control phase, while the experimental data are still displayed with the discrete symbols.

The variation of the 4P hub vibratory load components are calculated with respect to the variation of the control phase angles in the vertical, forward, and sideward directions, respectively. The hub sideward component is not included in Fig. 5-8 since its magnitude is too high compared to the other force components, indicating a problem with the measuring device.

The load predicted from the analysis shows significant discrepancy in amplitude from the experimental results, although their variation trends in terms of control phase are in good agreement. As one can see from Fig. 5-8, 3P frequency sine-dwell actuation appears to be the most effective in reducing the hub shear vibratory loads in both cases of vertical and forward components. More specifically, 3P actuation is most effective in hub vertical shear load reduction, resulting in 95% reduction at

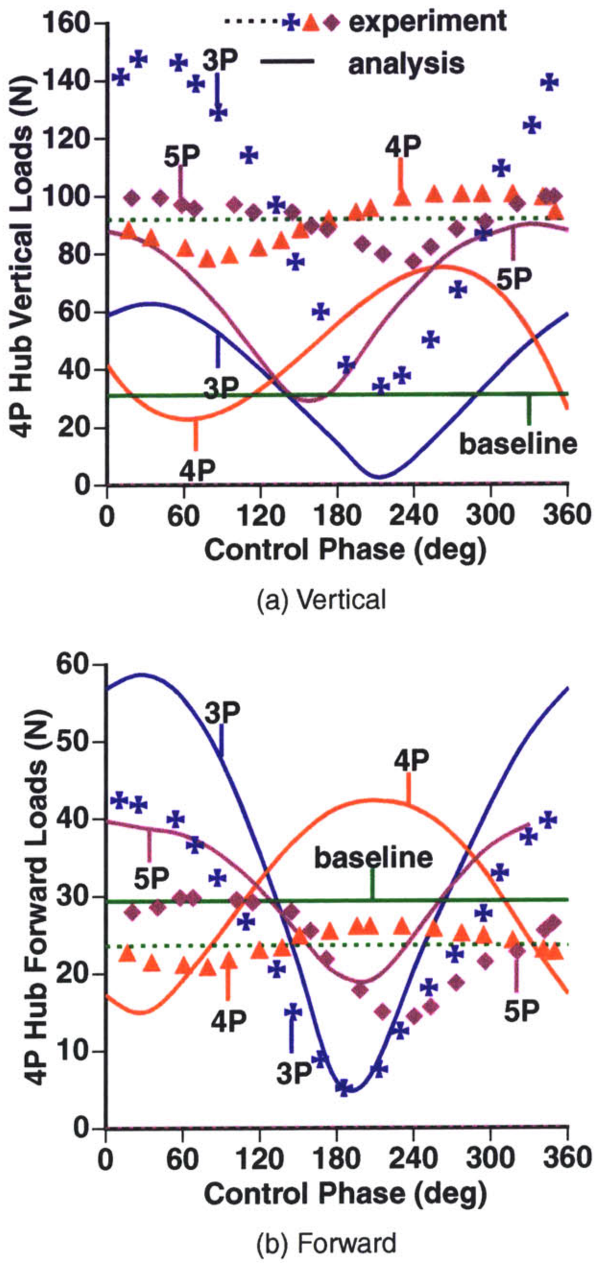

Figure 5-8: Variation of 4P hub shear vibratory loads for $\mu = 0.140$, $\alpha_S = -1^o$, $C_T = 0.0066$, and 1,000 V twist actuation at 3P, 4P, 5P with respect to control phase

210° control phase. It also reduces the hub forward shear loads by 80% at about 180° control phase. Such a hub shear vibratory load reduction performance numerically predicted here shows similar trend as it was observed in the experiment. Further discussion on the comparison between the current analytical results and the experimental data will be given at the end of this chapter. Since the dynamics of the test apparatus (ARES) used for the wind-tunnel test is not included in the model, this may be responsible for the discrepancies. Upgraded input model for the same ATR system including the pitch link and all the linkage components in the swashplate is attempted for better correlation, and will be described in a later section. Also, experimental characterization of the ARES testbed used in the wind-tunnel test is expected to be conducted in the future for the precise modeling of these extra components.

Rotating-system loads in the low-speed level flight case

Quantities in the rotating frame, for example, the flap and chordwise bending moments, and torsional moments are calculated in the reference blade and can also be correlated with the experimental results. The span location where these quantities are calculated is selected to match those of the strain gauges embedded in the test blade. While the fixed-system quantities, such as hub shear vibratory loads, were investigated only in 4P frequency components, those in the rotating frame are extracted and examined in their 3P, 4P, and 5P frequency components. Figs. 5-9 – 5-10 show blade loads at those frequencies.

Again, the lines are simple interpolation of the solution points from the analysis, and symbols represent the experiments. The 3P frequency components of the flap bending moment at 28.7% span location are extracted and shown in Fig. 5-9 (a). The results are for the condition of $\mu = 0.140$, $\alpha_S = -1°$, $C_T = 0.0066$, and 1,000 V twist actuation at 3P, 4P, 5P with respect to control phase. 4P frequency components for the same flap bending moment are presented in Fig. 5-9 (b), and 5P components are in Fig. 5-9 (c). As well as in the fixed-system quantities, the present model captures the trend of variation in the rotating frame values as they were observed in the experiments. However, discrepancies can be observed in the amplitude by approximately

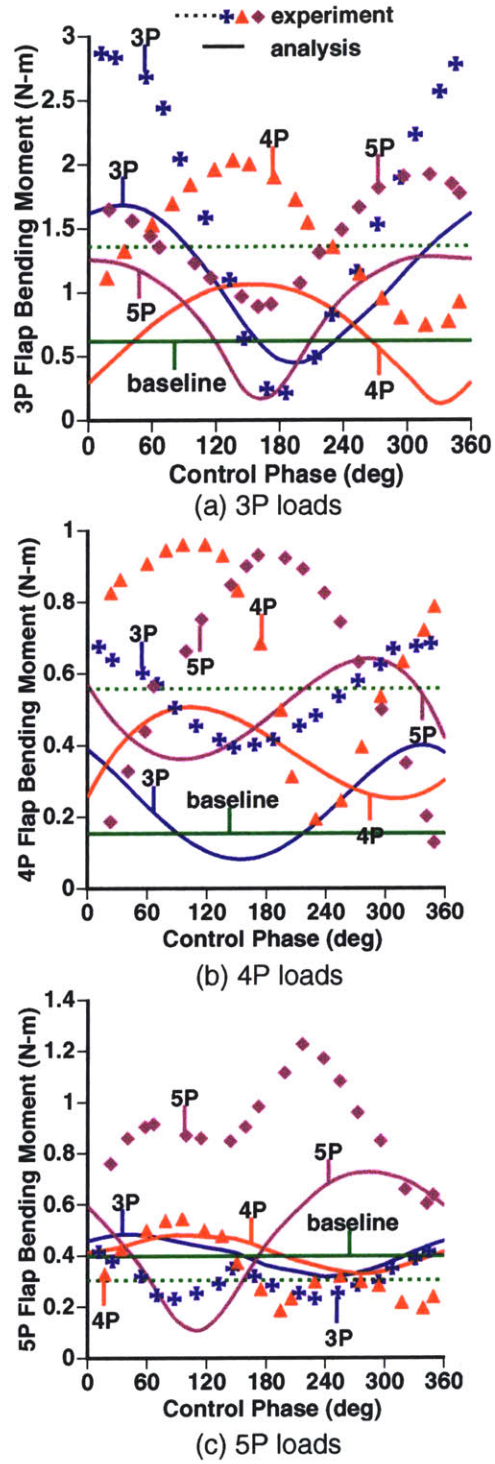

Figure 5-9: Variation of flap bending moment at 28.7% span location for $\mu = 0.140$, $\alpha_S = -1^o$, $C_T = 0.0066$, and 1,000 V twist actuation at 3P, 4P, 5P with respect to control phase

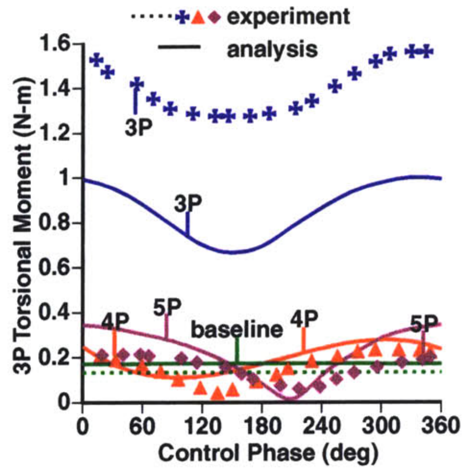

(a) 3P loads

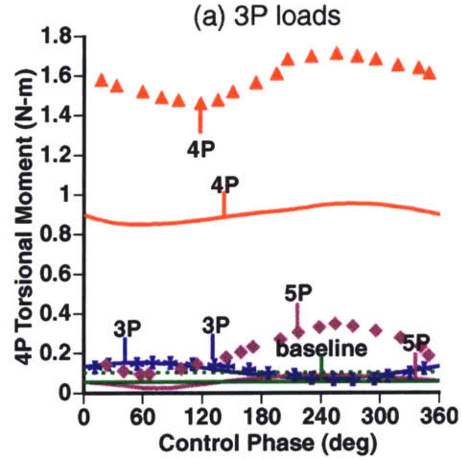

(b) 4P loads

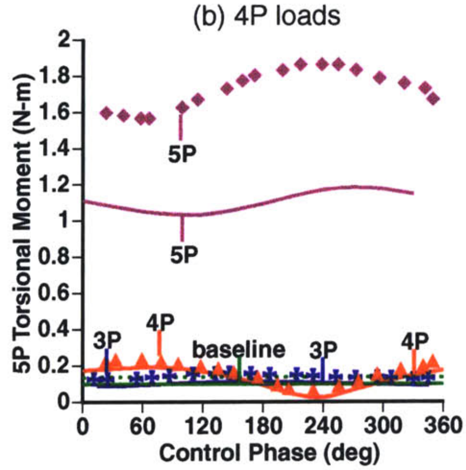

(c) 5P loads

Figure 5-10: Variation of torsional moment at 33.6% span location for $\mu = 0.140$, $\alpha_S = -1^o$, $C_T = 0.0066$, and 1,000 V twist actuation at 3P, 4P, 5P with respect to control phase

$20 - 50\%$ between the numerical results and experimental data. Torsional moment at 33.6% span location are calculated and shown in Fig. 5-10 for the same steady-state condition and amplitude of actuation as before. The 3P, 4P, and 5P components of the torsional moments in each of the cases are significantly increased by the actuation loads in their respective frequencies. This is an aspect of the ATR concept that requires special attentions since it may affect blade integrity and life.

Polar plot of the fixed-system loads in the low-speed level flight case

A simplifying assumption has been used by researchers investigating higher harmonic control technology using conventional swashplate actuation. It is based on the experimental finding that an approximate linear relationship can be extracted between the harmonic control inputs and the resulting fixed- and rotating-system loads [11, 12]. This relationship was well observed from the relevant wind-tunnel experiments when the fixed- and rotating-system loads obtained under the harmonic swashplate actuation were plotted in polar format. A similar polar plot is attempted on the present analysis result obtained to check if a linear relationship may be extracted. In the present section, only three shear force components of the fixed-system loads are displayed in polar format. 4P hub vertical shear loads due to 3P actuation is shown in Fig. 5-11 (a) for $\mu = 0.140$, $\alpha_S = -1°$, $C_T = 0.0066$. It is observed that the 4P vibratory load level at discretely-varying control phase (which is noted beside the individual points) compose an ellipse around a reference point corresponding to no actuation (designated by "Baseline"). Similar ellipse shape can be observed for the other components, such as 4P hub forward shear loads displayed in Fig. 5-11 (b), and sideward loads in Fig. 5-11 (c). These results show essentially the same trend as it was observed in the previously mentioned HHC studies. It leads to the same simplifying assumption that all the points on the ellipse can be obtained from the central point by adding an incremental vector which is almost linearly dependent on the 3P actuation input. This relationship can be described by the following relation

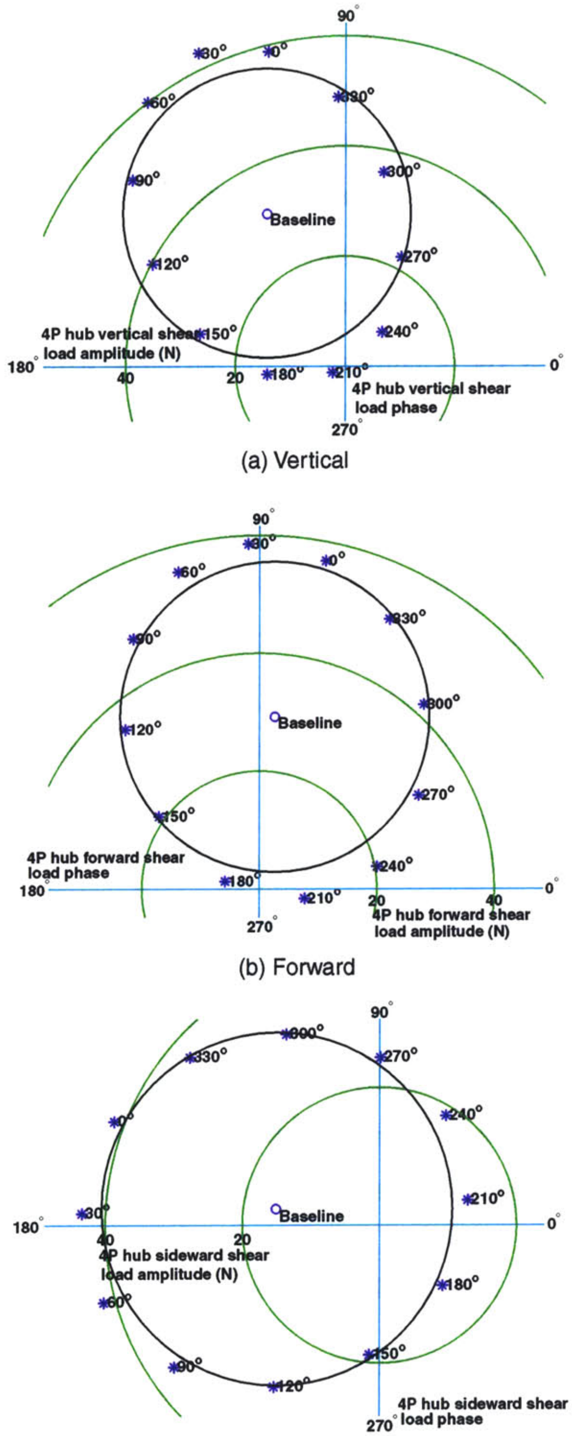

Figure 5-11: Polar plot of 4P hub shear vibratory loads for $\mu = 0.140$, $\alpha_S = -1^{\circ}$, $C_T = 0.0066$, and 1,000 V twist actuation at 3P, compared with the baseline value

$$\left\{ \begin{array}{c} F_{4c} \\ F_{4s} \end{array} \right\} = \left\{ \begin{array}{c} F_{4c} \\ F_{4s} \end{array} \right\}_{\text{Baseline}} + \left[\begin{array}{cc} a_{11} & a_{12} \\ a_{21} & a_{22} \end{array} \right] \left\{ \begin{array}{c} F_{3c}^{(a)} \\ F_{3s}^{(a)} \end{array} \right\} \tag{5.3}$$

where F_{4c} and F_{4s} are the cosine and sine component of 4P hub shear vibratory loads, respectively, with respect to its phase. $F_{3c}^{(a)}$ and $F_{3s}^{(a)}$ are the cosine and sine component of 3P twist actuation inputs, respectively. The shape of the actuation point grouping becomes elliptical since, as the control phase of the harmonic twist actuation input changes, the orientation of the harmonic feathering motion waveform of the blade changes relative to the forward flight velocity. For some control phase (30° in Fig. 5-11 (a)), the harmonic feathering effects add to the local velocity effects to produce the largest incremental load vector. At the opposite control phase (210° in Fig. 5-11 (a)), the interaction is also strong but exactly opposite, producing an almost equally long incremental load vector in the opposite direction. However, for some intermediate control phases and the phase exactly opposite to it (120° and 300° in Fig. 5-11 (a)), the interaction is weakest, producing the shortest incremental vectors.

However, the local wind velocities are constant with azimuth in hover, so the length of the incremental vector is independent of the harmonic input phase; thus the grouping will become circular. Such a linear relationship between input harmonic and output loads leads to the so-called **T** matrix approach [13]. It has been one of the traditional approaches to identify transfer functions, adopted by those who study conventional higher harmonic control. In this thesis, however, the polar plots are just used to support a completely different approach which is introduced in Chapter 6.

Results of the high-speed level flight case

For the high-speed level flight condition selected, a corresponding trim control commands are extracted from Table 5.1, and used to establish the required steady state equilibrium. Then, the same IBC-mode sine-dwell blade actuation signal as used in the previous low-speed flight case is applied. By processing the time domain results in the same way, fixed- and rotating-system loads for the high-speed level flight condi-

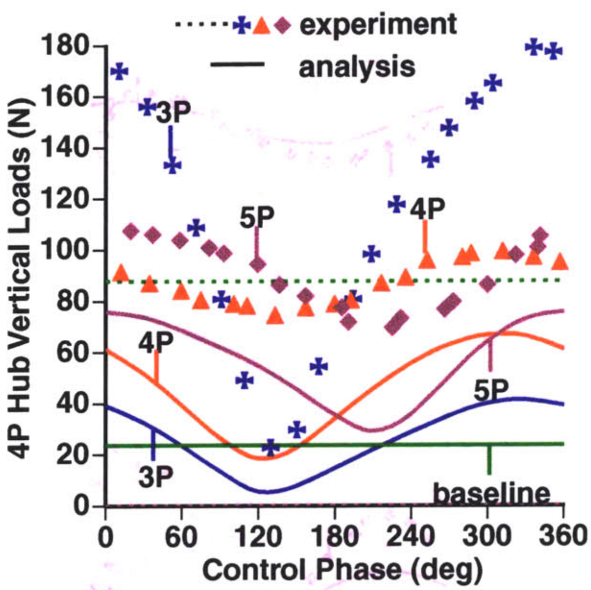

(a) Vertical

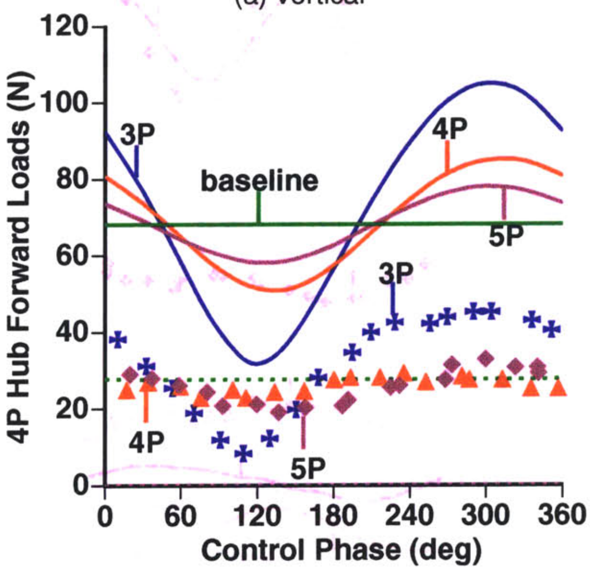

(b) Forward

Figure 5-12: Variation of 4P hub shear vibratory loads for $\mu = 0.333$, $\alpha_S = -6^o$, $C_T = 0.0066$, and 1,000 V twist actuation at 3P, 4P, 5P with respect to control phase

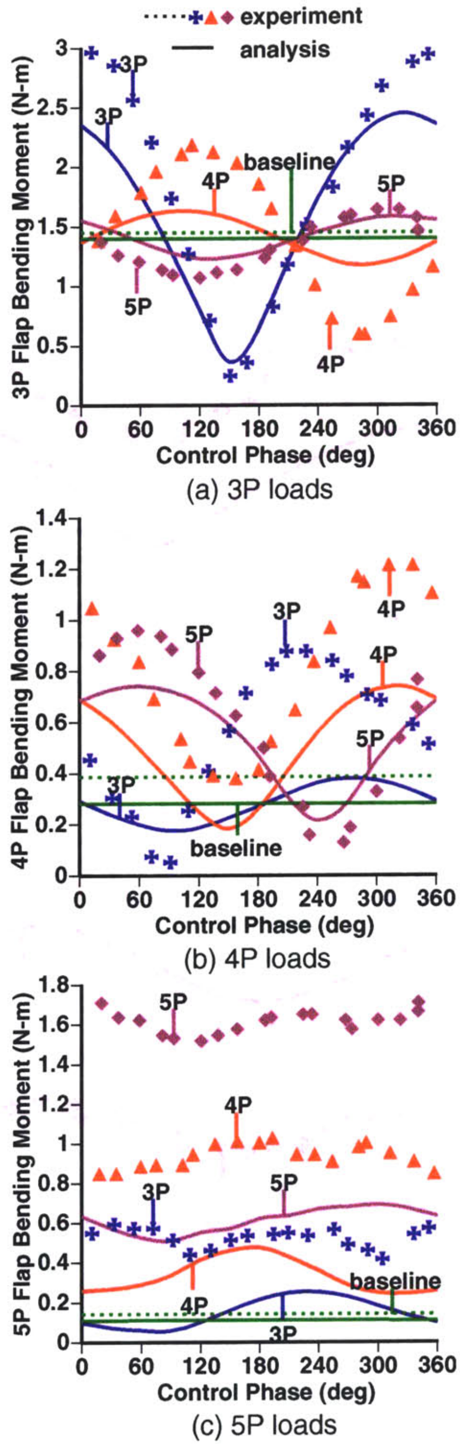

Figure 5-13: Variation of flap bending moment at 28.7% span location for $\mu = 0.333$, $\alpha_S = -6^o$, $C_T = 0.0066$, and 1,000 V twist actuation at 3P, 4P, 5P with respect to control phase

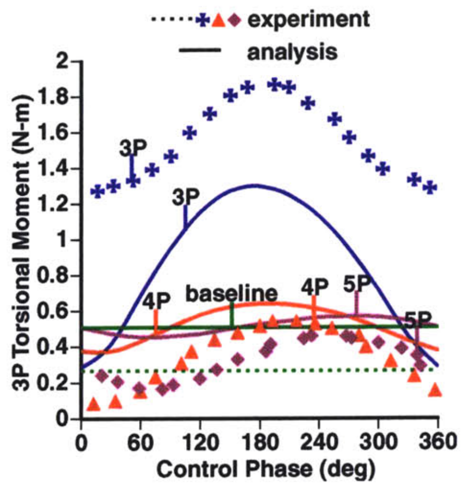

(a) 3P loads

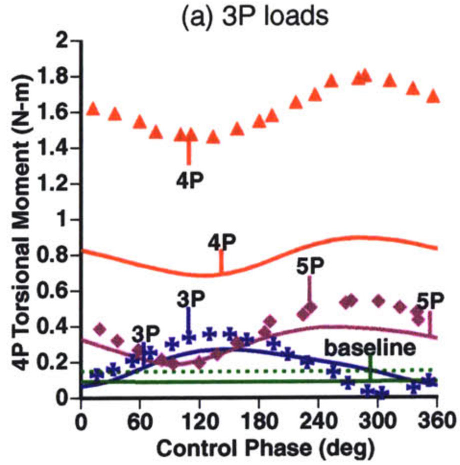

(b) 4P loads

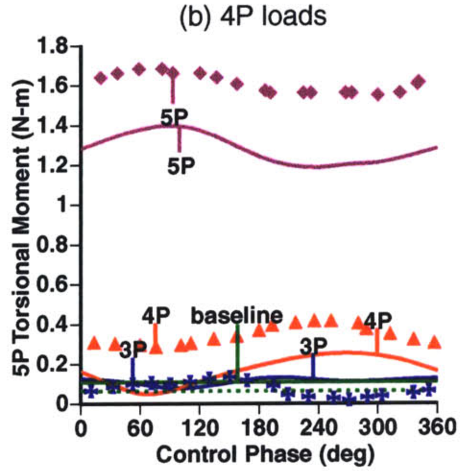

(c) 5P loads

Figure 5-14: Variation of torsional moment at 33.6% span location for $\mu = 0.333$, $\alpha_S = -6^o$, $C_T = 0.0066$, and 1,000 V twist actuation at 3P, 4P, 5P with respect to control phase tion are obtained. Their correlation with the experimental data is shown in Figs. 5-12 – 5-14. Again, the loads predicted from the analysis show significant discrepancy in amplitude from the experimental results, although their variation trends in terms of control phase are in good agreement.

5.3.4 Analysis Model with Pitch Link

As discussed in the previous section, the ATR system modeled without the detailed components such as pitch link and swashplate failed to exhibit precise load prediction regarding the fixed- and rotating-system loads when compared with the experimental results. Therefore, an upgrade of the input model was attempted. Detailed task of the upgrade includes to model a pitch horn as a rigid body and attach it at the feathering hinge. Also, two swashplate components, upper (rotating) and lower (non-rotating) are created as rigid bodies, and attached in the middle of the rotor shaft. These two components are connected with each other with a revolute joint so that they can exhibit the same vertical and tilting movement along the rotor shaft. Then, a pitch link, which is modeled as an elastic beam, is used to connect the pitch horn to the upper swashplate. In order to spin the upper swashplate independently, a scissor mechanism is also generated as a series of links and attached between the upper rotor shaft and the upper swashplate. Pitch control commands are applied at the lower swashplate as a vertical movement for collective pitch angle and two tilting angles for longitudinal and lateral cyclic pitch angles; these movements are transmitted to the upper swashplate. The upgraded input model including the detailed components is depicted in Fig. 5-15, where the pitch link mechanism is displayed only for one blade for convenience.

The geometry data for the updated model is based on the ARES test apparatus measurement used in the forward flight experiment, and summarized in Table 5.2. Most newly included components are modeled as rigid bodies, reflecting the fact that the ARES system is extremely stiff compared with the practical helicopter fuselage and components. However, the pitch link and rotor shaft are modeled as elastic beam, where the pitch link dynamics is specified with a stiffness value that represents the

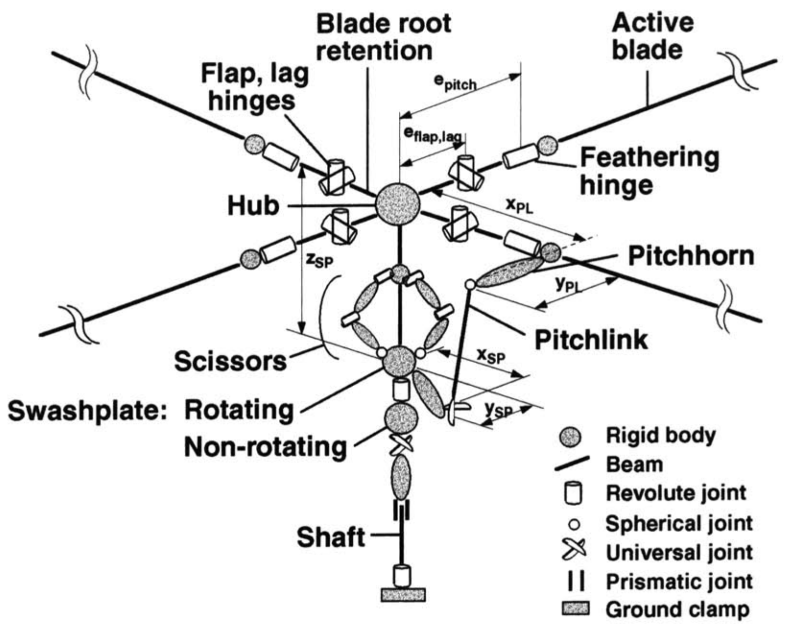

Figure 5-15: Upgraded input model of ATR system including pitch link and swashplate components

flexibility of the whole control system. According to NASA Langley, the rigid feathering mode of the ATR system is observed at frequency between 15P and 16P. Based on the pitch inertia of the ATR test blade and pitch link geometry, an axial stiffness of the pitch link is estimated as also included in Table 5.2. By including the pitch link mechanism in the model, the pitch/flap coupling existing in the ARES apparatus, which amounts to 0.5 in flap up/leading edge down fashion, is automatically implemented. Due to the dynamic interaction among the control linkage, the feathering motion at the blade root in the rotating condition shows discrepancy from those in

Table 5.2: Geometry and material property of the upgraded ATR system model

Parameter	Value
$e_{\text{flap, lag}}$	0.0762 m
e_{pitch}	0.1143 m
x_{PL}	0.03556 m
y_{PL}	0.05715 m
x_{SP}	0.027686 m
y_{SP}	0.04445 m
$EA_{\text{pitch link}}$	$3.822\ 10^3$ N

the static condition estimated to obtain the same pitch control commands. Therefore, an adjusted movement at the swashplate is added to compensate such discrepancy for the dynamic analysis.

5.3.5 Results from the Model with Pitch Link

The same IBC-mode sine-dwell signal generated in the previous section is applied in the upgraded analysis model, and both fixed- and rotating-system loads are recorded during the simulation. By processing the time domain results in the same way as in Section 5.3.3, corresponding frequency domain components are obtained. These are shown in Figs. 5-16 – 5-18 together with the experimental data and the analytical results previously obtained from the one without pitch link. A correlation on the pitch link load is possible for this upgraded model, and shown in Fig. 5-19.

Upgraded input model including the pitch link and all the linkage components in the swashplate is attempted for better correlation. However, this increase in model detail has shown little impact on the load prediction. Most of all, the discrepancies in the baseline load prediction are seldom cured by the model upgrade. Therefore, it is concluded that the sources from which the present discrepancies originate are still not properly included in the analysis. Sources of the discrepancies between analysis and experiment are discussed further in the following section. By observing a slight improvement obtained from the model upgrade, it is determined that the previous analysis model without pitch link will be used for further analysis. Although the previous model is crude in its representation of the swashplate control system, it is capable of exhibiting similar details on the dynamic characteristics of the ATR system with much lower computational effort.

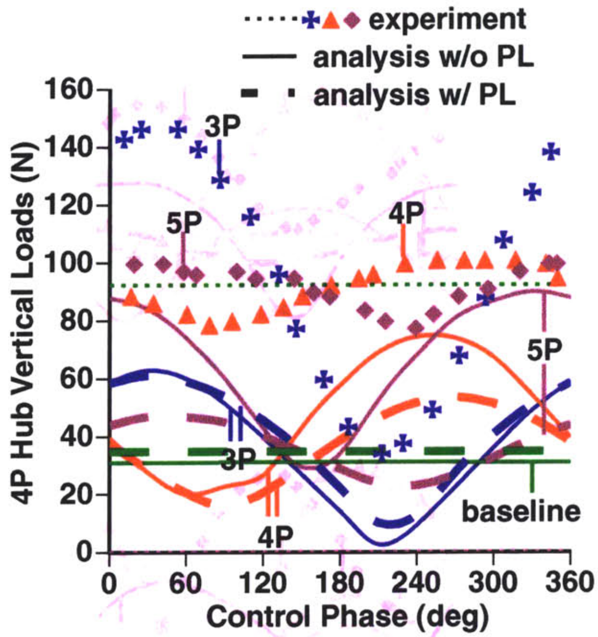

(a) Vertical

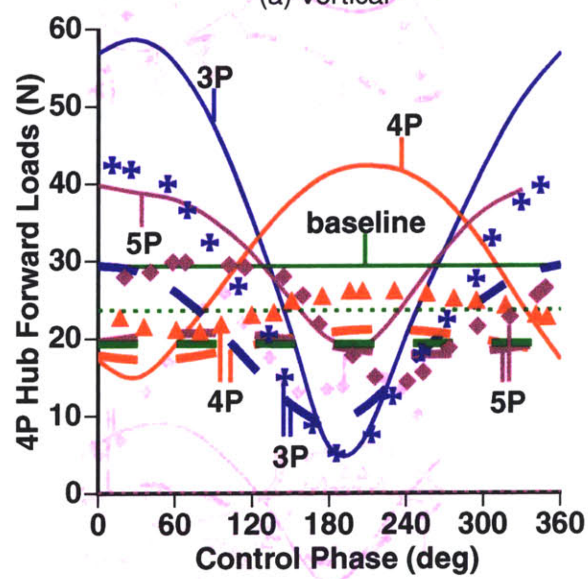

(b) Forward

Figure 5-16: Variation of 4P hub shear vibratory loads for $\mu = 0.140$, $\alpha_S = -1^{\circ}$, $C_T = 0.0066$, and 1,000 V twist actuation at 3P, 4P, 5P with respect to control phase: experiment, analysis without pitch link, and analysis with pitch link

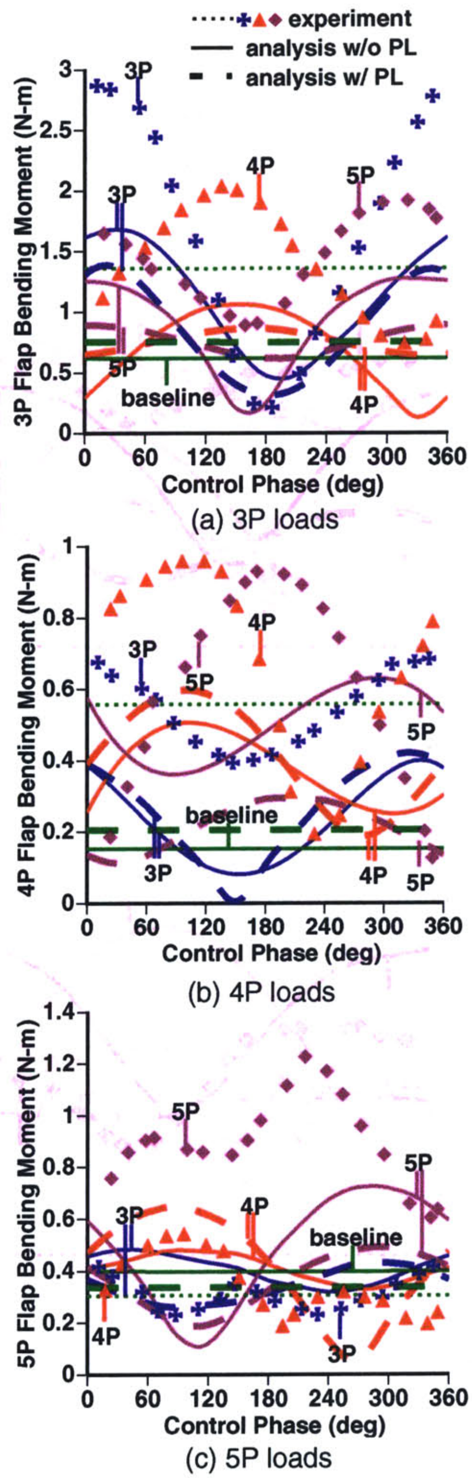

Figure 5-17: Variation of flap bending moment at 28.7% span location for $\mu = 0.140$, $\alpha_S = -1^o$, $C_T = 0.0066$, and 1,000 V twist actuation at 3P, 4P, 5P with respect to control phase: experiment, analysis without pitch link, and analysis with pitch link

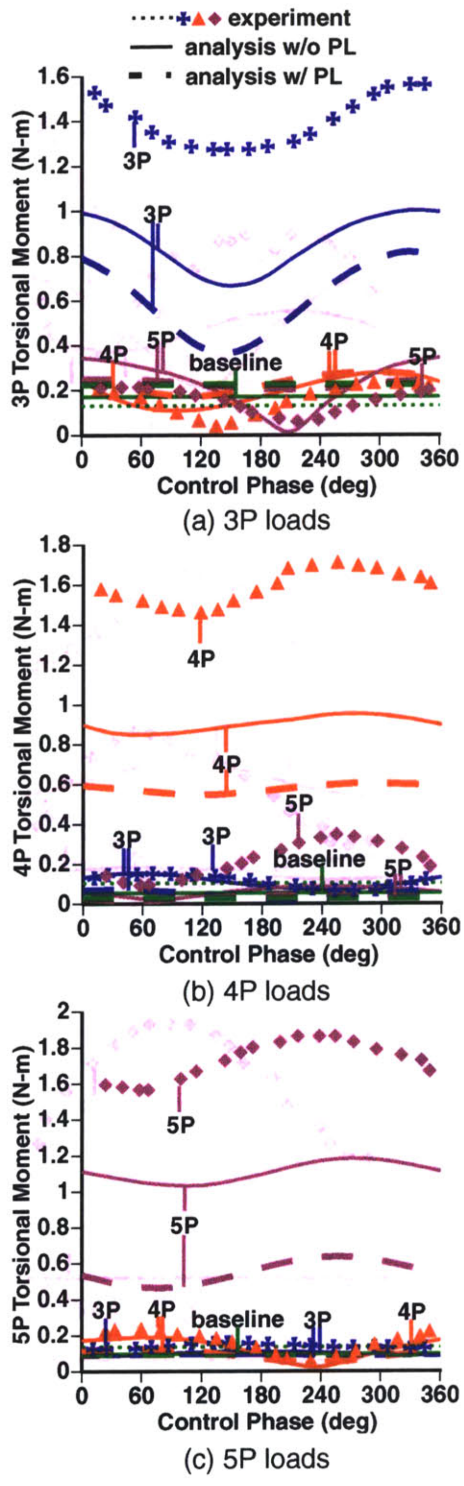

Figure 5-18: Variation of torsional moment at 33.6% span location for $\mu = 0.140$, $\alpha_S = -1^o$, $C_T = 0.0066$, and 1,000 V twist actuation at 3P, 4P, 5P with respect to control phase: experiment, analysis without pitch link, and analysis with pitch link

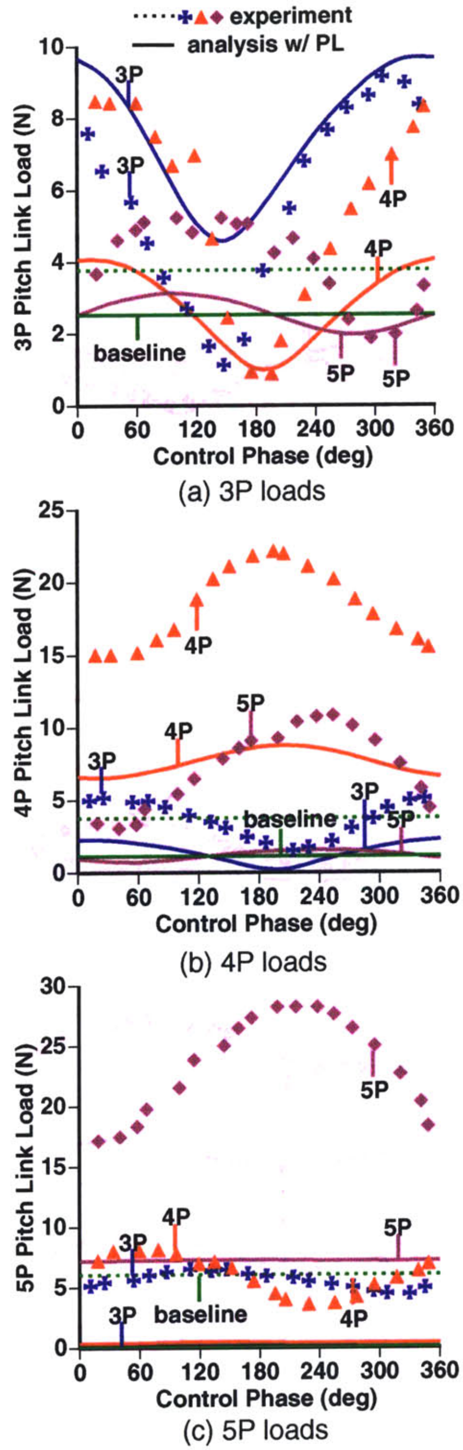

Figure 5-19: Variation of pitch link axial loads for $\mu = 0.140$, $\alpha_S = -1^{\circ}$, $C_T = 0.0066$, and 1,000 V twist actuation at 3P, 4P, 5P with respect to control phase: experiment, and analysis with pitch link

5.4 Correlation of Forward Flight Analyses with Experiments

Both of fixed- and rotating-system loads predicted from the forward flight analysis exhibit significant discrepancy in amplitude from the experimental results, although their variation trend in terms of control phase is in good agreement. It should be further noted that the baseline amplitude in most of the cases are significantly underpredicted by the numerical analysis.

A study to improve the correlation of the baseline load amplitude is performed. For the analysis model without pitch link, blade structural modeling accuracy was studied with respect to the stiffness matrix and chordwise c.g. location, regarded as factors which affect the dynamics of the rotor system. According to the cross-sectional analysis results shown in Table 3.3, the ATR test blade has its chordwise c.g. at 18%, although the blade manufacturers suggested that the blade had required 25% c.g. location. Also, the analysis indicates that the shear center is located at 30% chord instead of the 25% chord that coincides with the blade reference line. This effect can be included in the analysis by simply using the fully-populated stiffness matrix. Therefore, different models of the ATR dynamics were constructed and their prediction of the baseline loads were obtained for the low-speed level flight condition, as shown in Table 5.3. Changes in the load prediction resulted from the variation in the structural modeling. However, these changes fail to significantly improve the correlation with the experiments. Finally, the model with pitch link did exhibit an improvement even with a crude structural modeling for the blade; however, it is again a slight improvement. Therefore, an analysis model with a diagonal stiffness representation, 30% shear center and 25% c.g. locations, has been used for all the analytical results presented in this chapter, and is also used for further analysis in the following chapters.

Also, the experimental 4P hub sideward baseline force (See Table 5.3) presented unreasonably high magnitude when compared to the other two hub force components. This suggests that further characterization of the whole experimental apparatus is

Table 5.3: Fixed-system baseline loads predicted with different blade structural representations and c.g. locations ($\mu = 0.140$, $\alpha_S = -1^o$, $C_T = 0.0066$)

	Stiffness matrix representation	Chordwise c.g. (%)	Baseline loads (N)		
			Vertical	Forward	Sideward
Model without pitch link	diagonal	25	31.1	29.3	15.3
	diagonal	18	14.1	10.6	3.6
	fully-populated	18	19.4	16.1	4.5
Model with pitch link	diagonal	25	34.8	29.3	36.9
Experiment	-	-	92.0	23.6	142.8

desirable. Once this is done and the information brought to the model, an improved correlation between them is expected. In this thesis, the basic active aeroelastic characteristics of the ATR system has been captured by the analysis, and the study will continue based on that.

There exist other factors which may influence the accuracy of both analysis and experiment. In the analysis, the predicting accuracy is influenced by the aerodynamics model used. As described in Section 2.4.2, the one adopted in this thesis was considered accurate enough for the present type of rotor aeroelasticity study. However, it was recently found [61] that more sophisticated wake model, e.g. free wake, might be required to precisely estimate the aerodynamics, especially in the case of higher harmonic control investigation. Also, it is suggested by Peters [56] that the present aerodynamics be reinforced by an appropriate dynamic stall model, which is not included in the present implementation.

In the experiment, noise induced in the instrumentation may be a significant factor on the accuracy of the result. In the present experiment, instrumentation noise was manifested in the rotating-system loads measurement. For example, flap bending strain gauge measurements showed irregular variation in Fig. 5-14 (c). Also, recirculation in the tunnel may contribute to changes in response, even though this is deemed unlikely by the researchers at NASA Langley, based on previous experiments with the ARES testbed.

Chapter 6

System Identification of the ATR System in Forward Flight

6.1 Overview

The forward flight analysis model established in this thesis exhibited sufficient details of a typical helicopter and its rotor blade dynamic behavior, although it showed inaccuracy in amplitude of the predicted loads. Therefore, it is selected to be used in this chapter for system identification of the ATR system in forward flight.

During forward flight, the helicopter rotor blade exhibits an aerodynamic environment which varies itself with a period corresponding to the rotor revolution. This situation is illustrated in Fig. 1-1. This signifies that the helicopter rotor system is basically a linear time-periodic (LTP) system during forward flight. Therefore, a methodology considering this periodicity is required for its characterization. In this thesis, a method is adopted which results in multi-component harmonic transfer functions [62]. The theoretical background of the adopted methodology is briefly summarized in Appendix E with its implementation schemes that include additional assumptions imposed on the transfer functions. The sine-sweep input signals created for computation of such harmonic transfer functions are described in detail in this chapter. The results of the system identification is presented for each different mode of blade actuation. Finally, certain characteristics of the present ATR system are drawn from the system identification results, which may simplify the closed-loop controller design.

6.2 Input Signals for System Identification

A comprehensive and accurate system characterization effort requires input signals to possess appropriate frequency content, and also phase quantities in case of LTP system. As described in Appendix E.2, sinusoids are used to determine transfer functions, and more specifically, sine-sweep waves (chirp signals) are used to obtain the system response over a specific range of frequencies. The chirps may have frequencies that vary either linearly, quadratically, or logarithmically with time. The frequency content and time interval of the chirp is dependent on the system characteristics. It is also important to take the chirp phase into consideration in the case of LTP system.

For a helicopter rotor system with b blades and rotor rotational period T_r, the system period T will be T_r/b. Then, the output frequencies due to an input signal at frequency ω will be shifted by positive and negative multiples of the blade passage frequency ω_p, where

$$\omega_p = 2\pi b/T_r \tag{6.1}$$

Since a linearly varying sine-sweep signal is considered in the present identification, the frequencies of the input signal are a linear function of time, as

$$f = f_0 + \frac{f_1 - f_0}{T_c}t \tag{6.2}$$

where f_0 is the initial signal frequency (Hz), f_1 is the final frequency (Hz), and T_c is period of the sine-sweep (summation of single actuation period t_d and no actuation time between two successive actuations t_p). 1P and 10P frequencies are selected for the numerical values of f_0 and f_1, respectively, since such a range is found to have important frequency content for the present ATR system. Integration of the frequency equation, Eq. (6.2), will give the phase angle of the chirp ϕ_c as

$$\phi_c(t) = \left(f_0 t + \frac{f_1 - f_0}{2T_c} t^2\right) 2\pi \tag{6.3}$$

where the phase is in radians. The sine-sweep signal is generated using the unwrapped azimuthal location quantities. The relation between rotor rotational speed Ω (rpm) and the azimuthal location ψ is

$$\psi = \frac{360}{60} \Omega t \tag{6.4}$$

where time t is in seconds. A pseudo-time $\hat{t}$ is introduced based on the previously established relations, and uniformly distributed phase of N chirps over 360° can be produced by considering the number of the chirps that have already been generated, n_c, and shifting the time vector accordingly, so that

$$\hat{t} = \left[\psi - \left\{-360 + \mathrm{mod}\left(360\frac{n_c}{N}, 360\right)\right\}\right] \frac{60}{360\Omega} \tag{6.5}$$

where "mod" is the modulo function that returns the remainder obtained from the division of two arguments. The constructed chirp signal vector $\mathbf{U_c}$ with amplitude A_c for the rotor system can be represented as

$$\mathbf{U_c} = A_c \sin\left[2\pi\phi_c\left(\hat{t}\right)\right] \mathbf{V} \tag{6.6}$$

where $\mathbf{V}$ is a vector of length b, and collective, cyclic, and differential mode of actuation among the blades can be achieved by adjusting the elements of $\mathbf{V}$. In case of four-bladed rotor system, $\mathbf{V}$ for collective mode will be $[\ 1\ \ 1\ \ 1\ \ 1\ ]^T$, while $[\ 1\ \ -1\ \ 1\ \ -1\ ]^T$ for differential mode. A block diagram which generates the sine-sweep input signals described so far is illustrated in Fig. 6-1, and it is a part of the actual Simulink program used to implement chirp actuation during the forward flight testing.

Using the algorithm established, a collective mode chirp input signal is constructed with the amplitude of 1,000 V and nine phase angle divisions over 360° for the present

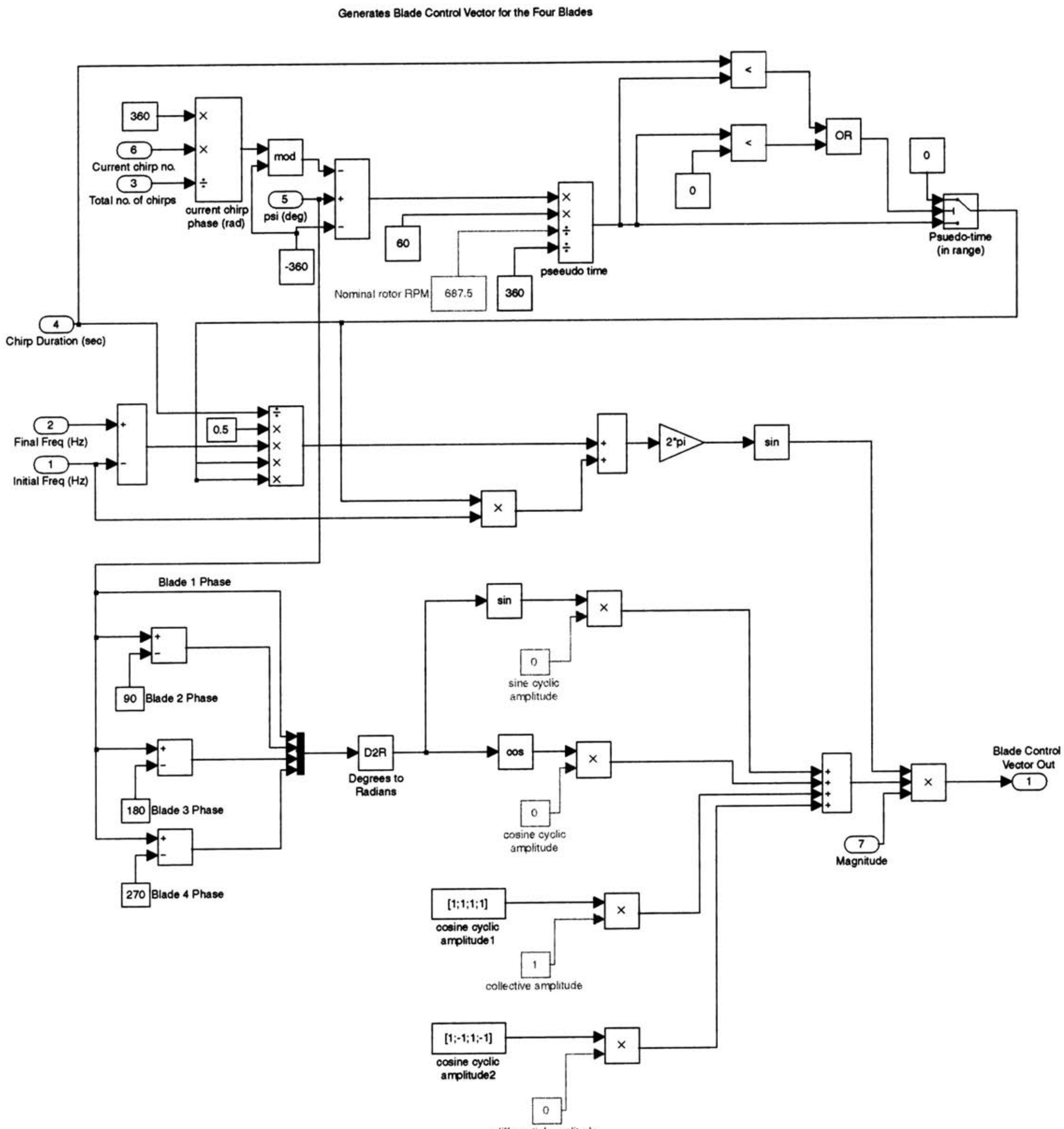

Figure 6-1: Simulink model of the sine-sweep input signal generator

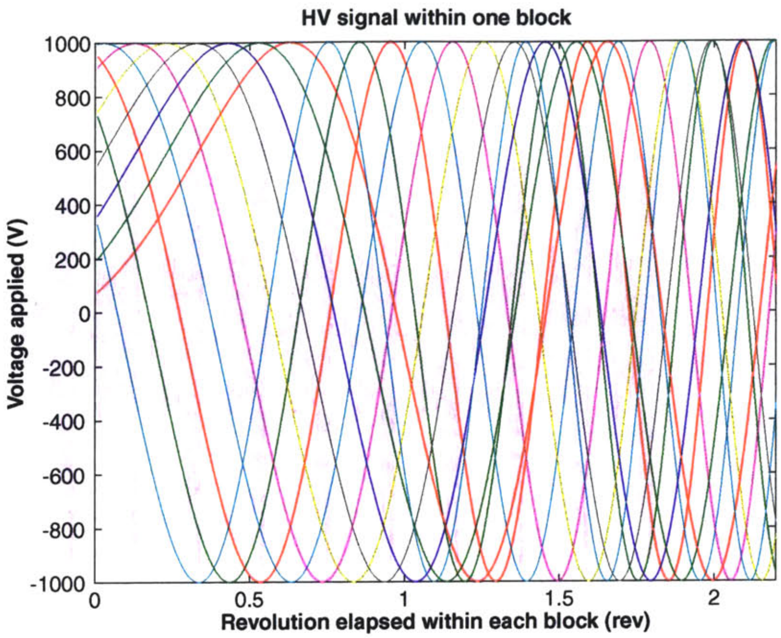

Figure 6-2: Collective mode sine-sweep signals generated with 9 divisions of phase angles

four-bladed ATR system identification. According to the definition of collective mode, all four blades have the same synchronous input signals for actuation, therefore one signal corresponding to Blade No. 1 may become a representative of all the input signals. In Fig. 6-2, representative signal generated for each different phase angle is overlapped with one another along the azimuthal location. It can be clearly seen that the initiation phase angle for each signal is uniformly separated, therefore all the signals conduct one complete sweep of 360° azimuthal location.

6.3 Results of the ATR System Identification

6.3.1 Collective Mode of Actuation

Using the constructed sine-sweep input signal, fixed- and rotating-system response of the ATR system at the low-speed level flight condition which was considered in Chapter 5 are calculated by the time domain analysis. At first, a series of collective mode actuation signal, as shown in Fig. 6-2, is applied, and its response is examined

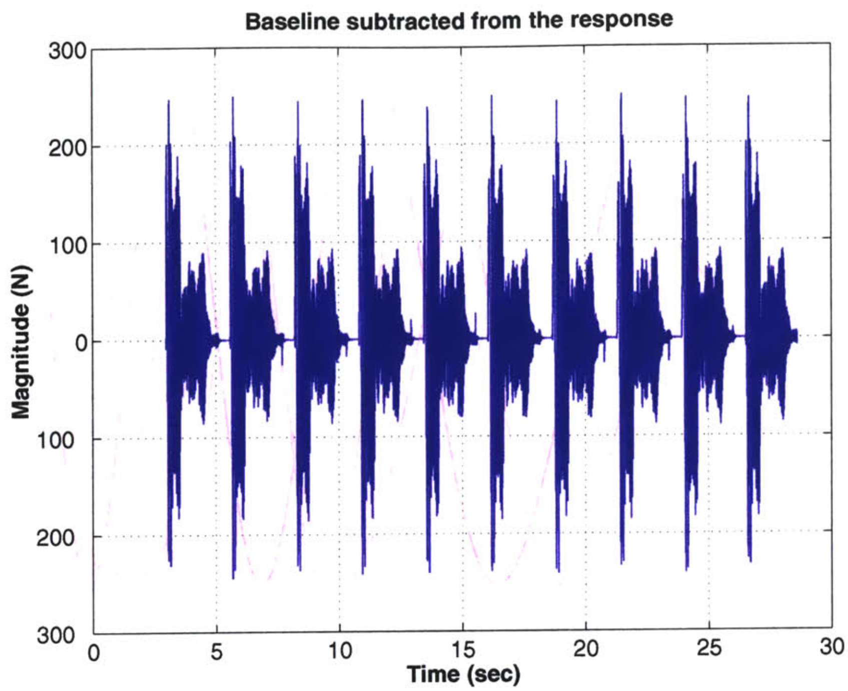

Figure 6-3: Time history of hub vertical shear loads from which the baseline loads are subtracted when the collective mode twist actuation is applied as described in Fig. 6-2

for the system identification. Before applying the system identification algorithm suggested in Appendix E.3, the amplitude of baseline loads must be subtracted from those under actuation. The amount of loads added to the baseline quantity becomes the object of transfer relationship. Time history of the ATR hub vertical shear loads from which the baseline loads are subtracted are shown in Fig. 6-3 from the simulation result using the collective mode sine-sweep actuation signal. Note that the hub vertical shear loads now oscillates around zero N, not near 1,000 N as in the case including the baseline loads.

The system identification scheme proposed in Appendix E.3 is now applied with the weighting factor α amounting to 10^{14}, and it is attempted here to estimate five harmonic transfer functions, i.e., G_{-2}, G_{-1}, G_0, G_{+1}, G_{+2}, at a time. Resulting transfer functions estimated are shown in Fig. 6-4, and G_0 is found to have amplitude which is significantly larger compared with the others.

This leads to the possibility that the response of the ATR system could be de-

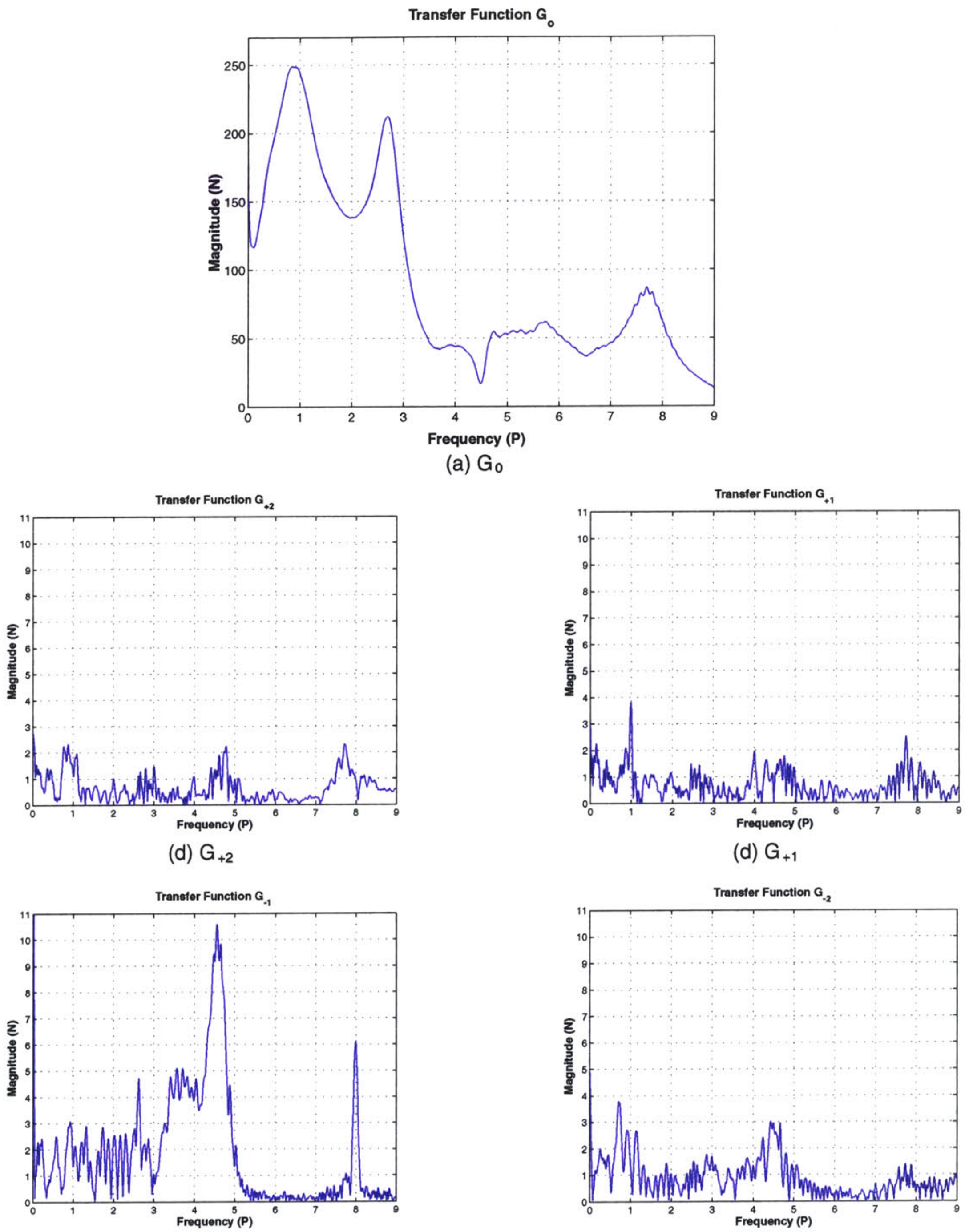

(a) G_0

(d) G_{+2}

(d) G_{+1}

(d) G_{-1}

(d) G_{-2}

Figure 6-4: Five harmonic transfer functions estimated for the hub vertical shear loads during the collective mode actuation

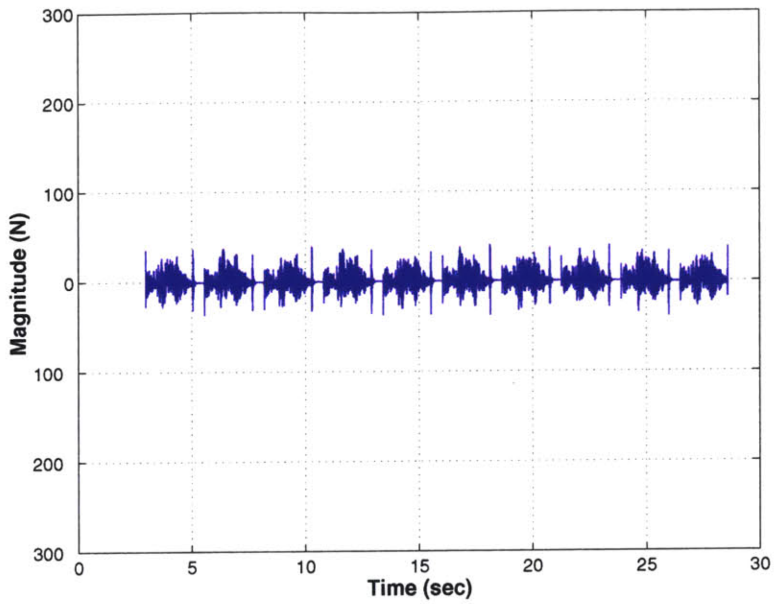

Figure 6-5: Component remaining from the original response after subtracting the one represented by G_0

scribed only by its G_0 component, just like in a linear time-invariant system. Such simplification can be verified by showing how large the remaining components will be from the total response by subtracting those represented by G_0. In Fig. 6-5, the remnant component from the original response after subtracting the one described by G_0 is plotted in time domain. As it is compared with the original response in Fig. 6-3, it is reduced by more than 1/3 in its amplitude. This implies that the energy contained in the remnant component becomes less than 1/9 of that in the original response since the energy is proportional to the square of the amplitude. It is therefore concluded that approximately 90% of the ATR system response can be described by G_0 alone when it is under the actuation of collective mode. This leads to the idea of regarding the present ATR system as a LTI system, and it will be verified once again by the polar plot later in this section.

More insight about the blade dynamics can be extracted from a Bode diagram of the hub vertical shear load, G_0, which was already described by its fan plot in Fig. 3-2. It is recognized that the peaks approximately match the frequencies of rigid and elastic flap bending modes and elastic torsion mode of the blades, as illustrated

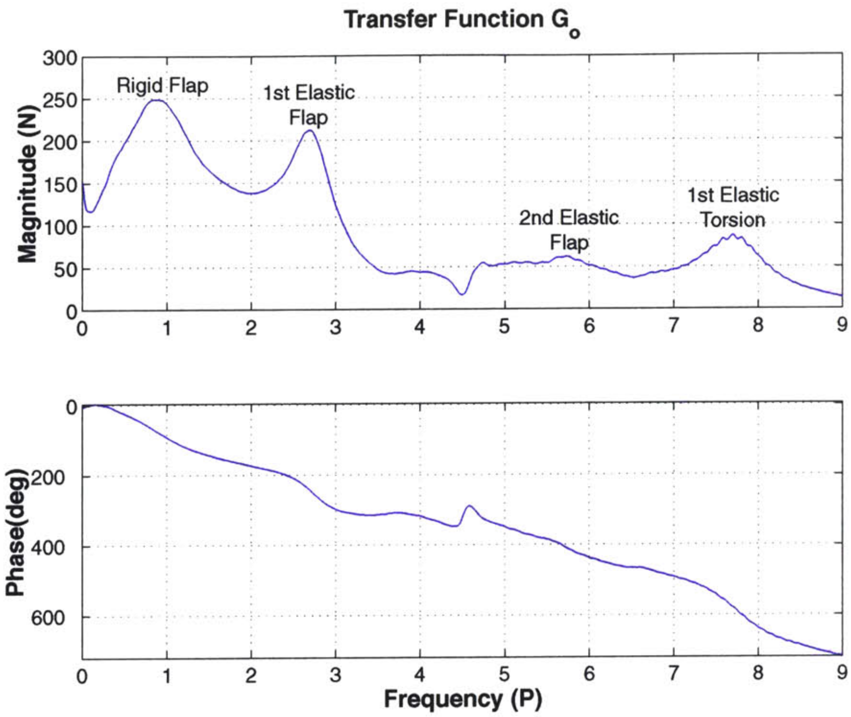

Figure 6-6: Harmonic transfer function G_0 of the hub vertical shear loads during the collective mode actuation

in Fig. 6-6. Furthermore, the property of G_0 being able to approximate the LTP system can be verified by comparing with the polar plot of the hub vertical shear loads obtained in Section 5.3.3. An amplitude of 47 N and phase delay of 317° can be read from the Bode diagram of G_0 in Fig. 6-6 at 4P excitation frequency. This information exactly matches those included in the polar plot of the hub vertical shear loads under the sine-dwell actuation at frequency 4P, which is illustrated in Fig. 6-7. In fact, IBC-mode 4P sine-dwell actuation considered in Chapter 5 generates exactly the same actuation signal as the collective mode considered here. The maximum amplitudes during IBC-mode 4P sine-dwell actuation occur at 90°, 180°, 270° azimuth after blade No. 1, respectively, which eventually places them at Blade No. 2, No. 3, No. 4, respectively. This results in equivalent signal used in the collective mode of actuation. Therefore, both of open-loop control simulation using IBC-mode sine-dwell actuation in Chapter 5 and system identification using sine-sweep actuation here describe the system behavior in a consistent manner.

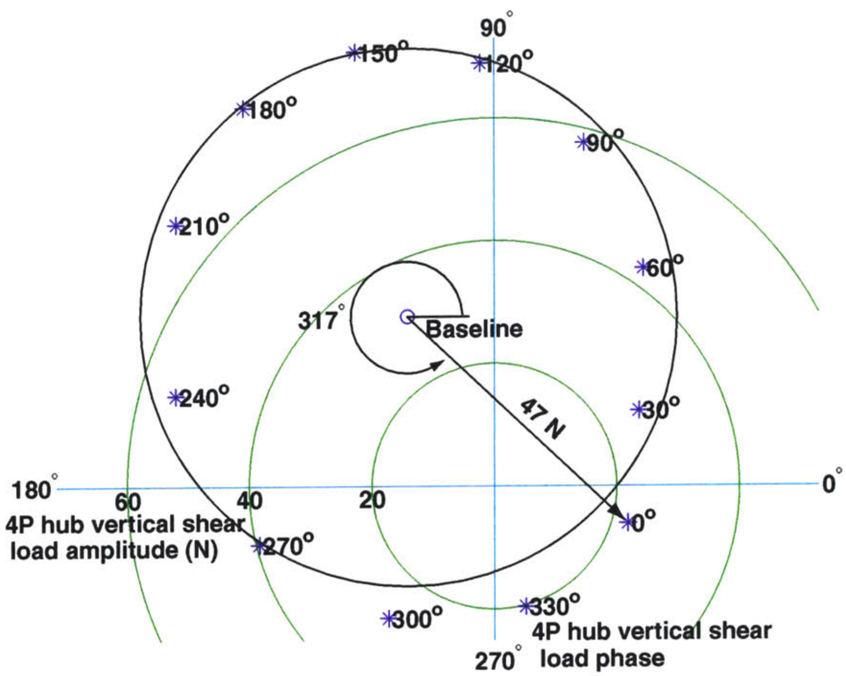

Figure 6-7: Polar plot of 4P hub vertical shear loads variation during 4P sine-dwell actuation

Another important characteristic of the present ATR system under collective mode of actuation can be extracted from the polar plot in Fig. 6-7. As indicated in this figure, the load variation under actuation can be approximated by a circle centered around the baseline load point. Therefore, this confirms again that the present ATR system behaves very similar to a LTI system under collective mode actuation. Based on this simplification to a LTI framework, a closed-loop controller will be designed.

6.3.2 Cyclic Mode of Actuation

Based on the same formulas introduced in Section 6.2, sine-sweep input signals for longitudinal and lateral cyclic mode of blade actuation may also be generated. By using these input signals and executing the same identification processes as described in Section 6.3.1, harmonic transfer functions corresponding to these two modes of actuation are estimated as well. Again, all the other components except G_0 in the result turn out to have much lower magnitudes. Therefore, the LTI simplification is

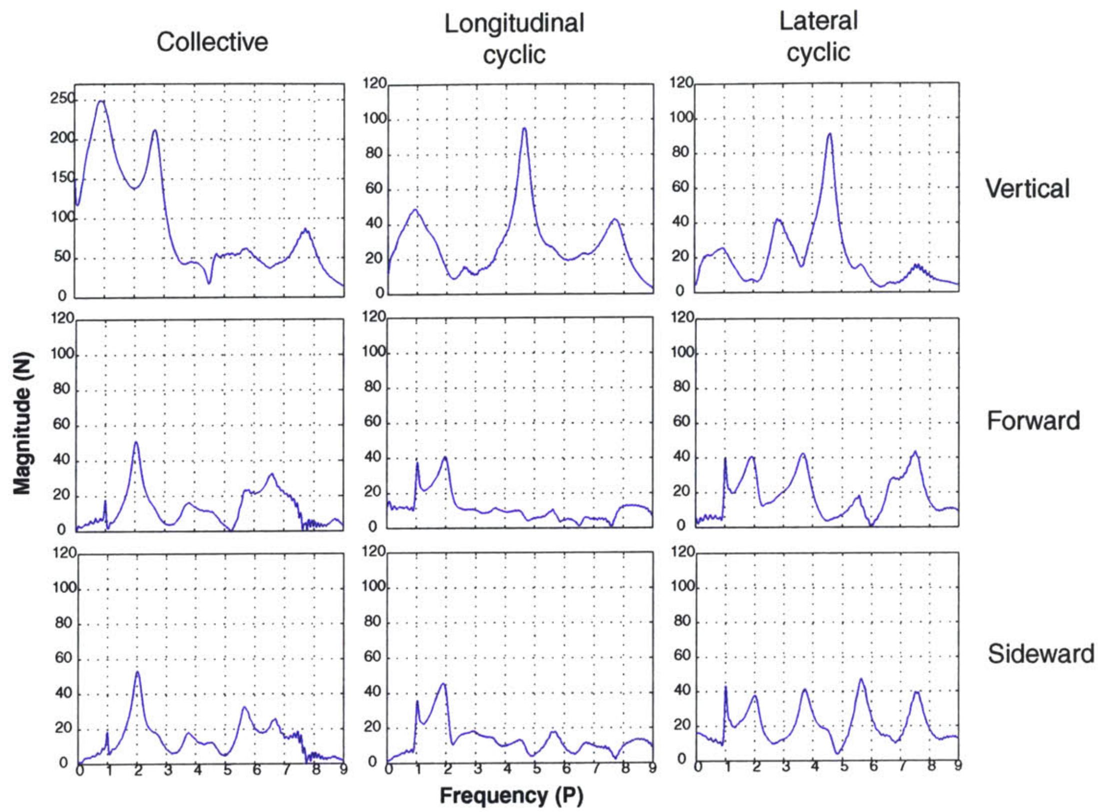

Figure 6-8: Matrix of G_0 estimated for three components of 4P hub shear vibratory loads versus three modes of blade actuation

still valid for these modes of actuation. All the identification results including the collective mode previously obtained may be represented as a transfer matrix relating three components of the hub shear loads versus three modes of blade actuation signal as shown in Fig. 6-8. Note that the vertical component versus the collective mode actuation (the uppermost and leftmost one) is only drawn in different scale from the others for an easy examination of the plots.

This transfer matrix leads to the idea of a multiple-component closed-loop controller which combines the three modes of blade actuation simultaneously. It may be designed for elimination of either single component of hub shear force or multiple-components of them at a time. For example, suppose the case of eliminating only the vertical components of 4P hub shear vibratory loads. From the analytical results presented in Fig. 5-8, the baseline amplitude for this component of the hub vibratory load was predicted as approximately 31 N. However, from Fig. 6-8, the amplitudes of the hub vertical vibratory loads altered by the application of each actuation mode are found to be 47 N, 34 N, and 35 N at 4P frequency, respectively. Therefore, it can be concluded that the application of the collective mode only of blade actuation is theoretically enough for a complete elimination of the 4P hub vertical vibratory loads at this flight condition. This possibility of complete elimination by the collective mode actuation is also implied by the polar plot in Fig. 6-7. In the figure, the plot encloses the origin, meaning that 4P hub vertical vibratory load may become zero by adjusting the amplitude (less than the maximum amplitude considered in Fig. 6-7) and phase of 4P IBC mode actuation (which is the same as 4P collective mode) appropriately. This conclusion may contradict the observation in the open-loop control sine-dwell test that the collective mode of actuation was less effective in vibration reduction. This contradiction may lie in the same context as the discrepancy generally found in the load amplitude results, because different degrees of the vertical load variation were obtained by 4P IBC-mode sine-dwell actuation between analysis and experiment (See Fig. 5-8 (a)). Moreover, an appropriate combination of the three actuation modes becomes equivalent to IBC mode, which was shown to be most effective in the open-loop control test. This combination is expected to bring an additional elimination of the other components besides the vertical loads. More discussion on the multiple-component closed-loop controller is given in Chapter 7.

Chapter 7

Closed-loop Controller for Vibration Reduction in Forward Flight

7.1 Overview

The results from system identification in Chapter 6 are utilized here to design a closed-loop controller for hub shear vibratory load reduction. As briefly mentioned in Section 5.3.3., the so-called **T** matrix approach has been traditionally used by researchers investigating higher harmonic control to identify transfer matrix [8, 13]. This approach resulted in a rather complicated structure of a closed-loop controller in order to implement the modulation and demodulation phases of the scheme. However, it was recently found that such a complex controller structure can be reduced to a classical disturbance rejection algorithm [9, 10]. This results in a simple LTI feedback compensator. In this thesis, a closed-loop controller based on this simple structure is attempted. Stability of the closed-loop system is checked first. Then, the vibratory load reduction capability of the designed controller is demonstrated numerically by combining with the time domain analysis built for the ATR system.

7.2 LTI Feedback Compensator for Disturbance Rejection

As introduced in Eq. (5.3), under the assumption of quasisteady condition and linearity, the amplitudes of the sine and cosine components of the vibrations at the b/rev frequency can be represented by

$$\mathbf{z} = \mathbf{T}\mathbf{u} + \mathbf{z_o} \tag{7.1}$$

where $\mathbf{z}$ is a vector of vibration amplitudes, $\mathbf{T}$ is the constant control response matrix, $\mathbf{u}$ is the vector of b/rev actuation amplitudes, and $\mathbf{z_o}$ is the vector of the vibration amplitudes with no actuation (baseline). Here, $\mathbf{z_o}$ is the disturbance to be rejected. The algorithm traditionally adopted by previous researchers [8, 14, 16, 11, 12, 13] is based on the idea of canceling the disturbance $\mathbf{z_o}$ by use of the higher harmonic swashplate input $\mathbf{u}$. Since the disturbance $\mathbf{z_o}$ is unknown, the approach is to measure the vibration at each time step and adjust the swashplate input $\mathbf{u}$ to just cancel that disturbance. The resulting control becomes

$$\mathbf{u_{n+1}} = \mathbf{u_n} - \mathbf{T}^{-1}\mathbf{z_n} \tag{7.2}$$

where the subscripts denote the index of the time step. The measurement of the vibration $\mathbf{z_n}$ is accomplished by a Fourier decomposition of the vibration at the b/rev frequency. A block diagram of the resulting controller is shown in Fig. 7-1. This control algorithm exhibits a quite complicated structure because of the modulation and demodulation tasks which are located in front of and behind the inverted $-\mathbf{T}$ matrix. The necessity of these modulation and demodulation tasks is originated partly from the fact that the constant control response matrix $\mathbf{T}$ is evaluated by the sine-dwell open-loop actuation at b/rev frequency.

However, it was recently shown that such a complex higher harmonic control algorithm for vibration rejection can be reduced analytically to a single input/single

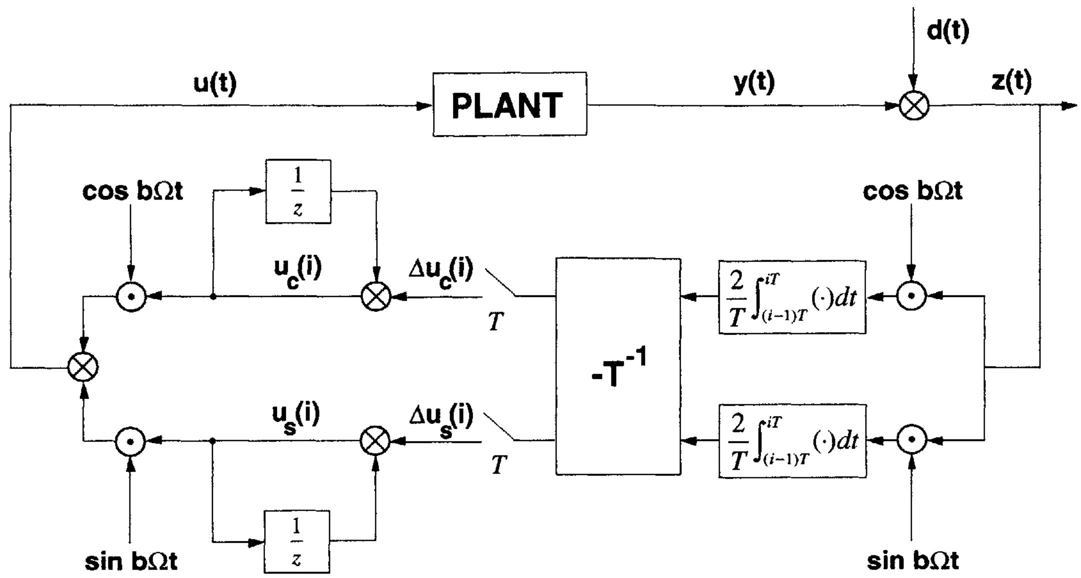

Figure 7-1: Block diagram of the higher harmonic control system adopted by researchers using quasisteady helicopter plant model [9]

output LTI system for a given plant transfer function $G(s)$ [9, 10]. According to this derivation, the block diagram shown in Fig. 7-1 is equivalent to an LTI feedback compensation structure, as illustrated in Fig. 7-2. The feedback compensator, $K(s)$, becomes

$$
\begin{aligned}
K(s) &= \frac{2k(As + Bb\Omega)}{s^2 + (b\Omega)^2} \qquad (7.3)\\
k &= \frac{1}{T}
\end{aligned}
$$

$$A = \mathrm{Real}\left\{\frac{1}{G(jb\Omega)}\right\}, \qquad B = -\mathrm{Imag}\left\{\frac{1}{G(jb\Omega)}\right\}$$

where T is the blade passage period. Furthermore, this LTI feedback compensator structure turns out to be essentially the same as a classical disturbance rejection algorithm, which is to eliminate an almost pure harmonic signal at constant frequency ω_o with the following compensator

$$H(s) = \frac{c_1 s + c_2}{s^2 + \omega_o^2} \qquad (7.4)$$

Stability and performance issues of the closed-loop system associated with this feed-

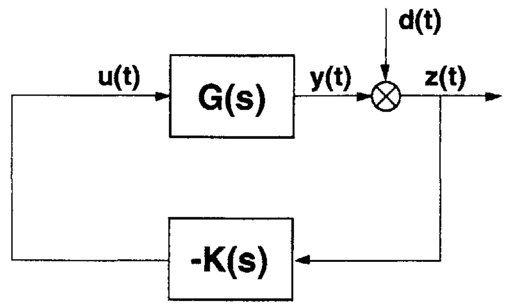

Figure 7-2: Block diagram of the LTI feedback compensator equivalent to HHC algorithm for vibration rejection [9]

back compensator were analytically investigated by the same authors and included in [9, 10]. In this thesis, a closed-loop controller for reducing hub shear vibratory loads during the ATR forward flight will be designed based on this feedback compensator using the LTI plant transfer function identified in Section 6.3.

7.3 Stability of the Closed-loop System

7.3.1 Original Feedback Controller

Before implementing the controller, the stability of the closed-loop system should be evaluated in order to ensure whether it is an appropriate controller. For this purpose, a loop gain, which is the product of the identified plant transfer function $G_0(s)$ (shown in Fig. 6-8) and the designed compensator $K(s)$, is investigated in frequency domain. Among the transfer matrix components presented in Fig. 6-8, the one for the hub vertical shear related only with the collective mode actuation is considered first. This implies a single-input single-output controller which reduces the hub vertical vibratory loads by use of the collective mode of blade actuation only. Its capability of complete vibration elimination within the hub vertical loads is already predicted from the transfer function estimate in Section 6.3.2.

Bode plot of the loop gain for the present closed-loop system is calculated and shown in Fig. 7-3. There exists a possible instability at the frequencies where the gain of the loop transfer function exceeds unity. Since the designed compensator has

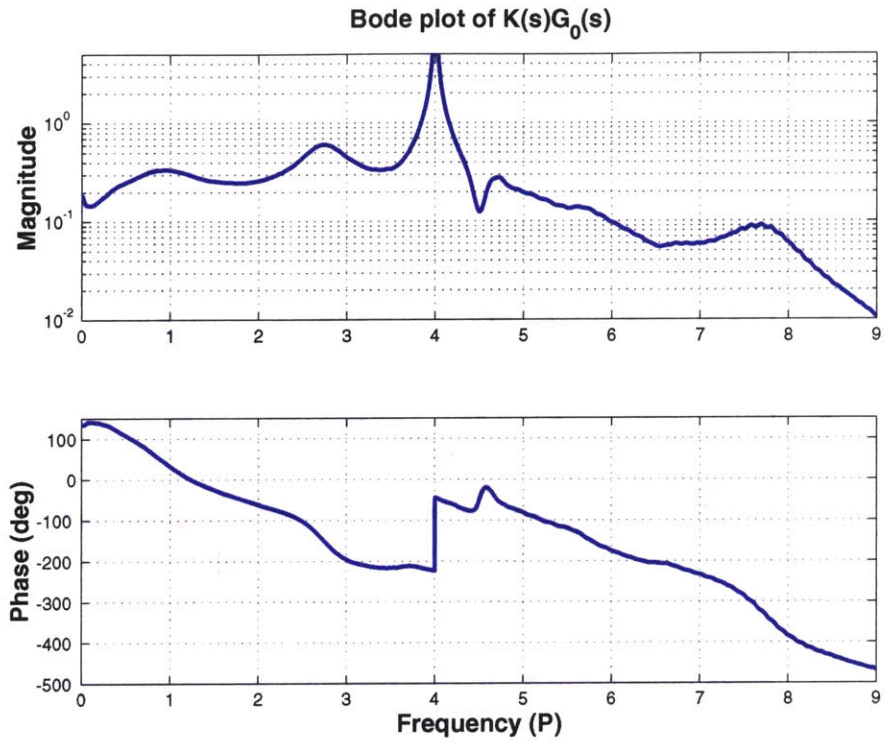

Figure 7-3: Bode plot of the loop transfer function

an infinite weighting at 4P frequency, the gain of the loop transfer function goes to infinity at the same 4P frequency, which makes it exceed unity over a narrow region centered at this frequency. Then, the variation of the phase within this region will determine the stability of the closed-loop system.

Another useful method of checking the stability of the controller is to examine the magnitude versus phase plot (Nichols plot) of the loop transfer function. Nichols plot of the present closed-loop system without any modification applied to $K(s)$ is displayed in Fig. 7-4 (a). The stability of the system is ensured if no encirclements of the critical point (unity magnitude at 180° of phase). This critical point is designated by a small circle in Fig. 7-4. In the same plot, contours of constant disturbance attenuation (or amplification) are also plotted according to the following relation

$$\frac{y}{d} = \frac{1}{1 + K(s)G_0(s)} \tag{7.5}$$

The closed contours around the critical point with positive figures represent degrees of

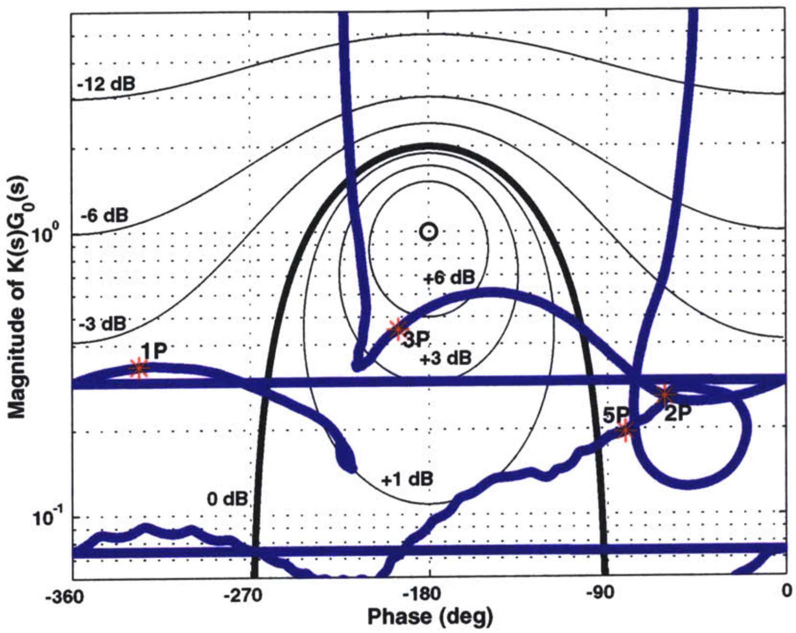

(a) Original

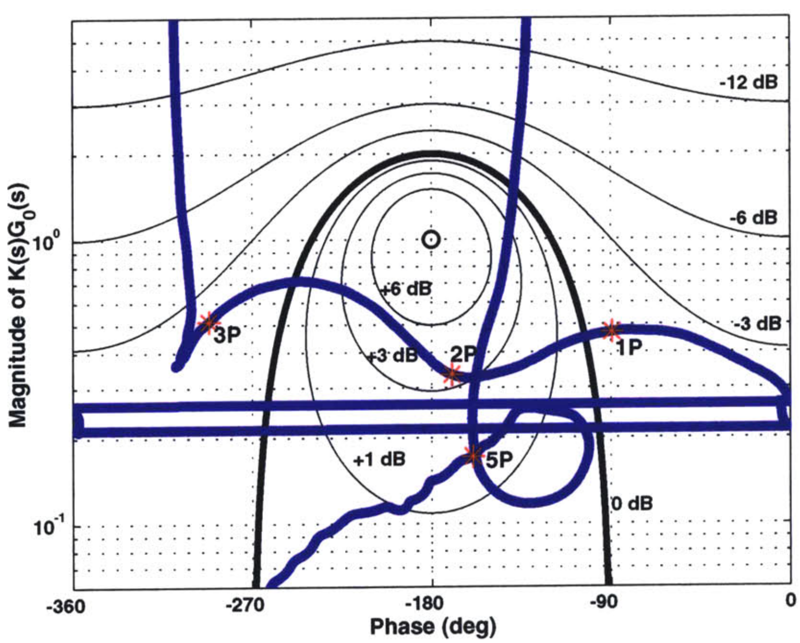

(b) Modified

Figure 7-4: Nichols plot of the loop transfer function vibration amplification. The inverted U-shaped contour with thicker line represents 0 dB boundary, where no vibration attenuation or amplification is obtained. The other contours indicate how much attenuation results (in dB) for the corresponding loop gain. Also, along the loop gain line, corresponding frequencies are designated by asterisks to see which frequency content is involved with a possible instability near the critical point. According to Fig. 7-4 (a), the present controller with the original $K(s)$ turns out to have gain margin of approximately 5.4 dB, and phase margin of 36°. In principle, this level of stability margin is regarded as enough for a general feedback compensator.

7.3.2 Modified Feedback Controller

When the gain of the controller is increased, i.e, the closed-loop gain line is shifted upward, there appears a chance of instability since it makes the gain margin diminished. Instability induced from this lack of gain margin is practically manifested during the numerical simulation, which will be described in the following section. Therefore, a modification on the original controller is needed to avoid this type of instability. The solution for this is to alter the closed-loop gain to have new phase characteristics, which is shifted by 45° from its original one. This modification is implemented by changing the transfer function for $K(s)$ in the following way

$$K(s) = \frac{2k(A's + B'b\Omega)}{s^2 + (b\Omega)^2} \tag{7.6}$$

where

$$A' = \mathrm{Real}\left\{(A - jB)e^{j(-45^\circ)}\right\}$$
$$B' = -\mathrm{Imag}\left\{(A - jB)e^{j(-45^\circ)}\right\}$$

where A and B are the same parameters as defined in Eq. (7.3). The resulting controller with the modification generates a new Nichols plot which is shown in Fig. 7-4 (b). Examining the result, the phase of the modified closed-loop gain is shifted as desired. Notice, however, that the magnitude of the closed-loop gain is slightly changed in Fig. 7-4 (b). The amount of such change in magnitude is observed as so small that no significant impact on the overall system characteristics is expected.

From the preliminary simulation of the resulting closed-loop controller, it is also observed that the steady component of the hub vertical loads is decreased by the controller engagement, as well as 4P vibratory component. This is due to the fact that the suggested controller $K(s)$ has a significant amount of gain at zero frequency. To improve the controller regarding this problem, a pole is added to its current transfer function, Eq. (7.6), at 0.4P frequency location. This will make the controller have negligible gain at zero frequency so that it may not affect the steady component. Therefore, the final form for the controller transfer function $K(s)$ becomes

$$K(s) = \frac{s}{(s + b\Omega/10)} \cdot \frac{2k(A's + B'b\Omega)}{s^2 + (b\Omega)^2} \tag{7.7}$$

So far, the sole component of the transfer function from the previous system identification, $G_0(s)$, has been used to represent the plant for the stability check and preliminary performance estimation. This simplification is due to the finding that more than 90% of the system response can be represented by $G_0(s)$ only under the three modes of blade actuation. In the following section, however, the time domain analysis will be used for the demonstration of the resulting controller. This signifies that the original plant with all its harmonic transfer function components will be present, and the performance of the closed-loop controller based on the simplified design can be numerically tested.

7.4 Numerical Demonstration of the Closed-loop Controller

In the preceding section, the task of the closed-loop controller design and its stability check was conducted by considering only the LTI component $G_0(s)$ among the estimated harmonic transfer functions. However, it is expected that the resultant controller will still behave well when combined with the original plant which has all the components of the harmonic transfer functions. In this section, a numerical demonstration of this situation is attempted using the time domain analysis.

The resulting LTI feedback compensator, whose transfer function in continuous-time is described by Eq. (7.7), can be easily incorporated in the time domain analysis by transforming it into a discrete-time state-space approximation. Using the `c2d` command based on a Tustin approximation, which is provided in MATLAB, an approximately equivalent discrete time state-space representation of the same feedback compensator can be obtained with the specific time step size selected for the analysis. The equivalent LTI feedback compensator which is transformed into the discrete-time state-space version can be expressed as

$$\begin{aligned} \mathbf{x}_{k+1} &= \mathbf{A}\mathbf{x}_k + \mathbf{B}\mathbf{u}_k \\ \mathbf{y}_k &= \mathbf{C}\mathbf{x}_k + \mathbf{D}\mathbf{u}_k \end{aligned} \tag{7.8}$$

where $\mathbf{x}_k$ is the state variables internal to the controller estimated at time step k. $\mathbf{u}_k$ is a sensor measurement from the plant, i.e., hub vertical shear load measurement in this case, and $\mathbf{y}_k$ is a controlled quantity of electric field applied at the blade integral actuators at time k in collective mode. Since the resultant controller is described as a third-order system in Eq. (7.7), its state-space representation involves three state variables, meaning that $\mathbf{x}_k$ becomes a 3×1 vector.

After incorporating the matrix representation described in Eq. (7.8) into the time domain analysis, a simulation is executed in order to evaluate the performance of the closed-loop controller. It is still required to establish the steady-state equilibrium for a specific flight condition before engaging the vibration minimizing controller. Otherwise, huge hub vibratory loads which are induced during the transient period before the steady state equilibrium is reached may generate unrealistically large control signal. Therefore, the initial 3-second period of no actuation is applied again to obtain the trim condition. Then, the controller is engaged with a different magnitude of its gain constant discretely adjusted at 0.5, 1.0, and 2.0 within each 2-second period.

The result of the time domain analysis is displayed as a time history of the hub

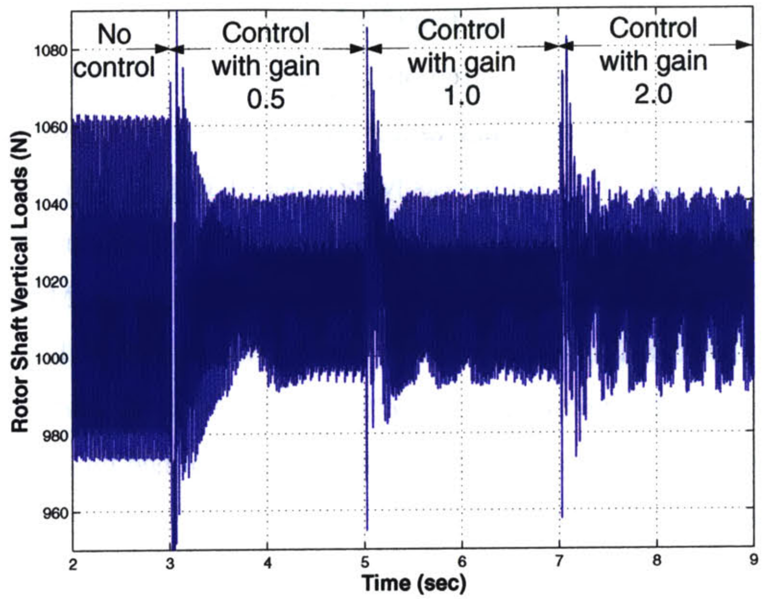

Figure 7-5: Time history of the hub vertical shear loads for $\mu = 0.140$, $\alpha_S = -1^o$, and $C_T = 0.0066$ without and with the closed-loop controller engaged

vertical shear loads in Fig. 7-5. As one can see, the vibratory load components without control action is significantly reduced by the engagement of the controller. By adjusting the constant gain in the controller, different response behaviors are obtained. At first, by increasing the gain, the settling time for the response is improved. This is clearly seen when comparing the settling time between the case of gain 0.5 and that of 1.0. However, when it comes up to gain 2.0, an instability occurs, which is induced from insufficient gain margin of the system. Although the current controller should be protected from this instability, a considerable amount of vibration near at 2.5P frequency is present in the response of gain 2.0. The other components of the hub shear loads are influenced little by the current controller engagement.

Qualitatively looking at Fig. 7-5, all the gains produce a similar degree of vibration reduction control. This suggests to examine the result in a quantitative way. For this purpose, one needs to investigate a power spectral density distribution of the hub vertical loads with respect to response frequency. Using the `psd` command provided in MATLAB, power spectral density distributions of the hub vertical shear load amplitudes without and with the controller engaged are computed in Fig. 7-6. It is seen

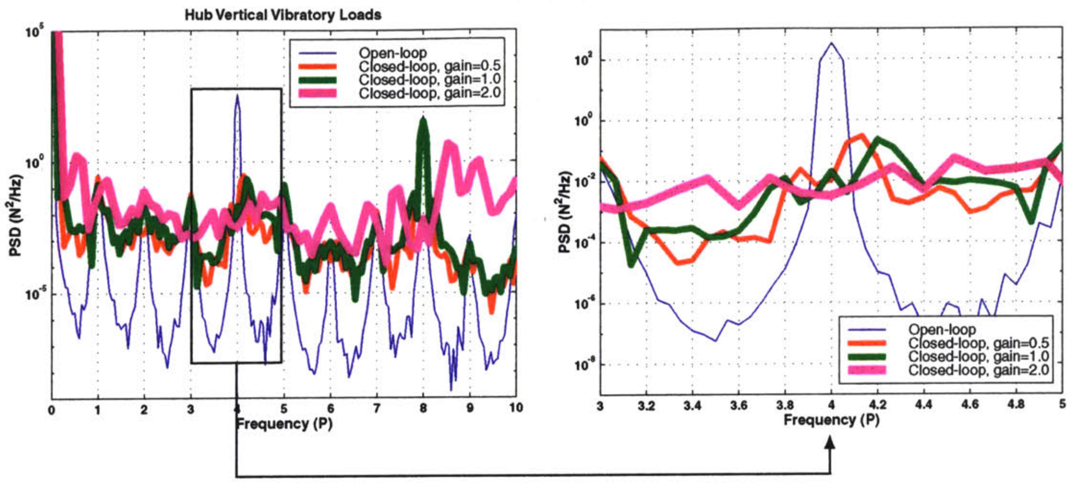

Figure 7-6: Power spectral desnity distribution of the hub vertical shear loads for $\mu = 0.140$, $\alpha_S = -1^o$, and $C_T = 0.0066$ without and with the closed-loop controller engaged

that the vibratory component at 4P frequency is decreased by different degree for each gain constant applied. According to this result, more than 90% of the 4P vibratory load existing in the original response is eliminated by the controller engagement. However, outside the narrow band of 4P frequency, it is observed that undesirable increase of vibratory load components are caused by the controller. Also, another significant vibration amplitudes are found at integral multiples of 4P frequency (e.g., amplitude at 8P frequency in Fig. 7-6). These vibration components are rarely affected by the current controller design, and explain the remnant vibration after the 4P component is eliminated. Therefore, it is recommended to improve the present controller into one that can eliminate disturbance in multiple harmonic components [25] in order to reduce other vibration components simultaneously.

Chapter 8

Conclusions and Recommendations

8.1 Summary

This thesis presents the numerical and experimental investigations of integral twist actuation of helicopter rotor blades as a mean to reduce vibration induced in forward flight. Active rotor blade with embedded anisotropic piezoelectric actuators is designed using the analytical framework established in this thesis. An analytical framework is proposed to investigate integrally-twisted helicopter blades and their aeroelastic behavior during different flight conditions. This framework is composed of frequency domain analysis for hover, and time domain analysis for forward flight. Both analyses are based on the same three-dimensional electroelastic beam formulation with geometrical-exactness, and are coupled with the appropriate finite-state dynamic inflow aerodynamics model. A prototype blade is manufactured and bench tests are conducted to confirm its structural characteristics and adequacy of the implementation process. Hover test of a four-bladed fully-articulated rotor is performed using the prototype blade with the other dummy blades. A good correlation is obtained regarding the control sensitivity of the active blade at hover condition. Based on the prototype blade design, four ATR test blades are manufactured in order to compose a fully-active-blade rotor system. This rotor system is tested in the NASA Langley Transonic Dynamics Tunnel in a first-ever forward flight condition for an integrally-twisted rotor.

The aeroelastic analysis developed for hover condition proved to be appropriate for predicting dynamic behavior of the active blade both at static and hover condition. However, the time domain analysis for forward flight condition showed a significant discrepancy in amplitude of loads predicted in both fixed- and rotating-frame when compared with the wind-tunnel testing data. Factors that influence the discrepancy may be grouped into two classes. From the standpoint of aerodynamics, in order to predict accurately unsteady loads acting on helicopter rotor blades during forward flight, more sophisticated aerodynamics model may be required in the analysis, for example, a model considering dynamic stall, free wake, etc. Such sophistication in aerodynamics becomes even more important when dealing with higher harmonic control of blade twist. From the structural point of view, further dynamic characterization of the ARES testbed is required, and its representation should then be brought into the proposed framework. Although the test apparatus was configured to avoid mis-balance in the rotating system, any structural factor that was beyond the standard balancing effort was not pursued. This may have induced different vibration level, and this factor needs to be identified and included in the analysis.

However, the trend of the fixed-system load variation with respect to control phase showed a good agreement between the analysis and experiment, and the analytical results included sufficient details of typical helicopter and rotor blade dynamic behavior exhibited in forward flight. This supports to proceed to the tasks of system identification and closed-loop controller design based on the established forward flight analysis model.

System identification based on the linear time-periodic system theory was conducted to estimate the harmonic transfer functions between integral actuator electric field and hub shear vibratory loads. It turned out that only the linear time-invariant component was dominant under the three modes of blade actuation: collective, longitudinal cyclic, and lateral cyclic. This simplification into a LTI system has been observed by previous researchers investigating higher harmonic control of helicopter blades.

A closed-loop controller was designed based on the system identification results and on the classical disturbance rejection algorithm. A preliminary stability check was conducted, and the resultant LTI feedback compensator was demonstrated numerically by incorporating it in the time domain analysis model. Even with the original plant with all the LTP components, the designed controller showed a satisfactory vibration reducing capability.

This thesis has addressed several issues related with helicopter vibration reduction technology with integrally-twisted rotor blades, which are:

1. Development of an analysis framework for the rotor system with actively-twisted blades in hover and forward flight

2. Investigation of dynamic characteristics of ATR blade due to its integral actuation at bench and in hover

3. Investigation of impact upon the ATR fixed- and rotating-system loads due to blade twist actuation in forward flight

4. Estimation of harmonic transfer functions of the ATR system in forward flight based on the linear time-periodic system theory

5. Design and numerical demonstration of closed-loop controller which minimizes helicopter vibration by integral blade twist actuation

8.2 Conclusions

A number of conclusions can be drawn from the current helicopter vibration reduction study, and they are summarized as follows.

- Experimental structural characteristics of the prototype blade compare well with design goals, and predictions by the established framework correlate well with bench test results.

- The design strategy of the present ATR blade prove to be appropriate by confirming the actuation capability and structural integrity exhibited by the prototype blade and the modified test blades.

- The aeroelastic analysis developed for hover proves to be appropriate in predicting dynamic behavior of the active blade in both static and hover condition.

- The aeroelastic analysis model developed for forward flight condition in this thesis shows an appropriate degree of agreement with the experimental data. However, further refinements are recommended due to its significant discrepancy in amplitude of load estimated both in fixed- and rotating-system.

- It is found by both analysis and experiment that integral twist actuation of the rotor blades has a potential of the ATR system hub shear vibratory load reduction up to 90% by an open-loop individual blade control.

- The active aeroelastic framework showed to be appropriate for design, analysis, and simulation of future active twist rotor systems for vibration reduction.

- Only LTI component is found to be dominant among the harmonic transfer function components estimated for the ATR system under the three modes of blade actuation in forward flight. This enables the control problem to be simplified into a LTI system.

- A closed-loop controller which reduces hub shear vibratory loads at given system frequency is designed as a simple LTI feedback compensator, and more than 90% of the original hub vertical vibratory load is eliminated by the controller engagement in the numerical demonstration.

8.3 Recommendations

From the effort to solve the remaining problems encountered in this study, some recommendations follow, which will be beneficial to improve future integral blade twist actuation development.

- Refinement of the present active aeroelastic analysis for forward flight is recommended since a significant discrepancy was found between the model prediction and the experimental data acquired in the amplitude of the fixed- and rotating-system loads. Since the discrepancy is considered to result from the less sophisticated aerodynamics model adopted, analysis with more sophisticated model is recommended.

- The discrepancy in the in the amplitude of the fixed- and rotating-system loads also results from incomplete representation of the structural components existing in the testing apparatus. Thus, further dynamic characterization of the ARES testbed is recommended.

- System identification and closed-loop controller design was conducted based on the established analytical model due to the limited availability of the experimental data. However, in order to apply a closed-loop controller in the practical system, experimental data is recommended for final tuning of the controller.

- Further improvement of the vibration reduction capability through optimization study of the active blade design parameters is suggested. This includes tailoring of active and passive plies included in blade lay-up, sizing of the active region, etc. Basic dynamic characteristics of the blade such as the natural frequencies may be another influencing factor for control authority in specific frequencies.

- It is desirable to use the concept of integral blade twist actuation as a means of acoustic noise reduction for the rotor system. In order to analyze the active rotor system for such purpose, more refined aerodynamics model is required to accurately predict the pressure distribution around the blades in a specific flight condition. For a wind-tunnel experiment, quiet environments are required so that the reliable acoustic data may be collected. A noise-reducing closed-loop controller can be designed and tested by conducting the procedures suggested in this thesis.

Appendix A

State-space Formulation for Hover Analysis

Explicit expressions of the state space representation for hover analysis, Eq. (2.32), are provided. Since detailed expressions of the sub-matrices included in the matrices **E** and **A** in Eq. (2.33) are found in the appendices of [63], non-zero sub-matrices in the matrix **B** are only described in this section.

$$
\begin{aligned}
\frac{\partial F_S}{\partial V} &= \sum_i \left(\frac{\partial F_S}{\partial V}\right)_i \\
\left(\frac{\partial F_S}{\partial V}\right)_i &= \left[\frac{\partial f_{u_i}}{\partial V}\ \frac{\partial f_{\psi_i}}{\partial V}\ \frac{\partial f_{F_i}}{\partial V}\ \frac{\partial f_{M_i}}{\partial V}\ \frac{\partial f_{P_i}}{\partial V}\ \frac{\partial f_{H_i}}{\partial V}\ \frac{\partial f_{u_j}}{\partial V}\ \frac{\partial f_{\psi_j}}{\partial V}\ \frac{\partial f_{F_j}}{\partial V}\ \frac{\partial f_{M_j}}{\partial V}\right]^T \\
\frac{\partial f_{u_i}}{\partial V} &= 0 \\
\frac{\partial f_{\psi_i}}{\partial V} &= -\frac{\Delta l_i}{2} C^T C^{ab} \widetilde{(rF^{(a)}_{B_i} + tM^{(a)}_{B_i})} F_i \\
\frac{\partial f_{F_i}}{\partial V} &= -\frac{\Delta l_i}{2} C^T C^{ab} (rF^{(a)}_{B_i} + tM^{(a)}_{B_i}) \\
\frac{\partial f_{M_i}}{\partial V} &= -\frac{\Delta l_i}{2} \left(\Delta + \frac{\widetilde{\theta}_i}{2} + \frac{\theta_i \theta_i^T}{4}\right) C^{ab} (tF^{(a)}_{B_i} + sM^{(a)}_{B_i}) \\
\frac{\partial f_{P_i}}{\partial V} &= 0 \\
\frac{\partial f_{H_i}}{\partial V} &= 0 \\
\frac{\partial f_{u_j}}{\partial V} &= 0
\end{aligned}
$$

$$\begin{aligned}
\frac{\partial f_{\psi_j}}{\partial V} &= -\frac{\Delta l_i}{2} C^T C^{ab} \widetilde{(rF_{B_i}^{(a)} + tM_{B_i}^{(a)})} F_i \\
\frac{\partial f_{F_j}}{\partial V} &= -\frac{\Delta l_i}{2} C^T C^{ab} (rF_{B_i}^{(a)} + tM_{B_i}^{(a)}) \\
\frac{\partial f_{M_j}}{\partial V} &= -\frac{\Delta l_i}{2} \left(\Delta + \frac{\widetilde{\theta}_i}{2} + \frac{\theta_i \theta_i^T}{4} \right) C^{ab} (tF_{B_i}^{(a)} + sM_{B_i}^{(a)})
\end{aligned}$$

Appendix B

Time Integration Formulation for Forward Flight Analysis

The energy decaying time integration of the beam formulation mentioned in Section 2.5.2 is summarized as follows. The displacement-based form of beam formulation, Eq. (2.22), can be expressed conveniently as

$$(\mathbf{R}\mathbf{p}_B)^{\bullet} + \mathbf{U}[\widetilde{\dot{u}}]\mathbf{R}\mathbf{p}_B - (\mathbf{R}\mathbf{f}_B)' - \mathbf{U}[\widetilde{u_o'} + \widetilde{u}']\mathbf{R}\mathbf{f}_B = \mathbf{q} \tag{B.1}$$

where

$$\begin{aligned} \mathbf{R} &= \begin{bmatrix} C^{Bb}C^{ba} & 0 \\ 0 & C^{Bb}C^{ba} \end{bmatrix} \\ \mathbf{U}[.] &= \begin{bmatrix} 0 & 0 \\ [.] & 0 \end{bmatrix} \end{aligned}$$

Note that $\mathbf{q}$ in Eq. (B.1) now represents all the terms including the actuation forces at the right hand side of Eq. (2.21). A time discretization scheme can be applied first over the time step, from t_n^- to t_{n+1}^-:

$$\frac{\mathbf{R}_{n+1}^- \mathbf{p}_{Bn+1}^- - \mathbf{R}_n^- \mathbf{p}_{Bn}^-}{\Delta t} + \mathbf{U}\left[\frac{\widetilde{u_{n+1}^-} - \widetilde{u_n^-}}{\Delta t}\mathbf{G}_m\right]\frac{\mathbf{p}_{Bn}^- + \mathbf{p}_{Bn+1}^+}{2} \tag{B.2}$$

$$- (\mathbf{Q}_m \mathbf{f}_{Bm})' - \mathbf{U}\left[\frac{2}{\mathbf{a}_o}(\widetilde{u'_o} + \widetilde{u'_m})\right] \mathbf{Q}_m \mathbf{f}_{Bm} = \mathbf{q}_m$$

where $\mathbf{a}_o$ contains the components of the conformal rotation vector of the rotation from B_n^- to B_{n+1}^-, measured in a. The subscript m denotes the time step mid-point, and $\mathbf{f}_m$ refers to elastic forces at this mid-point. Also,

$$\begin{aligned}
\mathbf{Q}_m &= \begin{bmatrix} \mathbf{H}_m & 0 \\ 0 & \mathbf{G}_m \end{bmatrix} \\
\mathbf{H}_m &= \frac{C_{n+1}^{Bb} C^{ba} + C_n^{Bb} C^{ba}}{2} \\
\mathbf{G}_m &= \frac{2 C_m^{Bb} C^{ba}}{4 - \mathbf{a}_o}
\end{aligned} \tag{B.3}$$

Similar discretization is then applied across the discontinuous jump, from t_n^- to t_n^+:

$$\begin{aligned}
&\frac{\mathbf{R}_n^+ \mathbf{p}_{Bn}^+ - \mathbf{R}_n^- \mathbf{p}_{Bn}^-}{\Delta t} + \mathbf{U}\left[\frac{\widetilde{u_n^+} - \widetilde{u_n^-}}{\Delta t} \mathbf{G}_j\right] \frac{\mathbf{p}_{Bn}^- + \mathbf{p}_{Bn}^+}{2} \\
&\quad -(\mathbf{Q}_j \mathbf{f}_{Bj})' - \mathbf{U}\left[\frac{2}{\mathbf{b}_o}(\widetilde{u'_o} + \widetilde{u'_j})\right] \mathbf{Q}_j \mathbf{f}_{Bj} = \mathbf{q}_j
\end{aligned} \tag{B.4}$$

where $\mathbf{b}_o$ are the components of the conformal rotation vector of the rotation from B_n^- to B_n^+, measured in a. The subscript j denotes the time step mid-point, and $\mathbf{f}_j$ refers to elastic forces at this mid-point. Both of Eqs. (B.2) and (B.4) constitute a time marching integration process for the present forward flight analysis.

Appendix C

AFC Distribution in the ATR Prototype Blade

The following table presents the electromechanical coupling coefficients (d_{11} and d_{12}) of the individual AFC packs embedded in the ATR prototype blade along its spanwise location. It is noted that the distribution of the packs is designed so that those with the best performance can be located at the inboard of the blade and the performance difference between top and bottom surfaces at the same spanwise location is to be minimized.

Table C.1: Active properties of the AFC packs distributed in the ATR prototype blade (pm/V)

		BS 43.31 ~ 58.80 cm	BS 58.80 ~ 74.30 cm	BS 74.30 ~ 89.79 cm
Outer layer AFC at top surface	d_{11}	413	322	309
	d_{12}	−172	−134	−129
Inner layer AFC at top surface	d_{11}	327	310	286
	d_{12}	−139	−129	−119
Outer layer AFC at bottom surface	d_{11}	373	322	304
	d_{12}	−156	−134	−127
Inner layer AFC at bottom surface	d_{11}	355	315	296
	d_{12}	−149	−132	−124
		BS 89.79 ~ 105.3 cm	BS 105.3 ~ 120.8 cm	BS 120.8 ~ 135.8 cm
Outer layer AFC at top surface	d_{11}	276	256	231
	d_{12}	−115	−107	−97
Inner layer AFC at top surface	d_{11}	259	238	210
	d_{12}	−108	−100	−88
Outer layer AFC at bottom surface	d_{11}	273	256	222
	d_{12}	−114	−107	−93
Inner layer AFC at bottom surface	d_{11}	263	239	221
	d_{12}	−109	−100	−93

Appendix D

Material Properties of the ATR Test Blade Constituents

The following two tables present the material properties of the constituent materials used in the ATR test blades manufacturing.

Table D.1: Material properties of the constituents in the ATR test blades

	E-Glass fabric	**EA9628 adhesive**	**Rohacell foam spar**	**Rohacell foam fairing**
Thickness (μm)	114.3	101.6	-	-
Density (kg/m^3)	1,716	1,163	75	35
E_L (GPa)	19.3	2.38	0.0896	0.035
G_{LT} (GPa)	4.14	0.69	0.0296	0.0138
	Fiber glass uni-tape	**Flexible circuit**	**Front ballast weight (tungsten)**	**Strain gauge wires**
Dimension	thickness 203.2 μm	width 6.604 mm	diameter 4.7625 mm	diameter 40×0.381 mm
Density (kg/m^3)	1,799	3,044	19,100	8,900
E_L (GPa)	48.2	-	-	-
G_{LT} (GPa)	5.7	-	-	-

Table D.2: Properties of the AFC packs used in the ATR test blades

Thickness	218 μm
Density	3,967 kg/m^3
d_{11}	309 pm/V
d_{12}	-129 pm/V
E_L	20.5 GPa
E_T	11.6 GPa
ν_{LT}	0.454
G_{LT}	4.0 GPa

Appendix E

LTP System and its Identification

What follows is a summary of the identification technique for LTP systems presented in [62].

E.1 Characteristics of LTP system

Linear time periodic system can be represented in a state-space form as

$$\begin{aligned} \dot{x}(t) &= A(t)x(t) + B(t)u(t) \\ y(t) &= C(t)x(t) + D(t)u(t) \end{aligned} \tag{E.1}$$

where the matrices $A(t)$, $B(t)$, $C(t)$, and $D(t)$ are in general periodic, with period T. When a sinusoidal signal excites an LTP system, the system responds with the superposition of sinusoids not only of the input frequency ω, but also of several other frequencies, $\omega + n\omega_p$, each with its own amplitude and phase, where n is an integer, and ω_p is the system major frequency, given as

$$\omega_p = 2\pi/T \tag{E.2}$$

The frequencies $\omega + n\omega_p$ are shifted harmonics, and they are often referred to simply as "harmonics."

According to Floquet theory, which has been widely used in LTP system investigation, the state vector x, at time t, is related to the one at period T away by the discrete transition matrix $\mathbf{\Phi}$ of the system.

$$x(t+T) = \mathbf{\Phi}x(t) \tag{E.3}$$

In general, it also satisfies that

$$x(t+nT) = \mathbf{\Phi}^n x(t) \tag{E.4}$$

If $x(0)$ happens to be an eigenvector of $\mathbf{\Phi}$, with corresponding eigenvalue $\mathbf{z}$, the solution will satisfy

$$x(t+nT) = \mathbf{z}^n x(t) \tag{E.5}$$

for all t. This implies that $x(t)$ has the form

$$x(t) = e^{st}\bar{x}(t) \tag{E.6}$$

where $s = (\log \mathbf{z})/T$, and $x(t)$ is periodic. That is, $x(t)$ is an exponentially modulated periodic (EMP) function. This suggests that EMP functions are the appropriate signals to describe the LTP systems. This leads to a concept of using EMP signals to determine the transfer functions of LTP systems. Expressing the EMP signals as complex Fourier series of a periodic signal of frequency ω_p, modulated by a complex exponential component, the appropriate input signal becomes

$$u(t) = \sum_{n \in Z} u_n e^{s_n t} \tag{E.7}$$

where $s_n = s + nj\omega_p$ ($s \in C$), and u_n are Fourier coefficients of $u(t)$.

Similarly expressing the matrices in the state space representation, Eq. (E.1), in terms of their Fourier series, and using the harmonic balance approach, one obtains

$$\begin{aligned} s_n x_n &= \sum_{m \in Z} A_{n-m} x_m + \sum_{m \in Z} A_{n-m} u_m \\ y_n &= \sum_{m \in Z} C_{n-m} x_m + \sum_{m \in Z} D_{n-m} u_m \end{aligned} \tag{E.8}$$

The summations in the previous expression, Eq. (E.8), can be transformed into matrix form as

$$\begin{aligned} s\mathcal{X} &= (\mathcal{A} - \mathcal{N})\mathcal{X} + \mathcal{B}\mathcal{U} \\ \mathcal{Y} &= \mathcal{C}\mathcal{X} + \mathcal{D}\mathcal{U} \end{aligned} \tag{E.9}$$

The updated state vector $\mathcal{X}$ in Eq. (E.9) represents the original ones at various harmonics of the system major frequency as

$$\mathcal{X} = \begin{bmatrix} \vdots \\ x_{-2} \\ x_{-1} \\ x_0 \\ x_1 \\ x_2 \\ \vdots \end{bmatrix} \tag{E.10}$$

The updated system dynamics matrix $\mathcal{A}$ in Eq. (E.9) is a doubly-infinite Toeplitz matrix given by

$$\mathcal{A} = \begin{bmatrix} \ddots & \vdots & \vdots & \vdots & \\ \dots & A_0 & A_{-1} & A_{-2} & \dots \\ \dots & A_1 & A_0 & A_{-1} & \dots \\ \dots & A_2 & A_1 & A_0 & \dots \\ & \vdots & \vdots & \vdots & \ddots \end{bmatrix} \tag{E.11}$$

where the submatrix A_n represents the n-th Fourier coefficient of $A(t)$. $\mathcal{B}$, $\mathcal{C}$, and $\mathcal{D}$ can be defined in the similar manner. The frequency modulation matrix $\mathcal{N}$ is an infinite block diagonal matrix given by

$$\mathcal{N} = \begin{bmatrix} \ddots & & & & & \\ & -2 \cdot j\omega_p I & & & 0 & \\ & & -1 \cdot j\omega_p I & & & \\ & & & 0 \cdot j\omega_p I & & \\ & 0 & & & 1 \cdot j\omega_p I & \\ & & & & & 2 \cdot j\omega_p I \\ & & & & & & \ddots \end{bmatrix} \tag{E.12}$$

where I is the identity matrix of the same dimensions as A_n.

The harmonic transfer function (HTF) is regarded as an operator which relates the harmonics of the input to those of the output for LTP system, and can be derived as follows.

$$\hat{\mathcal{G}}(s) = \mathcal{C}[sI - (\mathcal{A} - \mathcal{N})]^{-1}\mathcal{B} + \mathcal{D} \tag{E.13}$$

Although the matrices in Eq. (E.9) are infinite-dimensional, the number of the terms in the Fourier series is truncated for practical purpose, and the smallest number of them are retained which adequately represents the system dynamics.

E.2 Identification Methodology of the LTP System

As mentioned previously, an input sinusoid at single frequency generates a superposition of sinusoids at several frequencies of various amplitudes and phases in a LTP system. It is exemplified that only three frequencies in the output are to be accounted for in the following derivation. That means, the output Y comprises of the linear combination of the responses due to inputs at frequencies, ω, $\omega + \omega_p$, $\omega - \omega_p$. This is equivalent to regarding the system output as a linear combination of three different transfer functions (each corresponding to one of the three frequencies): G_0,

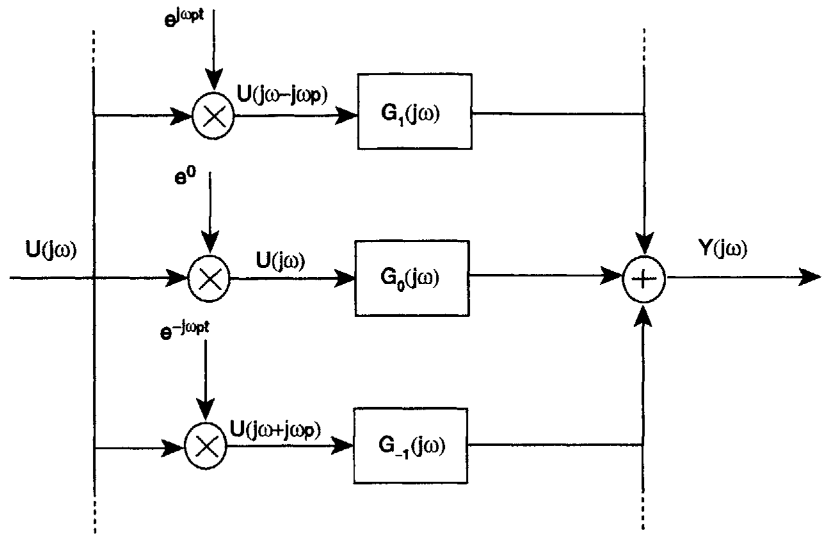

Figure E-1: LTP system block diagram with three transfer functions [62]

G_1, and G_{-1}, respectively. Thus,

$$Y(j\omega) = G_0(j\omega)U(j\omega) + G_1(j\omega)U(j\omega - j\omega_p) + G_{-1}(j\omega)U(j\omega + j\omega_p) \qquad \text{(E.14)}$$

In time domain, Eq. (E.14) can be expressed using the convolution as follows

$$y(t) = g_0(t) * u(t) + g_1(t) * [u(t)e^{j\omega_p t}] + g_{-1}(t) * [u(t)e^{-j\omega_p t}] \qquad \text{(E.15)}$$

A linear system represented by both Eqs. (E.14) and (E.15) is depicted in the block diagram in Fig. E-1.

However, since there is only one equation available in order to estimate three transfer functions G_0, G_1, and G_{-1}, the identification problem becomes underdetermined. This leads to the need of three different input applications for composing three independent equations, each of which is similar to Eq. (E.14). Due to the periodic nature of the system under consideration, it is extremely important to account for the time of application of each input relative to the system period T. In order for the system behavior to be completely analyzed, multiple identical input signals are applied which are evenly located over the system period. In Fig. E-2, an example of the input signals are shown. There, three input signals are created in sine-sweep

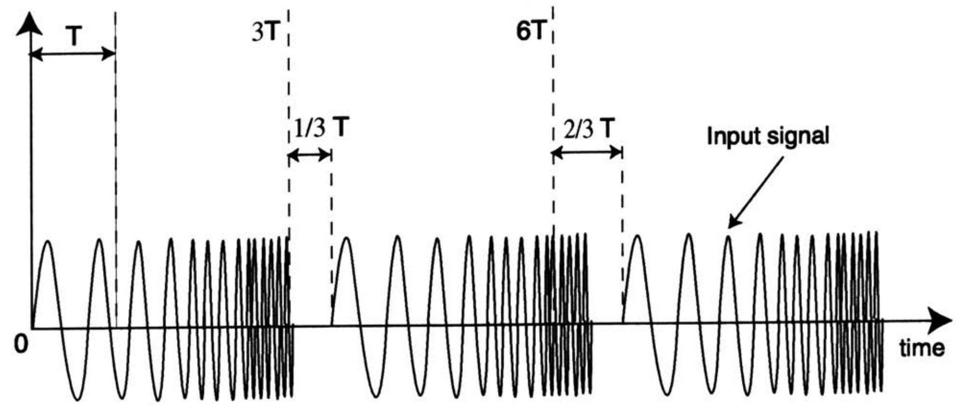

Figure E-2: Input signals generated with appropriate time intervals over the system period [62]

(chirp) form with uniformly separated initiation interval T_d over the system period T, where

$$T_d = T/3 = 2\pi/3\omega_p \tag{E.16}$$

Among the three input signals, the first one should have no delay between the start of the system period and its initiation time. Then, the input U and output Y_0 can be modeled as in Fig. E-1. For the second signal, there should be a delay T_d seconds between them, and the input can be described as $U(j\omega)e^{-j\omega T_d}$, which results in a block diagram shown in Fig. E-3. Similarly, delay for the third signal will be $2T_d$. Then, the output vector Y can be described as follows

$$\begin{Bmatrix} Y_0 \\ Y_{1/3} \\ Y_{2/3} \end{Bmatrix} = \begin{bmatrix} U(j\omega) & U(j\omega - j\omega_p) & U(j\omega + j\omega_p) \\ U(j\omega) & U(j\omega - j\omega_p)e^{j\omega_p T_d} & U(j\omega + j\omega_p)e^{-j\omega_p T_d} \\ U(j\omega) & U(j\omega - j\omega_p)e^{j\omega_p 2T_d} & U(j\omega + j\omega_p)e^{-j\omega_p 2T_d} \end{bmatrix} \begin{Bmatrix} G_0 \\ G_1 \\ G_{-1} \end{Bmatrix} \tag{E.17}$$

where $Y_{1/3}$ and $Y_{2/3}$ are the outputs due to the second and third chirp signals respectively. By using the nomenclature that $W = e^{j\omega_p T_d}$, one obtains from Eq. (E.16)

$$W = e^{j2\pi/3} \tag{E.18}$$

From this definition, it can be derived that $W^{-1} = e^{j2\pi/3}$, $W^2 = e^{j4\pi/3} = W^{-1}$, and $W^4 = W^{-2}$.

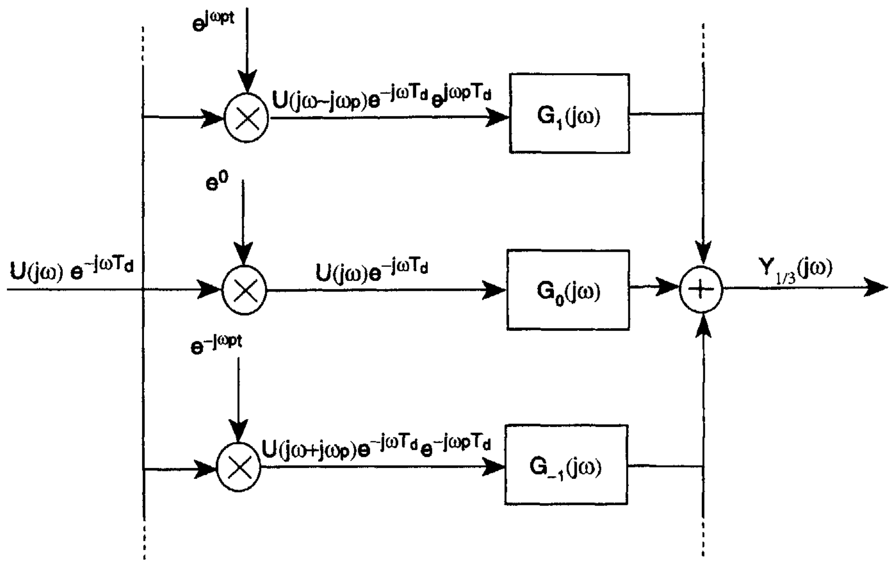

Figure E-3: Delayed input signal and corresponding output of LTP system [62]

Then, Eq. (E.17) becomes

$$\begin{Bmatrix} Y_0 \\ Y_{1/3} \\ Y_{2/3} \end{Bmatrix} = \begin{bmatrix} U(j\omega) & U(j\omega - j\omega_p) & U(j\omega + j\omega_p) \\ U(j\omega) & U(j\omega - j\omega_p)W & U(j\omega + j\omega_p)W^{-1} \\ U(j\omega) & U(j\omega - j\omega_p)W^2 & U(j\omega + j\omega_p)W^{-2} \end{bmatrix} \begin{Bmatrix} G_0 \\ G_1 \\ G_{-1} \end{Bmatrix} \tag{E.19}$$

When the W terms are separated, Eq. (E.19) becomes

$$\underbrace{\begin{Bmatrix} Y_0 \\ Y_{1/3} \\ Y_{2/3} \end{Bmatrix}}_{Y} = \underbrace{\begin{bmatrix} 1 & 1 & 1 \\ 1 & W & W^2 \\ 1 & W^2 & W^4 \end{bmatrix} \begin{bmatrix} U(j\omega) & 0 & 0 \\ 0 & U(j\omega - j\omega_p) & 0 \\ 0 & 0 & U(j\omega + j\omega_p) \end{bmatrix}}_{U} \underbrace{\begin{Bmatrix} G_0 \\ G_1 \\ G_{-1} \end{Bmatrix}}_{G} \tag{E.20}$$

Notice that the first matrix multiplied to give U in Eq. (E.20) is the one that commonly arises in discrete Fourier transform. Eq. (E.20) can be simply written as

$$Y = UG \tag{E.21}$$

or to compute the transfer functions directly

$$G = U^{-1}Y \tag{E.22}$$

The derivation so far is based on the assumption that the output measurements due to each input signal must be conducted by allowing the response to settle down significantly before the next input signal is initiated. Then, it can be reasonably drawn that Y_0 is only due to the fist input, $Y_{1/3}$ due to the second input, and so on. However, to make the identification process faster, input signals with less intervals of no actuation between successive signals is preferred. This leads to the idea of treating the entire input sequence as a single input signal, and similarly the output signal. Then, the problem becomes underdetermined again. In this case, some assumptions on the certain characteristics of G is required to make the problem well defined. In this thesis, a methodology of obtaining transfer functions is adopted which makes the problem constrained with those assumptions.

E.3 Implementation of the Developed Methodology

The identification methodology developed in the previous section requires three sets of data, namely the input u, output y, and time measurements ψ (at which u and y occur). In the case of rotor system identification, the information of ψ can be extracted from the record of the azimuth measurements. These data are recorded in a discrete manner with some fixed sampling frequency (in experiment) or time step size (in analysis), therefore all the data can be assembled in a vector of length n, where n is the total number of the data points. The input data can be expressed as

$$\mathbf{u} = \begin{bmatrix} u_1 & u_2 & u_3 & \dots & u_n \end{bmatrix} \tag{E.23}$$

$\mathbf{y}$ and $\boldsymbol{\psi}$ are similarly defined. If the transfer functions of the system as many as n_h need to be identified, an $n_h \times n$ matrix $\mathbf{U}$ is constructed according to Eq. (E.20) with an appropriately modulated and Fourier transformed vector $\mathbf{u}$ at each row, so that

$$\mathbf{U} = \begin{bmatrix} \mathcal{F}\{[e^{mj\psi_1}u_1 & \dots & \dots & e^{mj\psi_n}u_n]\} \\ \vdots & & \vdots & \vdots \\ \mathcal{F}\{[e^{1j\psi_1}u_1 & \dots & \dots & e^{1j\psi_n}u_n]\} \\ \mathcal{F}\{[e^{0j\psi_1}u_1 & \dots & \dots & e^{0j\psi_n}u_n]\} \\ \mathcal{F}\{[e^{-1j\psi_1}u_1 & \dots & \dots & e^{-1j\psi_n}u_n]\} \\ \vdots & & \vdots & \vdots \\ \mathcal{F}\{[e^{-mj\psi_1}u_1 & \dots & \dots & e^{-mj\psi_n}u_n]\} \end{bmatrix} \tag{E.24}$$

where $m = \frac{n_h-1}{2}$. Eq. (E.24) can be described in a more compact notation as

$$\mathbf{U} = \begin{bmatrix} \mathbf{u}(\omega - m\omega_p) & \dots & \mathbf{u}(\omega - \omega_p) & \mathbf{u}(\omega) & \mathbf{u}(\omega + \omega_p) & \dots & \mathbf{u}(\omega + m\omega_p) \end{bmatrix}^T \tag{E.25}$$

Similarly, $\mathbf{Y}$ can be constructed as the discrete Fourier transform of the vector $\mathbf{y}$ as

$$\mathbf{Y} = \mathcal{F}\left\{\begin{bmatrix} y_1 & y_2 & y_3 & \dots & y_n \end{bmatrix}\right\} \tag{E.26}$$

Recalling that the empirical transfer function estimate (ETFE) of a linear time invariant (LTI) system involves the power and cross spectral densities of input and output, these spectral densities can be defined in a similar manner for the present LTP system as

$$\begin{aligned} \mathbf{\Phi}_{\mathbf{UU}} &= \mathbf{U}^{*T}\mathbf{U} \\ \mathbf{\Phi}_{\mathbf{UY}} &= \mathbf{U}^{*T}\mathbf{Y} \end{aligned} \tag{E.27}$$

where $\mathbf{U}^{*T}$ is complex conjugate transpose of $\mathbf{U}$. Then, the transfer functions can be obtained for LTP system similarly as in LTI system as

$$\widehat{\mathbf{G}}(\omega) = (\mathbf{\Phi_{UU}})^{-1}\mathbf{\Phi_{UY}} \tag{E.28}$$

where $\widehat{\mathbf{G}}(\omega)$ is the harmonic transfer function estimate with each transfer function $\mathbf{g}_i$ at its row as

$$\widehat{\mathbf{G}}(\omega) = \begin{bmatrix} \mathbf{g}_m & \cdots & \mathbf{g}_1 & \mathbf{g}_0 & \mathbf{g}_{-1} & \cdots & \mathbf{g}_{-m} \end{bmatrix}^T \tag{E.29}$$

However, computation of the transfer functions with Eq. (E.28) will not yield an accurate result since only a few harmonics are considered instead of infinite number of them. The cumulative effect of the neglected harmonics is significant so that it can make the transfer functions estimated poorly. Suppose that a given system has inherently N_h transfer functions of significant magnitudes, but only n_h of them are evaluated. Then, its output can be expressed as

$$\mathbf{Y} = \underbrace{\sum_{k=-m}^{m} \mathbf{u}(\omega - k\omega_p)\mathbf{g}_k}_{\text{modeled part}} + \underbrace{\sum_{m<|l|\leq M} \mathbf{u}(\omega - l\omega_p)\mathbf{g}_l}_{\text{unmodeled part}} \tag{E.30}$$

where $m = \frac{n_h-1}{2}$ and $M = \frac{N_h-1}{2}$. The unmodeled part essentially appears as an error $\mathbf{e}$, therefore

$$\begin{aligned} \mathbf{Y} &= \sum_{k=-m}^{m} \mathbf{u}(\omega - k\omega_p)\mathbf{g}_k + \mathbf{e} \\ &= \mathbf{U}^T\widehat{\mathbf{G}} + \mathbf{e} \end{aligned} \tag{E.31}$$

In addition to this modeling insufficiency, the constraints are not applied yet which cures the underdeterminancy of the identification problem mentioned in the previous section. In this regard, an assumption is applied that the transfer functions are smooth enough that there are no rapid variations along with frequency. This generates a minimization problem with a cost function J, which penalizes a quadratic error and curvature of the transfer functions, so that

$$J = \min \left[(\mathbf{Y} - \mathbf{U}^T \widehat{\mathbf{G}})^2 + \alpha (\mathbf{D}^2 \widehat{\mathbf{G}})^2 \right] \tag{E.32}$$

where $\mathbf{D}^2$ is a second-order difference operator, and α is a weighting factor. By taking the derivative of J with respect to $\widehat{\mathbf{G}}$ in Eq. (E.32) and setting it to zero, the minimizing $\widehat{\mathbf{G}}$ can be found as

$$\widehat{\mathbf{G}} = \left[\mathbf{U}^T \mathbf{U} + \alpha \mathbf{D}^4 \right]^{-1} \mathbf{U}^T \mathbf{Y} \tag{E.33}$$

where $\mathbf{D}^4 = \mathbf{D}^2 \cdot \mathbf{D}^2$. Eq. (E.33) is the final form that is utilized in the following system identification, and more issues on the practical implementation of Eq. (E.33) and solutions are provided in [62].

Bibliography

[1] E. M. Laing. Army helicopter and vibration survey mehtods and results. *Journal of the American Helicopter Society*, 19(3):28–38, 1974.

[2] W. E. Hooper. Vibratatory airloading of helicopter rotors. *Vertica*, 8(2):73–92, 1984.

[3] W. K. Wilkie. *Anisotropic Piezoelectric Twist Actuation of Helicopter Rotor Blades: Aeroelastic Analysis and Design Optimization.* PhD dissertation, University of Colorado, Department of Aerospace Engineering Sciences, December 1997.

[4] R. G. Loewy. Helicopter vibrations: A technological perspective. *Journal of the American Helicopter Society*, 29(4):4–30, 1984.

[5] R. Bielawa. *Rotary Wing Structural Dynamics and Aeroelasticity.* American Institute of Aeronautics and Astronautics, 1992.

[6] B. Wang, L. Kitis, W. Pilkey, and A. Palazzolo. Helicopter vibration reduction by local structural modification. *Journal of the American Helicopter Society*, 27(3):43–47, 1982.

[7] M. Hamouda and G. Pierce. Helicopter vibration suppression using simple pendulum absorbers on the rotor blade. *Journal of the American Helicopter Society*, 29(3):19–29, 1984.

[8] J. A. Molusis, Hammond C. E., and Cline J. H. A unified approach to the optimal

design of adaptive and gain scheduled controllers to achieve minimum helicopter rotor vibration. *Journal of the American Helicopter Society*, 28(2):9–18, 1983.

[9] S. R. Hall and Wereley N. M. Linear control issues in the higher harmonic control of helicopter vibrations. In *Proceedings of the American Helicopter Society 45th Annual Forum*, Boston, MA, May 22–24 1989.

[10] S. R. Hall and Wereley N. M. Performance of higher harmonic control algorithms for helicopter vibration reduction. *Journal of Guidance, Control, and Dynamics*, 16(4):793–797, 1993.

[11] F. J. McHugh and J. Shaw. Helicopter vibration reduction with higher harmonic blade pitch. *Journal of the American Helicopter Society*, 23(4):26–35, 1978.

[12] J. Shaw and N. Albion. Active control of the helicopter rotor for vibration reduction. *Journal of the American Helicopter Society*, 26(3):32–39, 1981.

[13] J. A. Molusis, Hammond C. E., and Cline J. H. Wind tunnel results showing rotor vibratory loads reduction using higher harmonic blade pitch. *Journal of the American Helicopter Society*, 28(1):10–15, 1983.

[14] J. Shaw, Albion N., Hanker E. J., and R. S. Teal. Higher harmonic control: Wind tunnel demonstration of fully effective vibratory hub force suppression. *Journal of the American Helicopter Society*, 31(1):14–25, 1989.

[15] K. Nguyen, M. Betzina, and C. Kitaplioglu. Full-scale demonstration of higher harmonic control for noise and vibration reduction on the XV-15 rotor. In *Proceedings of the American Helicopter Society 56th Annual Forum*, Virginia Beach, VA, May 2–4 2000.

[16] E. R. Wood, R. W. Powers, J. H. Cline, and C. E. Hammond. On developing and flight testing a higher harmonic control system. *Journal of the American Helicopter Society*, 30(1):3–20, 1985.

[17] R. G. Loewy. Recent developments in smart structures with aeronautical applications. In *Proceedings of the 37th Israel Annual Conference on Aerospace Sciences*, February 26–27 1997.

[18] P. P. Friedmann. The promise of adaptive materials for alleviating aeroelastic problems and some concerns. In *Proceedings of Innovation in Rotorcraft Technology*, pages 10.1–10.16, London, United Kingdom, June 24–25 1997. Royal Aeronautical Society.

[19] I. Chopra. Status of application of smart structures technology to rotorcraft systems. *Journal of the American Helicopter Society*, 45(4):228–252, 2000.

[20] V. Giurgiutiu. Recent advances in smart-material rotor control actuation. In *Proceedings of the AIAA/ASME/ASCE/AHS/ASC 41st Structures, Structural Dynamics and Materials Conference- Adaptive Structures Forum*, Atlanta, Georgia, April 3–6 2000. AIAA Paper No. 2000–1709.

[21] T. A. Millott and P. P. Friedmann. Vibration reduction in helicopter rotors using an actively controlled partial span trailing edge flap located on the blade. NASA-CR-4611, June 1994.

[22] R. L. Jr. Spangler and S. R. Hall. Piezoelectric actuators for helicopter rotor control. SSL Report 1-89, SERC 14-90, MIT Space Engineering Research Center, Massachusetts Institute of Technology, Cambridge, Massachusetts, January 1989.

[23] C. Walz and I. Chopra. Design, fabrication and testing of a helicopter rotor model with smart trailing edge flaps. In *Proceedings of the AIAA/ASME/ASCE/AHS/ASC 35th Structures, Structural Dynamics and Materials Conference- Adaptive Structures Forum*, Hilton Head, SC, April 21-22 1994. AIAA-94-1767-CP.

[24] M. V. Fulton and R. Ormiston. Hover testing of a small-scale rotor with on-blade elevons. In *Proceedings of the American Helicopter Society 53rd Annual Forum*, Virginia Beach, VA, April 29-May 1 1997.

[25] E. F. Prechtl and S. R. Hall. Design and implementation of a piezoelectric servo-flap actuation system for helicopter rotor individual blade control. AMSL # 00-3, Massachusetts Institute of Technology, January 2000.

[26] A. Hassan, F. K. Straub, and K. W. Noonan. Experimental/numerical evaluation of integral trailing edge/flaps for helicopter rotor applications. In *Proceedings of the American Helicopter Society 56th Annual Forum*, Virginia Beach, VA, May 2–4 2000.

[27] P. Jaenker, V. Kloeppel, F. Hermle, S. Storm, M. Christmann, M. Wettemann, and T. Lorkowski. Development and evaluation of a hybrid piezoelectric actuator for advanced flap control technology. In *Proceedings of the 26th European Rotorcraft Forum*, Rome, Italy, September 14–16 1999.

[28] A. P. F. Bernhard and I. Chopra. Hover testing of active blade-tips using a piezo-induced bending-torsion coupled beam. *Journal of Intelligent Material Systems and Structures*, 9(12):963–974, 1999.

[29] J. H. Milgram and I. Chopra. Rotors with trailing-edge flaps: Analysis and comparison with experimental data. *Journal of the American Helicopter Society*, 43(4):319–331, 1998.

[30] R. Barrett. Intelligent rotor blade structures development using directionally attached piezoelectric crystals. M.S. thesis, University of Maryland, College Park, MD, 1990.

[31] P. C. Chen and I. Chopra. Hover testing of smart rotor with induced-strain actuation of blade twist. *AIAA Journal*, 35(1):6–16, 1997.

[32] J. P. Rodgers and N. W. Hagood. Development of an integral twist-actuated rotor blade for individual blade control. AMSL 98-6, Massachusetts Institute of Technology, October 1998.

[33] C. E. S. Cesnik, S.-J. Shin, W. K. Wilkie, M. L. Wilbur, and P. H. Mirick. Modeling, design, and testing of the NASA/ARMY/MIT active twist rotor prototype

blade. In *Proceedings of the American Helicopter Society 55th Annual Forum*, Montreal, Canada, May 25–27 1999.

[34] A. A. Bent and N. W. Hagood. Piezoelectric fiber composites with interdigitated electrodes. *Journal of Intelligent Material Systems and Structures*, 8:903–919, 1997.

[35] J. P. Rodgers, A. A. Bent, and N. W. Hagood. Characterization of interdigitated electrode piezoelectric fiber composites under high electrical and mechanical loading. In *Proceedings of the Society of Photo-Optical and Instrumentation Engineers*, San Diego, California, 1996.

[36] K. W. Wilkie, R. G. Bryant, J. W. High, R. L. Fox, R. F. Hellbaum, Jr. A. Jalink, B. D. Little, and P. H. Mirick. Low-cost piezocomposite actuator for structural control applications. In *Proceedings of SPIE Smart Structures and Materials Conference*, Newport Beach, CA, March 5–9 2000.

[37] P. C. Chen and I. Chopra. A feasibility study to build a smart rotor: Induced-strain actuation of airfoil twisting using piezoceramic crystals. In *Proceedings of the Society of Photo-Optical and Instrumentation Engineers*, pages 238–254, San Diego, California, Vol. 1917 1993.

[38] R. C. Derham, B. Matthew, and D. B. Weems. An introduction to the aeromechanical design space of "smart" rotors. In *Proceedings of American Helicopter Society Northeast Region National Specialists' Meeting–Improving Rotorcraft Acceptance through Active Controls Technology*, Bridgeport, CT, October 4–5 2000.

[39] A. J. duPlessis and N. W. Hagood. Modeling and experimental testing of twist actuated single cell composite beams for helicopter blade control. AMSL 96-1, Massachusetts Institute of Technology, February 1996.

[40] W. K. Wilkie, M. L. Wilbur, P. H. Mirick, C. E. S. Cesnik, and S.-J. Shin. Aeroelastic analysis of the NASA/ARMY/MIT active twist rotor. In *Proceedings*

of the American Helicopter Society 55th Annual Forum, Montreal, Canada, May 25–27 1999.

[41] C. E. S. Cesnik and S.-J. Shin. On the modeling of integrally actuated helicopter blades. *International Journal of Solids and Structures*, 38(10-13):1765–1789, 2001.

[42] A. M. Badir. Analysis of two-cell composite beams. In *Proceedings of the 36th Structures, Structural Dynamics, and Materials Conferences*, pages 419–424, New Orleans, 1995. AIAA Paper No. 95-1208-CP.

[43] C. E. S. Cesnik and M. Ortega-Morales. Active composite beam cross-sectional modeling - stiffness and active force constants. In *Proceedings of the 40th AIAA Structures, Structural Dynamics, and Materials Conference*, St. Louis, Missouri, April 12–15 1999. AIAA Paper No. 99-1548.

[44] D. H. Hodges. A mixed variational formulation based on exact intrinsic equations for dynamics of moving beams. *International Journal of Solids and Structures*, 26(11):1253 – 1273, 1990.

[45] S.-J. Shin and C. E. S. Cesnik. Design, manufacturing and testing of an active twist rotor. AMSL # 99-3, Massachusetts Institute of Technology, June 1999.

[46] C. E. S. Cesnik and S.-J. Shin. On the twist performance of a multiple-cell active helicopter blade. *Smart Materials and Structures-Special Issue on Rotorcraft Applications*, 10:53–61, 2001.

[47] R. C. Derham and N. W. Hagood. Rotor design using smart materials to actively twist blades. In *Proceedings of the American Helicopter Society 52nd Annual Forum*, Washington, DC, June 4–6 1996.

[48] M. L. Wilbur, Jr. W. T. Yeager, W. K. Wilkie, C. E. S. Cesnik, and S.-J. Shin. Hover testing of the NASA/ARMY/MIT active twist rotor prototype blade. In *Proceedings of the American Helicopter Society 56th Annual Forum*, Virginia Beach, VA, May 2–4 2000.

[49] M. L. Wilbur, P. H. Mirick, Jr. W. T. Yeager, C. W. Langston, C. E. S. Cesnik, and S.-J. Shin. Vibratory loads reduction testing of the NASA/ARMY/MIT active twist rotor. In *Proceedings of the American Helicopter Society 57th Annual Forum*, Washington, DC, May 9–11 2001.

[50] D. A. Peters and C. J. He. A closed form unsteady aerodynamic theory for lifting rotor in hover and forward flight. In *Proceedings of the American Helicopter Society 43rd Annual Forum*, St. Louis, Missouri, May 1987.

[51] O. A. Bauchau. Computational schemes for flexible, nonlinear multi-body systems. *Multibody System Dynamics*, 2:169–225, 1998.

[52] C. E. S. Cesnik and M. Ortega-Morales. Active composite beam cross-sectional modeling-stiffness and active force components. In *Proceedings of the 40th AIAA Structures, Structural Dynamics, and Materials Conference*, St. Louis, Missouri, April 20–23 1999. AIAA Paper No. 99–1548.

[53] V. K. Wickramasinghe and N. W. Hagood. Material characterization of active fiber composite actuators for active twist helicopter rotor blade applications. In *Proceedings of the AIAA/ASME/ASCE/AHS/ASC 41st Structures, Structural Dynamics and Materials Conference- Adaptive Structures Forum*, Atlanta, Georgia, April 3–6 2000. AIAA Paper No. 2000–1499.

[54] X. Shang and D. H. Hodges. Aeroelastic stability of composite rotor blades in hover. In *Proceedings of the 36th Structures, Structural Dynamics and Materials Conference*, New Orleans, Louisiana, April 10 – 12 1995.

[55] D. H. Hodges, A. R. Atilgan, C. E. S. Cesnik, and M. V. Fulton. On a simplified strain energy function for geometrically nonlinear behavior of anisotropic beams. *Composites Engineering*, 2(5 – 7):513 – 526, 1992.

[56] D. A. Peters and C. J. He. Finite state induced flow models part II: Three-dimensional rotor disk. *Journal of Aircraft*, 32(2):323–333, 1995.

[57] D. de Andrade. *Application of Finite-State Inflow to Flap-Lag-Torsion Damping in Hover.* PhD dissertation, Georgia Institute of Technology, 1992.

[58] N. J. Theron. *Multi-Body Dynamic Analysis of Helicopter Rotors.* PhD dissertation, Rensselaer Polytechnic Institute, 1994.

[59] Anonymous. Wind-tunnel model system criteria. LHB 1710.15, NASA Langley Research Center, May 1992.

[60] P. Dixon. Fax correspondence. Technical report, Advanced Technologies Incorporated, Newport News, VA, October 1999.

[61] B. G. van der Wall. Simulation of HHC on helicopter rotor BVI noise emission using a prescribed wake method. In *Proceedings of the 26th European Rotorcraft Forum*, Hague, Netherlands, September 26–29 2000.

[62] A. Siddiqi and S. R. Hall. Identification of the harmonic transfer functions of a helicopter rotor. AMSL 01-1, Massachusetts Institute of Technology, March 2001.

[63] X. Shang. *Aeroelastic Stability of Composite Hingeless Rotors with Finite-State Unsteady Aerodynamics.* PhD dissertation, Georgia Institute of Technology, 1995.

Biographical Note

SangJoon Shin graduated from Seoul National University in Seoul, Korea with a B.S. degree in Aerospace Engineering in February, 1989, with honors. He received a M.S. degree in the same field at Seoul National University in February, 1991. In 1991, he joined the Korean Agency for Defense Development in Taejon, Korea as a research engineer. He had five years' experience at the Helicopter Systems Department and the Turboprop Trainer Systems Group. In August, 1996, he came to the United States and joined the graduate program of the Aeronautics and Astronautics at Massachusetts Institute of Technology. He received the second Science Master degree in Aeronautics and Astronautics in June, 1999. His thesis was entitled: "Design, Manufacturing, and Testing of an Active Twist Rotor." He continued the research of the active helicopter rotor for his doctoral degree.

3231-57